

Dual-Antiphase Patch Antennas for Microwave Imaging and Osteoporosis Screening Results Based on Neural Networks

Theoretical and Experimental Results

by

Johnathan W. Adams

A dissertation submitted to the faculty of

Worcester Polytechnic Institute

in partial fulfillment of the requirements for the

Doctor of Philosophy

in

Electrical and Computer Engineering

December 13th, 2022

APPROVED:

Professor Ara Nazarian (Harvard Med.
School)

Professor Gregory M. Noetscher (WPI)

Professor Kyoko Fujimoto (GE, WPI)

Dr. James Brown (Micro Systems
Engineering, Inc.)

Professor Sergey N. Makaroff (WPI)

To my parents

Abstract

In this thesis, we introduce, construct, and test novel miniaturized antennas for microwave imaging. We also present the corresponding osteoporosis screening and detection results which are based on deep learning.

Microwave Imaging is an emerging medical imaging technology with potential benefits in physical size, complexity, and cost when compared to traditional solutions. There is potential to further optimize the cost of a diagnostic solution by reducing image resolution and relying on signal processing techniques to make up the difference. The required image resolution depends on the application in question. Additionally, for generic imaging, there is potential to increase image resolution using smaller antennas and higher operating frequencies that can be realized using more efficient on-body antennas

A point-to-point transmission setup has been used to measure subjects to determine if they are osteoporotic or healthy. This setup is safe, easy to use, and compact when compared to the standard, x-ray-based imaging modality for osteoporosis. Two dichotomous diagnostic tests were performed using the subset of the study participants who could be conclusively classified as osteoporotic, osteopenic, or healthy. The first test investigated an integral-based classifier that achieved a Youden's J index of 81.5%. The second test investigated the use of a perceptron neural network classifier that produced a Youden's J of approximately 83%. The neural network achieved 94% specificity, making it more suitable for pre-screening potentially osteoporotic patients compared to the less specific integral classifier.

The dual antiphase patch antenna used for osteoporosis detection is inherently more efficient at radiating into the body than contemporary on-body dipole or single-patch antennas. A miniature, 2.4 GHz, version of the dual antiphase patch antenna has been developed using computer simulation, fabricated, and tested for viability in a theoretical high-resolution brain-imaging setup. The balun and matching circuitry have been condensed into the antenna's PCB (Printed Circuit Board). The effect of surface waves was also factored into the design consideration, while maximizing the detected signal's SNR.

Results for Defense

I defend

1. Novel neural network classifier (topology, training, and verification) for microwave imaging of healthy vs osteoporotic bone based on wrist testing results.
2. Design, construction, and testing of a novel miniaturized antenna for microwave imaging: a 2.4 GHz dual antiphase antenna.

Papers

J. W. Adams, Z. Zhang, G. M. Noetscher, A. Nazarian and S. N. Makarov, "Application of a Neural Network Classifier to Radiofrequency-Based Osteopenia/Osteoporosis Screening," *IEEE Journal of Translational Engineering in Health and Medicine*, vol. 9, pp. 1-7, 2021, Art no. 4900907, doi: 10.1109/JTEHM.2021.3108575.

J. Adams, Z. Zhang, G. M. Noetscher, A. Nazarian and S. N. Makarov, "Application of a Neural Network Classifier to Radiofrequency-Based Osteopenia/Osteoporosis Screening," *2021 43rd Annual International Conference of the IEEE Engineering in Medicine & Biology Society (EMBC)*, 2021, pp. 15-18, doi: 10.1109/EMBC46164.2021.9630944.

P. J. Serano, J. W. Adams, and A. Nazarian, "Modeling and Experimental Results for Microwave Imaging of a Hip with Emphasis on the Femoral Neck," in *Brain and Human Body Modelling 2021: Selected Papers Presented at 2021 BHBM Conference*, S. Makarov, G. Noetscher, A. Nummenmaa, Springer Nature, 2022, ch. 10, pp. 125-138. ISBN 978-3-031-15450-8.

J. W. Adams, L. Chen, P. Serano, A. Nazarian, R. Ludwig, S. Makarov, "Miniaturized Dual Antiphase Patch Antenna Radiating into the Human Body at 2.4 GHz," *IEEE J. of EM, RF, and MW in Medicine and Biology*, Under Review.

Presentations

J. Adams, Z. Zhang, G. M. Noetscher, A. Nazarian and S. N. Makarov, "Application of Neural Networks to Radiofrequency Osteoporosis Screening," *2021 43rd Annual International Conference of the IEEE Engineering in Medicine & Biology Society (EMBC)*.

J. Adams, S. N. Makarov, G. M. Noetscher, S. Arum, R. Rabiner, A. Nazarian, and Z. Zhang, "Application of Neural Networks to Radiofrequency Osteoporosis Screening," *Brain and*

Human Body Modelling 2021. Available: <https://education.martinos.org/brain-and-human-body-modeling-conference/>

J. W. Adams, L. Chen, and P. Serano, "Miniaturized Dual Antiphase Antenna at 2.4 GHz for Microwave Imaging" at *Brain and Human Body Modelling Conference 2022*. Available: <https://tmslab.martinos.org/conferences/brain-and-human-body-modeling-conference-2022/>

G. Noetscher, W. Wartman, D. Pham, J. Adams, S. Makarov, "Verification of the VHP-Female V.5.0 Full Body CAD Human Model," *2018 40th Annual International Conference of the IEEE Engineering in Medicine & Biology Society (EMBC)*.

Acknowledgements

Mr. Serano and Mr. Chen for their invaluable assistance and guidance with antenna design and simulation.

Mr. Appleyard for his expertise in design and fabrication of test fixtures. Additionally for his insights and experience with failure analysis and debugging complex physical systems.

Dr. Makaroff for his continued support, advice and guidance throughout this project.

Ms. Ortiz for her assistance with photography of the experimental setups.

Contents

Abstract	3
Results for Defense	4
Papers	4
Presentations	4
Acknowledgements.....	6
Chapter 1. Introduction	11
1.1. Definition of Microwave Imaging.....	11
1.2. Microwave Imaging Application: Stroke.....	12
1.3. Microwave Imaging Application: Osteoporosis	13
1.4. Microwave Imaging Application: Breast Cancer Detection	14
1.5. Advantages of Microwave Imaging.....	15
1.6. Examples of Antennas for Microwave Imaging.....	16
Magneto-Electric Dipole Antennas.....	16
Brick-Shaped Antennas	17
Dual-Antiphase Patch Antennas	17
Chapter 2. Dual Antiphase Patch Antenna Design and Application in the UHF Band [6]	20
2.1. Device Concept.....	20
2.2. On-Body Antenna Design.....	21
2.3. Simulation with Realistic Human Phantom	23
2.4. Device Construction and Measurement Sequence.....	25
2.5. De-embedding Transmission and Reflection Coefficients	27
2.6. Pilot Study	28
2.7. Subject Selection for Dichotomous Diagnostic Test (Osteogenic/Osteoporotic vs Healthy).....	29
2.8. Data Processing for Entire Frequency Band – Transmission through the wrist	30

2.9. Index Functions	32
2.10. Data Processing for a Narrow Frequency Band of 0.1 GHz	33
2.11. Youden's J index for Eq. (3). Finding optimum frequency band.....	33
2.12. Sensitivity and Specificity for the Optimum Frequency Band.....	35
2.13. Improvement of antenna matching	35
2.14. Effect of surrounding tissue	36
2.15. Effect of wave diffraction around the wrist, surface waves	37
2.16. Results for male and female subjects.....	37
2.17. Results for healthy young subjects.....	38
2.18. Radio frequency data adds supplementary information to clinical risk factors	38
2.19. How much supplementary information is contained in “effective” wrist thickness? .	38
2.20. Osteoporosis Detection in Other Body Compartments	40
2.21. Summary.....	41
Chapter 3. Using Neural Networks to Improve Diagnosis from Wrist Tester	43
3.1. Differences Between Breast Cancer and Osteoporosis Application	43
3.2. Radiofrequency Measurement Device	44
3.3. Data Collection.....	45
3.4. The Perceptron	47
3.5. Neural Network Topology.....	48
3.6. Training, Validation, and Classification.....	49
3.7. Results for Non-Normalized Data.....	50
3.8. Results for Normalized Data	50
3.9. Limitations of the Study	52
3.10. Fractures in Group 1	53
3.11. Discussion of Non-Normalized Data.....	53
3.12. Discussion of Normalized Data	54

3.13. Discussion of MLP Network Performance	54
3.14. Number Representations' Effect on Classification Results	55
3.15. Summary.....	55
Chapter 4. Miniaturized Dual Antiphase Patch Antennas for Microwave Imaging of Bone and Other Tissues	57
4.1. Antenna Design and Modelling	58
4.2. Fabrication and Assembly	60
4.3. Phantom Preparation	61
4.4. Efficiency.....	62
4.5. Phantom Measurements vs. In Vivo Human Measurements	62
4.6. Phantom Measurements vs. Simulations	63
4.7. In Vivo Human Head Measurements vs. Simulations.....	64
4.8. Simulated Electric Field Patterns Around Phantom and Human Head	66
4.9. Discussion of Results	66
4.10. Limitations	67
4.11. Summary.....	69
My Publications and Presentations	70
Publications.....	70
Presentations	70
References	72
Appendix A. Prior Art Study Subject Roster.....	86
Appendix B. Modeling and Experimental Results for Microwave Imaging of a Hip with Emphasis on the Femoral Neck.....	88
B.1. Experimental Hardware	88
B.2. Measurement Sites.....	89
B.3. Simulated Antenna Positioning and Human Body Model	90

B.4. Software Modelling of Matched Antennas.....	91
B.5. In Vivo Measurement Results	92
B.6. Simulation Results	94
B.7. Limitations	96
B.8. Validation of Simulation Using In Vivo Measurement Results	97
B.9. Propagation Paths and Antenna Position.....	97
B.10. Frequency Choice and Propagation Through Bone	97
Appendix C. Additional Exploration of Machine Learning Techniques for Osteoporosis Detection	99
C.1. Base Data.....	99
C.2. Data Augmentation	100
C.3. Principal Component Analysis	101
C.4. Feature Selection	102
C.5. Training and Validation	103
C.6. PCA Results	104
C.7. Feature Selection Results.....	105
C.8. MLP Classifier Results.....	106
C.9. Limitations	107
C.10. Dimension Reduction.....	107
C.11. MLP Classifier	107
Appendix D. Design of Antenna Array Switchboard for Microwave Imaging	108
D.1. Constraints	108
D.2. System Design	109
D.3. Board Design.....	110

Chapter 1. Introduction

Microwave imaging is a set of emerging and affordable medical imaging techniques that use electromagnetic waves in a variety of configurations to determine information pertaining to the interior of an object. For the purposes of this document, the object in question is the human body. This thesis will investigate the properties of dual-antiphase antennas and how their properties address some of the challenges associated with performing microwave imaging on the human body.

One advantage of microwave imaging is its low cost and affordability as compared to CT (computer tomography), MRI (magnetic resonance imaging), and other human body imaging modalities such as positron emission tomography (PET), etc. The notable exception is ultrasonic imaging, which is also inexpensive when compared to traditional imaging modalities. The major disadvantage is its low resolution and inability of deeper penetration at higher frequencies, which are also disadvantages shared by microwave imagers. Unlike ultrasonic imagers, microwave imagers can measure dielectric properties of tissues (dielectric constant and conductivity), which is impossible with any other method.

1.1. Definition of Microwave Imaging

Microwave imaging is the practice of transmitting microwave-length radio waves into an object and using the reflected and/or transmitted signals to determine properties of the interior of the object. Typically, microwave imaging refers to microwave tomography: the practice of creating a map of material layers differentiated by their dielectric properties. However, microwave imaging also includes less sophisticated techniques.

Initial inquiries into what is now known as microwave imaging began in the late 1970s when Jacobi, Larsen, et al. immersed two antennas in water with various tissue samples between them [1], [2]. This was the first published experiment in which active electromagnetic stimulus was applied to a sample to measure scattering [2], though prior to this some passive measurement of various samples had been performed [3]. This experiment forms the basis of current microwave imaging: sending electromagnetic waves into a sample and observing the scattering of the wave to determine properties of the sample.

Practical microwave imaging of biological samples has been challenged by the high attenuation of electromagnetic waves in biological tissue and the dielectric mismatch between

the media surrounding the antenna and the sample itself. To address this, recent studies have placed different media between the microwave antennas and the biological sample, including but not limited to air [4], tuned-dielectric rubber [5], and the biological sample itself [6]. Additionally, antennas have been designed specifically for direct contact with and transmission through biological samples. The dual-antiphase patch antenna is one of these designs [7], [8].

Additionally, microwave imaging suffers from a penetration versus precision trade-off. Wavelength is inversely proportional to frequency and directly proportional to the size of physical features the imager can detect. Conversely, attenuation of the electromagnetic wave over distance inside the body is inversely proportional to frequency and, therefore, directly proportional to wavelength.

1.2. Microwave Imaging Application: Stroke

A stroke occurs when the blood supply to some or all regions of the brain is interrupted. This can be due to a clogged artery, known as an ischemic stroke, or due to a ruptured artery, which causes a hemorrhagic stroke [9]. Diagnosis of strokes through accurate imaging technologies is common practice and is generally accomplished by MRI (magnetic resonance imaging) or CT (computerized X-ray tomography) [10]. Further, post-operative monitoring has been strongly correlated with reduced short-term “death or disability,” among said stroke patients [11] because some treatments are effective against one type of stroke, yet they make the other type worse. These conventional imaging technologies, however, have some drawbacks for post-operative monitoring of stroke patients. Chiefly among these drawbacks are the “portability, cost and harmful effects,” [10] associated with these systems. CT and MRI machines are expensive enough that most locations do not have enough machines to provide continuous monitoring to more than a couple of patients. Both are room-scale machines that require the patient to lie down on a moving platform positioned by the operator. Finally, CT is X-ray based and therefore not suitable for long-term use due to the accumulation of ionizing radiation. For contrast, ultrasonic monitoring can speed up thrombolysis of ischemic strokes but can sometimes exacerbate hemorrhagic strokes or cause bleeding elsewhere in the brain, depending on its frequency [12].

Microwave imaging, by comparison, does not have these drawbacks. It lacks the large power requirements and room-scale electromagnet that MRI relies upon, and microwaves are non-

ionizing, as they are below visible frequencies. Lower power requirements and fewer large, expensive, or specialty parts offer a potential cost savings as well. It is equally suitable to ischemic and hemorrhagic strokes and does not risk further damage to the body.

Microwave stroke detection relies on the difference in dielectric properties between the pooled or clotted blood and the surrounding brain tissue. When the transmitted electromagnetic wave encounters this boundary, it scatters. By monitoring different locations on the outside of the head and using knowledge of the dielectric properties of the tissues, the location the scattering occurred can be reconstructed [2], [4], [10]. Performing this process repeatedly with different directions for the incident wave produces a boundary of the built-up blood, whether the stroke is ischemic or hemorrhagic [10].

Some developmental products for microwave imaging based stroke detection include the MedField MD-100 Strokefinder [13], the EMTensor BrainScanner [14], and the EMVision [15]. Notable recent academic work includes a fixed 3-D array [10] using antennas with a specialized graphite-rubber matching medium [5] to improve performance made by Dr. Vipiana and her group from Politecnico di Torino. Additionally, a group at the University of Queensland built a 2-D array and used it to demonstrate their polar sensitivity encoding for faster processing of tomography data [16], as well as a flexible 3-D array [17]. Finally, a group at the City University of Hong Kong built a differentially fed magneto-electric dipole antenna that utilizes a liquid matching solution to achieve coupling to the body [18].

1.3. Microwave Imaging Application: Osteoporosis

Osteoporosis is a degradation of trabecular bone, which makes up the inner core of human bones [19]. This degradation can subsequently lead to bone fractures, particularly at the hip and spine. The World Health Organization (WHO) has defined individuals at risk for these fractures based on their areal Bone Mineral Density (aBMD, g/cm²) relative to that of a normal young adult, as measured by Dual-energy X-ray Absorptiometry (DXA). Some shortcomings of DXA include exposing patients to small ionizing radiation doses of up to 0.86 mrem [20]; the surrounding soft tissues can introduce relevant measurement errors [21], [22]; bone mineral density (BMD) measurements are affected by variations in bone size [23], [24]; and measurements of cortical and trabecular bone cannot be separated [25]. Additionally, fracture predictions based on aBMD are neither sensitive nor specific [26], [27], [28], [29], [30].

Therefore, quantitative ultrasound measurement techniques, which correlate well with DXA [31], can be improved upon.

Microwave or radiofrequency imaging of (heel) bone was first introduced by Dr. Keith Paulsen and his research group at Dartmouth College in the early 2010s as an alternative non-ionizing diagnostic method to assess bone health [4], [32], [33], [34], [35]. Due to the well-known complexity and poor spatial resolution of the standard microwave imaging setup [36], [37] used in these studies, no clinically applicable results have been generated to date. However, the underlying physical idea of this method is simple and powerful. In osteoporosis, bone mass decreases and pore size increases. The lost bone mass is replaced by a mixture of yellow bone marrow. Such substantial changes in physical properties must alter electromagnetic tissue properties [38], [39] and must generate a significantly different radiofrequency (RF) channel through the bone. It may therefore be sufficient to track an integral measure of radio wave propagation along the path through the bone [6] instead of restoring the complete permittivity map, as attempted previously [4], [32] [33] [34] [35]. A comparison of the setups for these two methods is shown in Fig. 1.

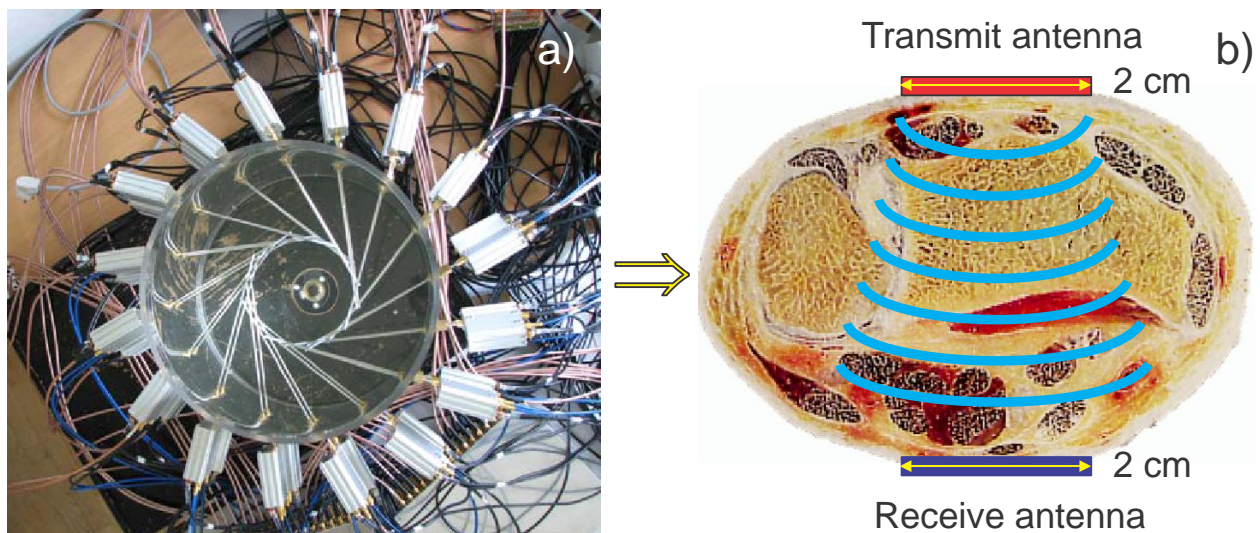


Fig. 1. (a) typical microwave imaging setup [37], (b) author's point-to-point transmission setup for measuring bone density at the wrist [6].

1.4. Microwave Imaging Application: Breast Cancer Detection

Breast cancer is a general term for any cancerous growth that occurs in the breasts [40]. Recently, it has been established that these cancerous growths have different dielectric properties from the surrounding tissue [41], [42], [43], [44], [45], [46], [47], [48], [49], [50],

though the magnitude of the differences is strongly dependent on the type of tissue surrounding the tumor [51], [46], [47]. X-ray mammography is the standard technology for breast cancer detection, though ultrasound, MRI, and PET (Positron Emission Tomography) solutions also have been investigated [51]. Mammograms expose patients to regular doses of x-rays, which are a form of ionizing radiation. Additionally, they typically take a two-dimensional scan and therefore require some positioning of the subject which can be difficult or unpleasant. Finally, there are scenarios, chiefly in non-fatty tissue, in which the mammogram does not always provide meaningful distinction between the malignant tissue and the surrounding tissue [51], [52]. Ultrasound is safe but suffers from low resolution. In general, it has trouble differentiating between malignant and benign tumors [51], [53]. MRI is known to have high sensitivity but varying specificity in this application [53]. Its cost serves to keep it away from screening work. PET detects positrons emitted when a radioactive mixture is processed by the breast cells. This allows early detection at the expense of radiation exposure and low resolution [51].

Dr. Hagness and her group at the University of Wisconsin have explored multiple setups for both passive and active microwave imaging to detect breast cancer [46], [47], [54], [55], [56]. Dr. Paulsen, Dr. Meaney and their associates at Dartmouth College have performed multiple experiments on microwave tomography of the breasts [57], [58], [59], [60]. Dr. Zhurbenko, Dr. Krozer and their collaborators investigated a three-dimensional microwave imaging system [37], which is shown in Fig. 1a.

1.5. Advantages of Microwave Imaging

Compared to traditional imaging techniques, microwave imaging requires less sensor hardware and comparatively few moving parts. Moreover, despite their design complexity, antennas are simple to fabricate when compared to magnetic excitors or X-ray sensors. All of these factors contribute to a much lower cost of production for microwave imaging equipment when compared to MRI, CT, or PET. Microwave antenna coupling is less volatile and is relatively simple to do. Additionally, the ultrasound imaging methods cannot resolve electric properties of the human tissues, which allows microwave imagers higher possible accuracy of diagnosis for a comparable image resolution.

The measurement hardware and stimulus generators used by microwave sensors remain complex but are comparable in size to control packages for other sensing technologies. Due

to the small size of the antennas, this control hardware often constitutes the bulk of a given microwave imaging system's physical size. Such setups [6] are small and portable compared to traditional imaging machines for the same task. Additionally, thanks to the popularity of radio communications, parts for microwave imaging systems are readily available off-the-shelf. This further improves the cost-to-performance for commercial microwave imaging devices when compared to other sensing modalities. Further, microwave imaging does not expose patients to ionizing radiation or strong magnetic fields. It can be used more frequently and with less preparation and caution than MRI or CT. As far as absorbed power goes, the device described in [6] transmits with less power than a typical cell phone.

1.6. Examples of Antennas for Microwave Imaging

The following three antenna types described below are examples of different approaches to solving or circumventing the problems inherent to microwave imaging. First, the magneto-electric dipole antenna separates the axes of the magnetic and electric resonators to limit the strength of skin-surface-propagating electromagnetic waves (surface waves) and uses a liquid intermediary solution to match the antenna to the body. Second, the brick-shaped antenna seeks to solve the problem of mismatch and conformality using a flexible solid medium. Third, the dual-antiphase patch antenna eschews an intermediary matching medium and instead seeks to achieve a superior direct-coupled transmission through the body using antiphase resonators with an unconventional feed structure.

Magneto-Electric Dipole Antennas

The magneto-electric dipole antenna discussed here is a permutation of the standard magneto-electric dipole antenna [61]. It is a dielectric-matched antenna with a focus on directing all transmitted power into the body. The name of the antenna is derived from the separation of the magnetic and electric dipoles due to the three-dimensional L-shape of each radiator. The antenna has, "two horizontal patches performing as a half-wavelength electric dipole and two vertically oriented quarter-wavelength shorted patches together with a portion of the ground plane between them performing as a magnetic dipole," [18]. These elements are immersed in a commercial matching liquid and backed by a cavity reflector that serves a dual role to contain the matching liquid. The antenna is also packaged with an impedance transformer, implemented using the interior layers of the mounting PCB to produce a coaxial arrangement, known as a substrate-integrated coaxial line (SICL) [18].

Compared to other contemporary antennas, the magneto-electric dipole antenna is not susceptible to surface-waves. Almost all of the radiated power is directed into the body, and any surface-waves travel in the subsurface skin layers instead of the outside surface of the skin. Additionally, it demonstrates wide-band performance between 0.4 and 2.3 GHz [18].

Brick-Shaped Antennas

The brick-shaped antenna is an evolution of the dielectric-matched antenna concept with a focus on real-world usability. Instead of using a liquid dielectric, the brick-shaped antenna employs a block of graphite-saturated rubber to match the radiator to the body [5]. The authors note that while the graphite powder does provide the required permittivity, it also increases conductivity, though the authors observe that the new conductivity is similar to conductivities of contemporary liquid matching solutions [5], [62].

Compared to liquid-matched antennas the brick-shaped antenna is minimal maintenance and easily repositionable while maintaining a good match between the antenna and the body. It can be placed in orientations that are difficult for liquid antennas, and the flexible rubber deforms to provide full contact between the brick and the body's contours [63], [64].

The underlying antenna element is a triangular planar monopole with a "trimmed back-placed ground plane," [5]. It is strip-line-fed and matched on the feed side by a distributed matching network [5].

Dual-Antiphase Patch Antennas

Dual-antiphase patch antennas are an evolution of antennas designed for direct contact with the human body, with the goal of penetrating the signal into the body. Other antennas built for this purpose include broadband monopole and dipole antennas [54], [65], [37], [66], [67], [55], [68], [69], small arrays [54], [65], [37], [66], [67], [55], and multi-band single-patch antennas [56], [70]. These antennas typically suffer, "from a lower transmission coefficient" [6] through any significant quantity of living tissue.

The dual-antiphase patch antenna addresses this shortcoming by changing the interactions between the waves in the antenna and in the skin. This change is achieved due to the construction of the dual antiphase patch antenna: instead of two dipole wings, the dual antiphase patch antenna consists of two entirely separate antennas, in close proximity to each other and fed in antiphase as shown in Fig. 2, via a 180° power splitter. A similar

antiphase feeding mechanism for two dipole wings is known as the Dyson balun [71], [72], [73].

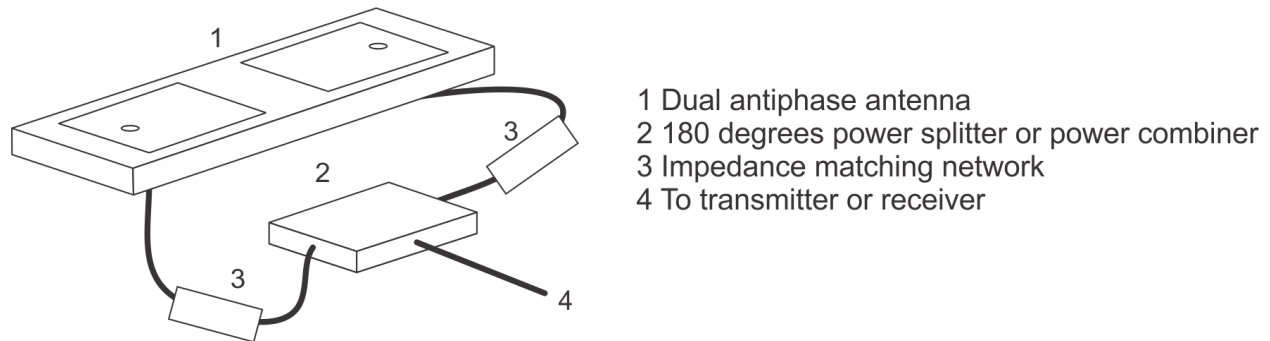


Fig. 2. Dual-antiphase patch antenna [7].

Utilizing two separate antennas driven in antiphase increases the distance current must travel through the body to short between the two radiators, therefore increasing the penetration of the incident wave into the body.

Given a distributed resistance/capacitance approximation of body tissue, Fig. 3 illustrates the dual antiphase antenna concept. Fig. 3a illustrates the path between two wings of a single on-body dipole with the feed in the middle. On the other hand, Fig. 3b shows the approximate path of the subsurface currents when the two *independent* patch antennas are fed in antiphase. Despite their relative proximity, these two antennas are necessarily spaced farther apart than the wings of the dipole antenna (from Fig. 3a). In the dual-antiphase configuration, the antenna electric current has its maximum at the centerline of every patch, far away from the feed. When fed in antiphase, the electric field penetrates the body well due to the longer current shorting path in the body. This improves the coupling of the near surface of the body to the antenna, thereby allowing current to radiate into the body with similar efficiency to the current on the metal parts of both patch antennas.

Typical singular on-body loop or dipole antennas, by contrast, are less efficient when in contact with the relatively conductive body, due to the small physical length of the shorting path between the feeds. In the worst case, this short can prevent the majority of the antenna body from such an antenna from being excited.

Numerical simulations and empirical measurements confirm that dual-antiphase antennas that work well on living tissue do not, in general, work well in air even near said tissue. Gaps

less than 1 mm have proven serviceable in practice [6] especially when populated by a thin insulator instead of air, though best performance is achieved by direct coupling to the skin.

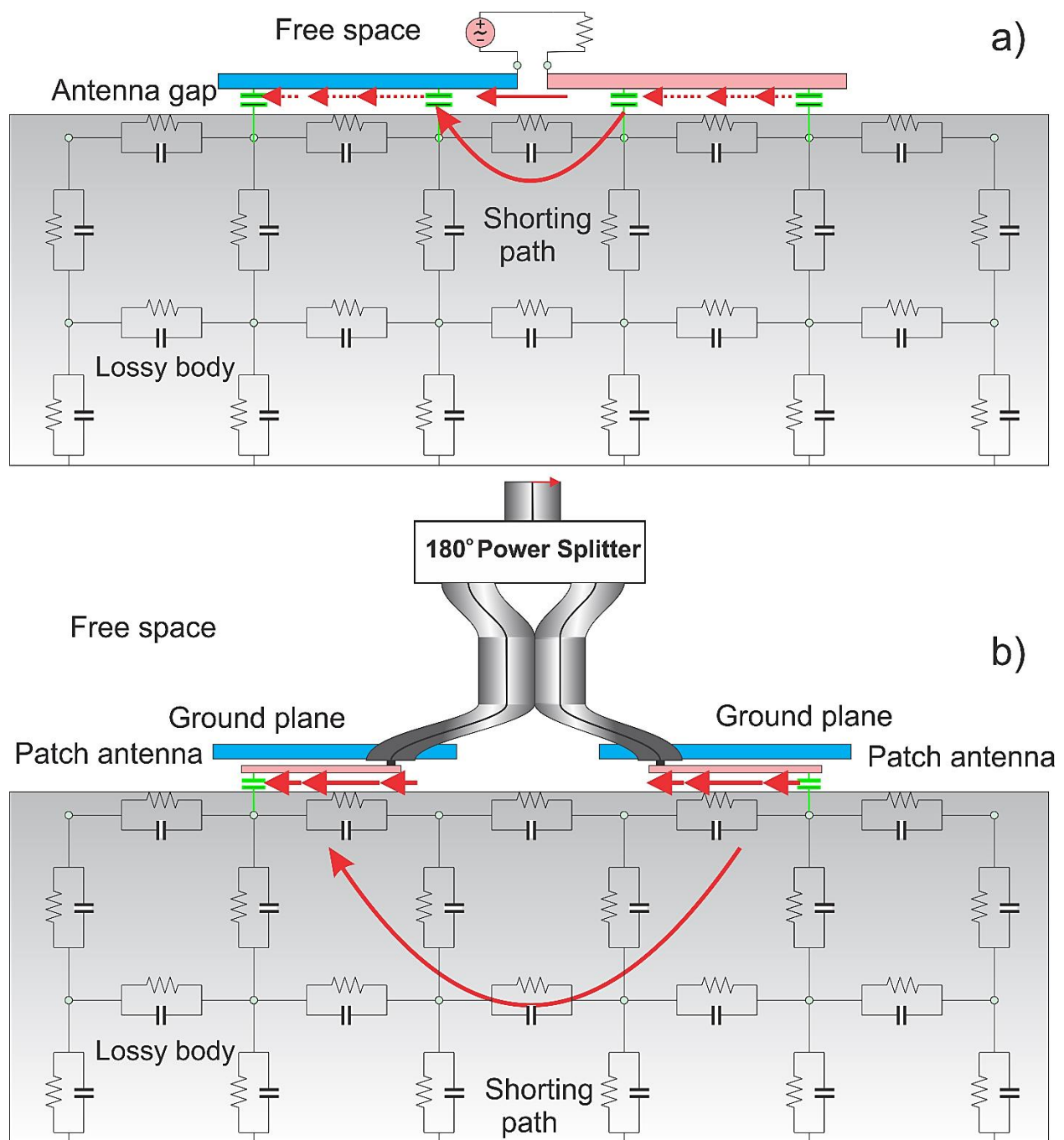


Fig. 3. Dual-antiphase patch antenna theory of operation and comparison of subsurface current paths [7]. (a) Conventional center-fed on-body dipole antenna arrangement: high currents near the feed can be shorted by the body in the immediate feed vicinity, (b) Dual-antiphase patch antenna: currents attempting to travel through the body subsurface from one feed to another take a longer path through the body due to spacing of two antennas. Those oscillating currents simultaneously radiate into the body.

Chapter 2. Dual Antiphase Patch Antenna Design and Application in the UHF Band [6]

This chapter discusses the wrist tester device, its data, and the initial inquiries into classification of the results as background for the use of machine learning for the same task, presented in the next chapter. The osteoporosis screening device is based on the hypothesis that it may be sufficient to track an integral measure of radio wave propagation along the path through the bone instead of restoring the complete permittivity map of the bone and the surrounding tissues, as attempted previously [4], [32], [33], [34], [35].

To do so, the device operate on a transmission path through the body that is mostly composed of bone. The wrist was the readily accessible point at that satisfied this requirement. The authors used their proposed dual-antiphase patch antenna [8]. They measured radio wave propagation through the wrist and compared their results with osteoporotic and osteopenic (low bone density) conditions established via DXA and through a history of bone fracture.

Essentially, the device is equivalent to two low-power cellphones placed on both sides of the wrist with one transmitting and the other receiving. The radiofrequency (RF) signal goes through the bone and mimics its properties. The RF setup radiates into the wrist 0.1 W of RF power in the 0-2 GHz band, which is significantly less than the radiated power of a typical cellphone (between 0.6 W and 3 W) operating in the same frequency band.

2.1. Device Concept

The device concept is illustrated in Fig. 4a. Two dual antiphase patch antennas (Fig. 4b), described in the text below, are placed on both flat sides of the wrist close to the position of the ulnar head under an applied controlled pressure of 1 kg force. The radiofrequency signal in the 0 – 2GHz band travels from the transmit antenna through bone, cartilage, and soft tissue to the received antenna while being attenuated and scattered. The total amount of attenuation and scattering is measured via the microwave transmission coefficient $S_{21}(f)$ and is correlated to osteopenic and osteoporotic conditions. The antenna width across the wrist is 2 cm; the antenna length along the wrist is 5 cm; facilitating continuous contact between the two surfaces.

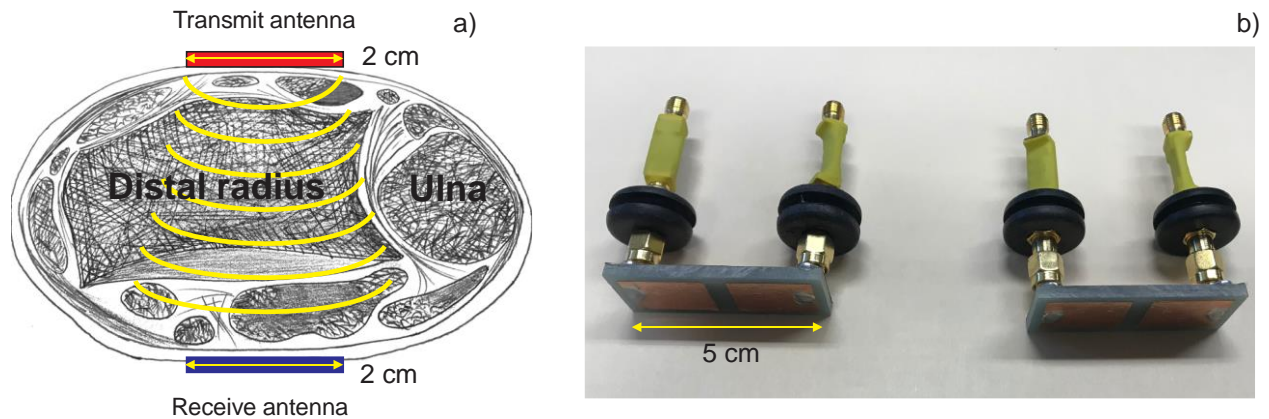


Fig. 4. (a) – Idealized diagram illustrating antenna placement on both sides of a human wrist. (b) – Transmit and receive dual antiphase patch antennas with individual lumped-component matching networks (green isolation) designed for the present chapter. Antenna length (along the wrist) is 5 cm; antenna width (across the wrist) is 1.8 cm. [6]

2.2. On-Body Antenna Design

Dedicated antennas for radiating into the body or receiving from the body are located on the skin surface. In the initial device prototypes, single slotted patch antennas [74], [75] or printed dipoles attached to the wrist were employed. Both antenna types suffered from a lower transmission coefficient through the wrist. To overcome this, a new antenna configuration known as the dual antiphase patch antenna (shown in Fig. 5a as Configuration A) was designed and optimized [8]. This new configuration resembles an array of two patch antenna radiators in echelon, with the patches facing toward the body. However, the probe (or microstrip) feeds are located on the opposite sides of the patches. Most importantly, the individual antennas are fed in antiphase using a 180° power splitter.

The two antiphase patch radiators provide a greater penetration depth and transmitted signal into the body than a single antenna or two adjacent patch antennas in phase. To demonstrate this, Fig. 5 presents simulation results for the radiated electric field of four representative antenna configurations. These results are obtained at 915 MHz simulation frequency with the commercial FEM software ANSYS HFSS Electronics Desktop 2019R1. The wrist is modeled as a brick with a height of 6 cm, an average relative dielectric constant $\epsilon_r = 30$, and an average conductivity $\sigma = 0.1$ S/m. The 3.25 mm thick substrate (FR4 or a low-loss Rogers laminate) has the size of 50×20 mm. The two radiators are fed in antiphase, with a port power of 0.05 W each. Both ports are matched to $10 - j5$ ohm. The antenna indicates both parallel and series resonances, which are closely spaced.

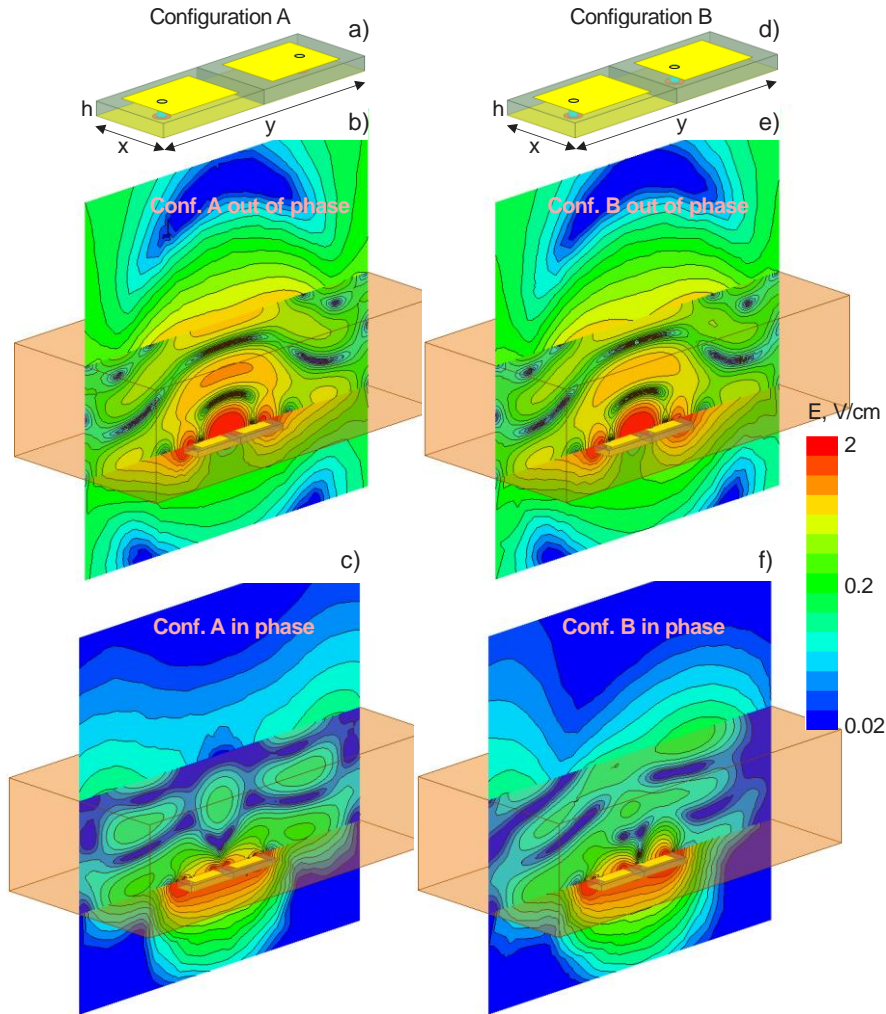


Fig. 5. Four representative antenna configurations (configuration A fed in antiphase or phase and configuration B fed in antiphase or phase, respectively). Out-of-phase antenna array concept (b, e) is compared to the standard in-phase directional antenna array concept (c, f). Electric field magnitude is shown given 0.05 W of power per individual antenna radiator port at 915 MHz. The dual antiphase patch antenna in (a) has been selected. [6]

While Fig. 5b shows the magnitude of the electric field for antiphase feeding, Fig. 5c is the same result but for the in-phase feed. In the former case, the signal propagates into the body and is strong. In the latter case, the signal is significantly absorbed in the vicinity of the antenna and is mostly directed outwards, i.e. into air. For comparison purposes, Fig. 5e and Fig. 5f show the same results but when the two individual patch antennas are in echelon as in Fig. 5d (Configuration B). The antiphase feeding again causes strong transmission, but it is weaker than that of Configuration A (Fig. 5b). Furthermore, the beam is not entirely symmetric.

When matched to $10 - j5$ ohm prior to the power splitter, the dual antiphase patch antenna in configuration A from Fig. 5a indicates a sufficiently large impedance bandwidth shown in Fig. 6. The band is centered approximately around 800-900 MHz and holds for different values of both the dielectric constant and the conductivity of the tissue. Therefore, Configuration A from Fig. 5a was selected as the on-body dual antiphase patch antenna prototype.

Numerical simulations indicate that the antenna performance quickly deteriorates when a gap between the antenna and the body reaches or exceeds 1 mm. Therefore, in the ideal setting, this gap should be either minimized or a direct ohmic contact with body surface should be maintained with the assistance of a gel. The authors suggest minimizing the gap by applying a controlled pressure to the antenna attached to the body, negating the need for a gel.

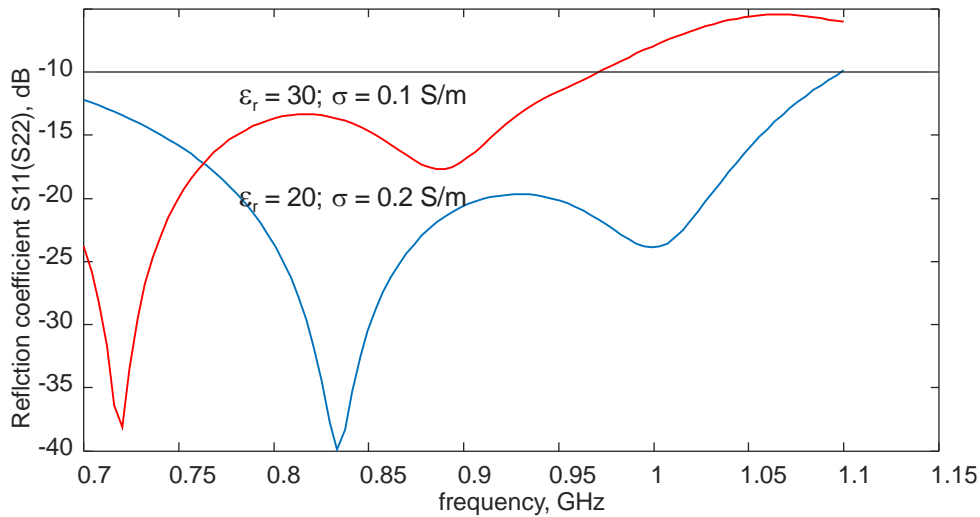


Fig. 6. Simulated reflection coefficient magnitude in dB, $|S_{11}(f)|_{dB}$, of the dual antiphase patch antenna from Fig. 5a as a function of frequency loaded with different values of average tissue permittivity/conductivity. Matching to characteristic impedance of $10 - j5 \Omega$ is assumed. [6]

2.3. Simulation with Realistic Human Phantom

The anatomically accurate computational human model VHP-Female [76], derived from the Visible Human Project (VHP) of the U.S. National Library of Medicine, has been used for the simulations of a realistic, inhomogeneous wrist model described below. The VHP-Female model characterizes a 60-year-old Caucasian female subject with a height of 162 cm as measured from top of the scalp to the average center of both heels. The body mass of the model is 88 kg, resulted in a computed Body Mass Index of 33.5 (moderately obese). The model has separate anatomical skin and fat layers of variable thicknesses and has been

augmented with electromagnetic tissue properties from the IT'IS Database [39] in the frequency range from 10 MHz to 100 GHz.

A wrist model from the VHP-Female with 10 individual tissue sub-compartments has been isolated, augmented with the antenna models from Fig. 5a, and simulated at 915 MHz using the FEM based software ANSYS HFSS Electronics Desktop 2019R1 with seven adaptive mesh refinement passes, and a given input power of 1 W into each radiator of the dual antiphase patch antenna on bottom of the wrist, mimicking the transmitter (TX) setup. The receiver (RX) arrangement includes an identical dual antiphase patch antenna on top of the wrist. The model configuration is shown in Fig. 7a.

Simulation results are shown in Fig. 7b and Fig. 7c, respectively. Fig. 7b demonstrates distribution of the Poynting vector across the wrist cross-section with the lower threshold of 0.1 W/m^2 . Simulation results reveal that the majority of the radiated power propagates through the center of the wrist and through the bone marrow toward the receiver antenna. A vanishingly small power flow is observed close to the perimeter of the wrist. This is a consequence of the dual antiphase patch antenna design described in the previous section. The effects of both wave diffraction and of the associated surface waves around the wrist thus appear to be negligibly small, as seen in Fig. 7b. Additionally, Fig. 7c shows the distribution of the complex magnitude of the total electric field through the wrist cross-section with the most significant transmitted field observed for cortical and trabecular bone. Similar results have been obtained at 600 MHz and 1200 MHz, respectively.

This simulation model does not account for anisotropy of trabecular bone since the authors were unable to find the anisotropic dielectric material properties for the given frequency bands. The authors also mention the lack of data on dielectric radiofrequency properties of the osteoporotic bone in the literature. Trabecular or cancellous bone forms the inner part of the medullary cavity in short and flat bones. In trabecular bone, the anisotropic calcified tissue is arranged in the form of plates or struts called trabeculae, approximately $200 \mu\text{m}$ thick, creating numerous interconnected cavities [77]. These cavities are filled with bone marrow. In osteopenic/osteoporotic bone, the trabecular bone matrix is partially replaced by a soft fatty tissue. Correlation of mechanical anisotropy with dielectric bone properties has been discussed in [78]. Also note that the isotropic dielectric data given in [39] were obtained with animals *in vivo* and *in vitro*, and therefore cannot be considered as perfectly accurate for the

human wrist. For instance, [78] reports rather different values of the dielectric constant for human trabecular bone. Additional relevant research on bone dielectric properties was performed in [35], [78], [79], [80].

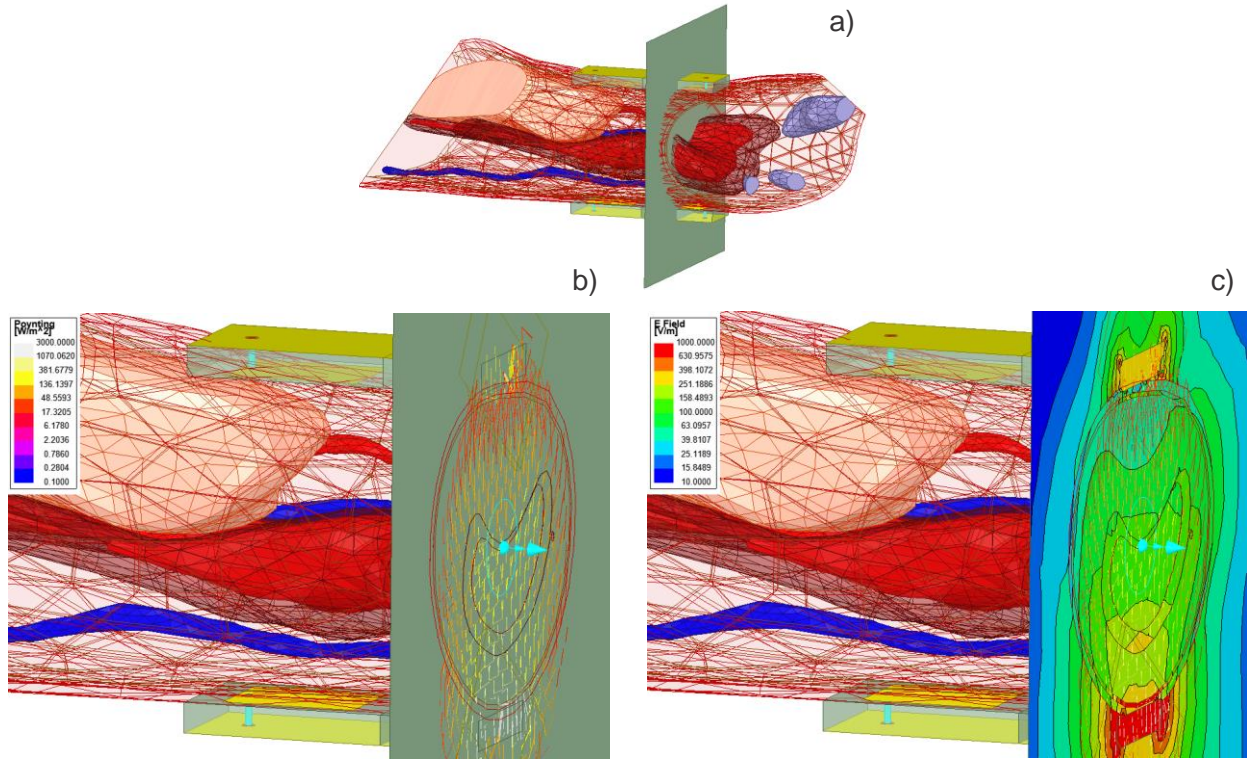


Fig. 7. (a) – Computational model configuration. The RX dual patch antenna is on top of the wrist; the TX antenna is on its bottom. (b) – Distribution of the Poynting vector through the wrist cross-section with the lower threshold of 0.1 W/m^2 and the upper threshold of 3000 W/m^2 or 0.3 W/cm^2 . The majority of the radiated power propagates through the center of the wrist and through the bone marrow toward the receiver antenna while a vanishingly small power flow is observed close to the perimeter of the wrist. (c) – Distribution of the complex magnitude of the total electric field through the wrist cross-section. [6]

2.4. Device Construction and Measurement Sequence

The prototype for the radiofrequency wrist tester device is shown in Fig. 8. It includes a transparent plastic enclosure, a movable top frame (using two stepper motors with a microcontroller connected to the pressure sensors), two 2×1 antenna arrays described previously, and four pressure sensors. Wrist measurements are performed when a controlled pressure of 1 kg of force is applied. The authors increase the measurement repeatability and accuracy of the device by incorporating a pressure-controlled, solid, and precisely adjustable wrist support. This allows the authors to precisely control pressure during antenna attachment to the wrist. The testbed in Fig. 8 includes the following major components:

- Movable top with four pressure sensors (FlexiForce® ESS301) connected to a microcontroller and a 2x1 receiver antenna array with a 180° power splitter (ZFSCJ-2-4-S, Mini-Circuits). The pressure sensors and the array use a flexible support to enable better adjustment to various wrist sizes.
- Fixed bottom with the identical embedded (and replaceable) 2x1 transmit antenna array printed on 128 mil FR4 and another 180° power splitter; two cables from the splitter are wired together.
- Supporting frame, which could potentially measure wrist thickness after applying pressure from top.

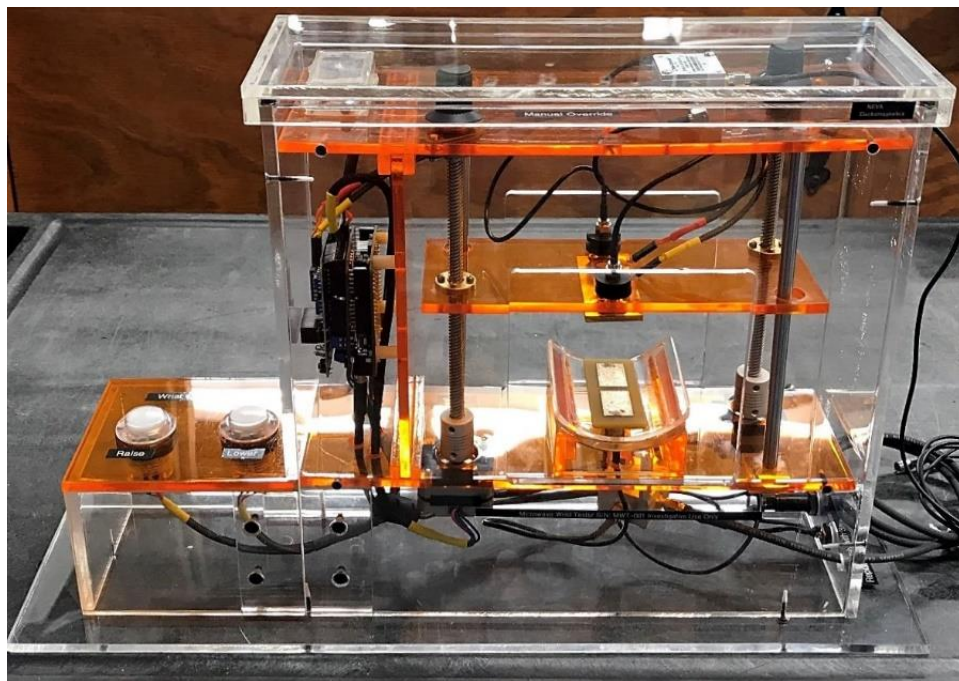


Fig. 8. Microwave setup with transmitting/receiving dual antiphase patch antennas (each comprising of two closely spaced patch antennas fed in antiphase), gear motors, pressure sensors, and a microcontroller. [6]

Measurements are performed by putting the wrist inside the device holder horizontally at a prescribed position of the ulnar head. The device top moves down and stops automatically when the applied pressure reaches 1 kg of force (3-7 sec), irrespective of wrist diameter. Measurements of reflection and transmission coefficients $S_{11}(f)$, $S_{21}(f)$ after the 180 deg power splitters as functions of frequency are performed in less than 0.5 seconds. The device top is then raised to its original position in 3-7 sec. The entire measurement sequence

requires about 20-30 sec. Left and right wrist circumferences are separately measured and recorded at a position just under the ulnar head.

Electronics and patient safety are addressed by both the low power of the system and the construction therein. All wiring connections are sealed, and all exposed electronics are isolated. There are two replaceable external fuses (7 V 3 A). For additional biological isolation, subjects could choose to wear a thin, disposable plastic glove to prevent any contact with the device. The device is periodically cleaned with alcohol swabs.

From the point of view of electromagnetic safety, the present device is equivalent to two low-power cellphones placed on either side of the wrist: one is transmitting, and another is receiving. The device introduces minimum radiofrequency energy into the wrist (0.1 W total power over a maximum time duration of 0.5 min). Such power is 6-30 times less than the power of a cellphone and is 10,000-100,000 times less than the power of an MRI radio-frequency coil. The U. S. Department of Health and Human Services, Food and Drug Administration, Center for Devices and Radiological Health, Division of Biomedical Physics accepts guidelines of the International Commission on Non-Ionizing Radiation Protection (ICNIRP) [81]. These guidelines state that the general-exposure local Specific Absorption Rate (SAR) should be less than 0.08 W/kg at 915 MHz [81], which is the center operating frequency of the device. The corresponding numerical simulation study performed with the commercial FEM software ANSYS Electronics Desktop 2019R1 and a CAD VHP-Female version 3.0 full-body computational human model [76] revealed that this condition is satisfied with a 10x safety margin.

In the research study reported below, the antennas have been connected to a portable Keysight FieldFox N9914A network analyzer to investigate and test the entire frequency band from 30 kHz to 2 GHz and to establish the most sensitive region(s) of operation. The typical operation setup is shown in Fig. 9 on the next page.

2.5. De-embedding Transmission and Reflection Coefficients

Since the radiofrequency device is contained in a protective enclosure, the S-parameters cannot be calibrated and measured directly at the power splitter ports. The microwave device was therefore calibrated along with the cables running to the network analyzer. This leads to oscillatory behavior of both $S_{11}(f)$ and $S_{21}(f)$. To eliminate these spurious oscillations, de-

embedding was performed after measuring S-parameters for each cable. For this purpose, the MATLAB RF Toolbox™ from MathWorks, Inc. was employed (function `deembedsparams`).



Fig. 9. Experimental setup connected to portable Keysight FieldFox N9914A network analyzer and performing measurements. Measurements of reflection and transmission coefficients $S_{11}(f)$, $S_{21}(f)$ as functions of frequency are performed in less than 0.5 seconds. The device top is then raised to its original position (3-7 sec). [6]

2.6. Pilot Study

After receiving Institutional Review Board (IRB) approval through Worcester Polytechnic Institute, the written informed consent from 72 subjects (ranging from 23-94 years old, 58 female, 14 male, 3 African American, 4 Hispanic, 64 Caucasian, cf. Appendix A) was obtained to participate in this study. All measurements were further performed in accordance with the relevant IRB guidelines and regulations.

Given a common fear of ionizing radiation, especially among elderly subjects, the authors did not enforce or require any extra DXA measurements. For every subject the following parameters were recorded:

- Reflection coefficient $S_{11}(f)$ (both magnitude and phase) from right and left wrists for the bottom antenna configuration after the 180 deg power splitter in the frequency range from 30 kHz to 2 GHz.
- Transmission coefficient $S_{21}(f)$ (both magnitude and phase) between the two antennas after the 180 deg power splitters and through right and left wrists, respectively, in the frequency range from 30 kHz to 2 GHz.

- Age, weight, height, left wrist circumference, and right wrist circumference.
- Family history of osteoporosis and history of bone fracture according to a verbal statement.

Initially, all subjects with de-identified data have been subdivided into five preliminary categories detailed in Appendix A:

1. **Category 1 (healthy young adults, 23-30 years old).** Unknown bone density but young age (≤ 30). **5 subjects in total** (2 female, 3 male).
2. **Category 2 (low risk factor category, 42-94 years old).** Unknown bone density (no DXA data) but (all together): no history of bone fractures, no medication, and no family history of bone fracture/osteoporosis. **32 subjects in total** (24 female, 8 male). These clinical risk factors can have a larger impact on fracture risk than one standard deviation decline in bone density [82], [83]. Therefore, we feel comfortable considering them at low risk without explicit BMD information.
3. **Category 3 (unknown risk factor category, 44-77 years old).** Unknown bone density (no DXA data) but at least one of the following: family history of osteoporosis, low BMI, history of bone fractures, women after menopause. **12 subjects in total** (10 female, 2 male).
4. **Category 4 (osteopenia or low bone density, 55-90 years old).** Confirmed osteopenic bone density (T-score between -1.0 and -2.4) according to the most recent DXA exam (obtained within the last year) and prescribed medications such as various calcium/magnesium supplements (600-1000 mg). **18 subjects in total** (17 female, 1 male).
5. **Category 5 (osteoporosis, 55-86 years old).** Confirmed osteoporotic bone density (T-score of -2.5 or below) according to the most recent DXA exam (obtained within the last year) and prescribed medications such as bisphosphonates. **5 Subjects in total** (5 female, 0 male).

2.7. Subject Selection for Dichotomous Diagnostic Test (Osteogenic/Osteoporotic vs Healthy)

In the interest of performing an unbiased study, we eliminated Category 3 (unknown risk factor category). As a result, we ended up with two groups (60 subjects in total) suitable for binary classification:

1. **Group 1 osteopenic/osteoporotic** (Categories 4 and 5 together, 55-90 years old, mean 77.5/STD 10.1). T-score of -1.0 or below according to the most recent DXA exam and prescribed medications. **23 subjects in total** (22 female, 1 male).
2. **Group 2 healthy** (Categories 1 and 2 together: low risk category, 23-94 years old, mean 60.2/STD 16.6). Unknown bone density (no DXA data) but young adults or (all together): no history of bone fractures, no medication, and no family history of osteoporosis. **37 subjects in total** (26 female, 11 male).

A single binary statistic (the Youden's J statistic) was then applied to these two groups to capture the performance of a dichotomous diagnostic test.

2.8. Data Processing for Entire Frequency Band – Transmission through the wrist

Fig. 10a shows the normalized transmission coefficient magnitude between the two antennas through left and right wrists in the 0-2 GHz frequency band for all 60 subjects selected for the dichotomous diagnostic test as described previously. Normalization means that we divide $|S_{21}(f)|$ by BMI and multiply it by subject age, that is $Age \cdot |S_{21}(f)| / BMI$. Red color corresponds to Group 1 while blue color corresponds to Group 2. One hundred and twenty frequency curves in total are shown in the figure.

The osteoporotic and osteopenic subjects more consistently indicate higher normalized transmission coefficients, while the healthy subjects more consistently indicate lower normalized transmission coefficients. In other words, the osteoporotic and osteopenic wrists become relatively more transparent to radio frequency signals. However, some curves in Fig. 10 locally overlap. An integral measure of the transmission coefficient may therefore be the best differentiator. Notably, the data for five young healthy subjects highlighted in magenta in Fig. 10b indicate the smallest “transparency” while the data for five osteoporotic subjects (T-score of -2.5 or below) highlighted in magenta in Fig. 10c indicate the nearly highest “transparency”.

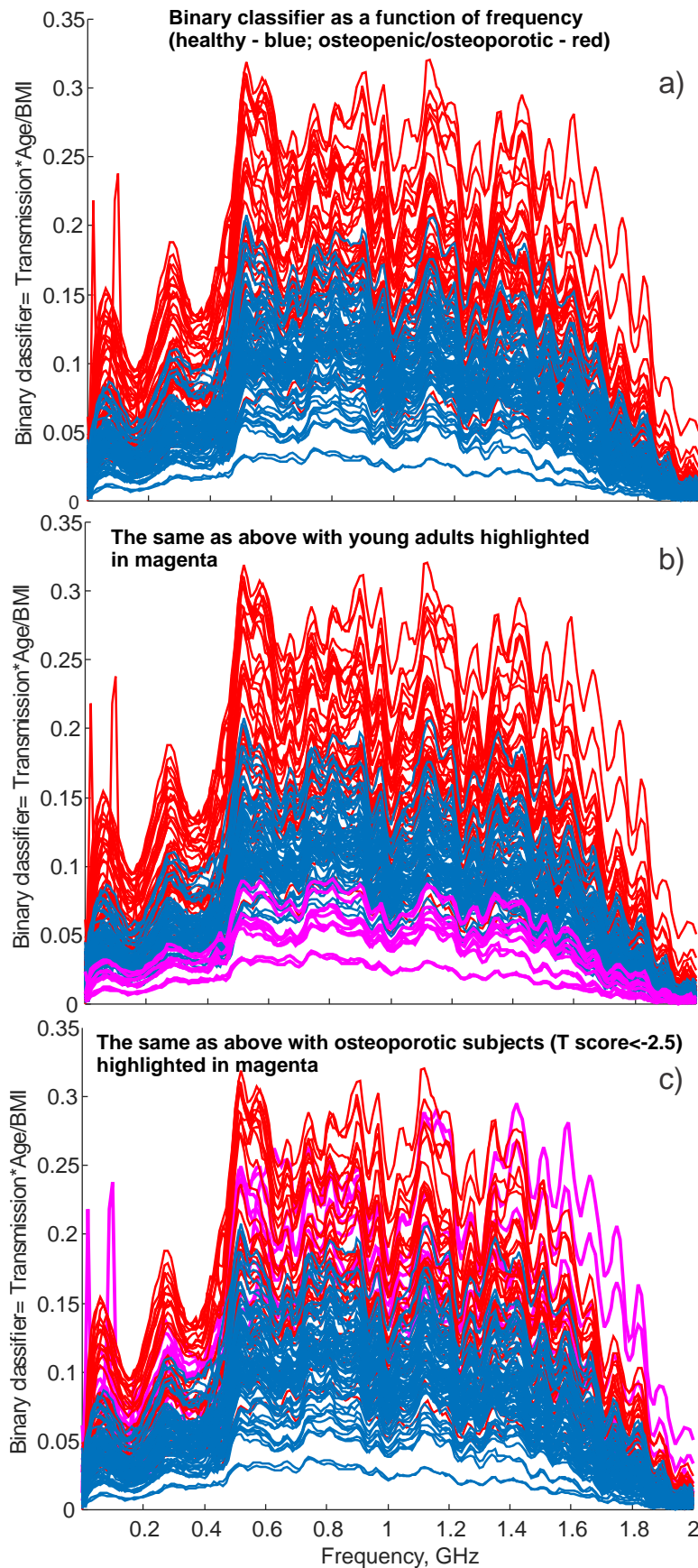


Fig. 10. (a) – Transmission coefficient $|S_{21}(f)|$ between the two antennas and through left and right wrists divided by BMI and multiplied by age in the frequency range 0-2 GHz for all subjects from Group 1 (osteopenic and osteoporotic) and Group 2 (healthy). Red corresponds to Group 1 while blue corresponds to Group 2. 120 frequency curves in total are shown in the figure. (b) – The same as in (a) but with the data for five young adults highlighted in magenta. (c) – The same as in (a) but with the data for five osteoporotic subjects (T score below -2.5) highlighted in magenta. [6]

2.9. Index Functions

Bone density presumably correlates with BMI and approximately inversely with age; osteoporosis mostly occurs in elderly women with a low BMI. Since the cohort mostly includes women, the authors could neglect the sex variable. Thus, for comparison purposes, the authors introduce a simple “natural” indicator, D_0 , of osteoporosis/osteopenia for the study participants in the form of the ratio of two clinical risk factors:

$$D_0 = \frac{Age}{BMI} \quad (1)$$

which does not require any measurements but should already approximately differentiate osteoporotic/osteopenic and healthy persons, respectively. Healthy conditions correspond to lower values of D_0 . Indicator D_0 will be normalized to its maximum value, that is

$$D_0 \rightarrow D_0/\max(D_0) \quad (2)$$

Now, the authors introduce the primary differentiator (index) in the form

$$D_1 = \frac{Age}{BMI} \times \int_{f_L}^{f_U} |S_{21}(f)| df \quad (3)$$

which additionally includes an integral of the transmission coefficient $S_{21}(f)$ from Fig. 6 over a certain frequency band from f_L to f_U . Indicator D_1 is obtained by averaging the data for both wrists. Indicator D_1 is also normalized to its maximum value as

$$D_1 \rightarrow D_1/\max(D_1) \quad (4)$$

Following the observations of Fig. 10, the authors suggest that indicator D_1 would better differentiate osteoporotic/osteopenic and healthy conditions, respectively, than indicator D_0 .

2.10. Data Processing for a Narrow Frequency Band of 0.1 GHz

Using the network analyzer for RF data acquisition and obtaining the entire spectrum in Fig. 10 is costly. Low-cost power meters with the center frequency from 0.5 to 1 GHz operating over the band of 0.1 GHz could be designed and/or purchased. Therefore, we restrict ourselves to a smaller frequency band in Eq. (3). We assume that the integration bandwidth is given by

$$f_U - f_L = 0.1 \text{ GHz} \quad (5)$$

We chose the center frequency of the band in such a way as to provide the best performance. To do so, we move the integration window with the width of 0.1 GHz in Fig. 10 from left to right. Then, we select such window positions where the ROC area and Youden's J index for the ROC (receiver operating characteristic) curve are maximized as shown in Fig. 11.

2.11. Youden's J index for Eq. (3). Finding optimum frequency band

Fig. 11a shows the maximum value of Youden's J index for each center frequency of the band. Here, an average absolute transmission coefficient $|S_{21}(f)|$ for both wrists of the subject is employed. The maximum value of Youden's J index corresponds to the optimum value of the empirical device calibration threshold or cutoff T . Threshold T differentiates the two states:

$$\textit{Osteopenic/Osteoporotic} \quad D_1 > T \quad (6a)$$

$$\textit{Healthy} \quad D_1 \leq T \quad (6b)$$

The most favorable frequency band is indicated by a vertical bar in Fig. 11, from 890 MHz to 920 MHz. The horizontal line in Fig. 11a-c shows Youden's J index for indicator D_0 given by Eq. (1). The global maximum value of Youden's J index for indicator D_1 achieved over the band from 890 to 920 MHz is 0.815 or 81.5%. The global maximum value of Youden's J index for indicator D_0 is 0.615 or 61.5%. The difference in these values reflects supplementary useful information obtained from radiofrequency data.

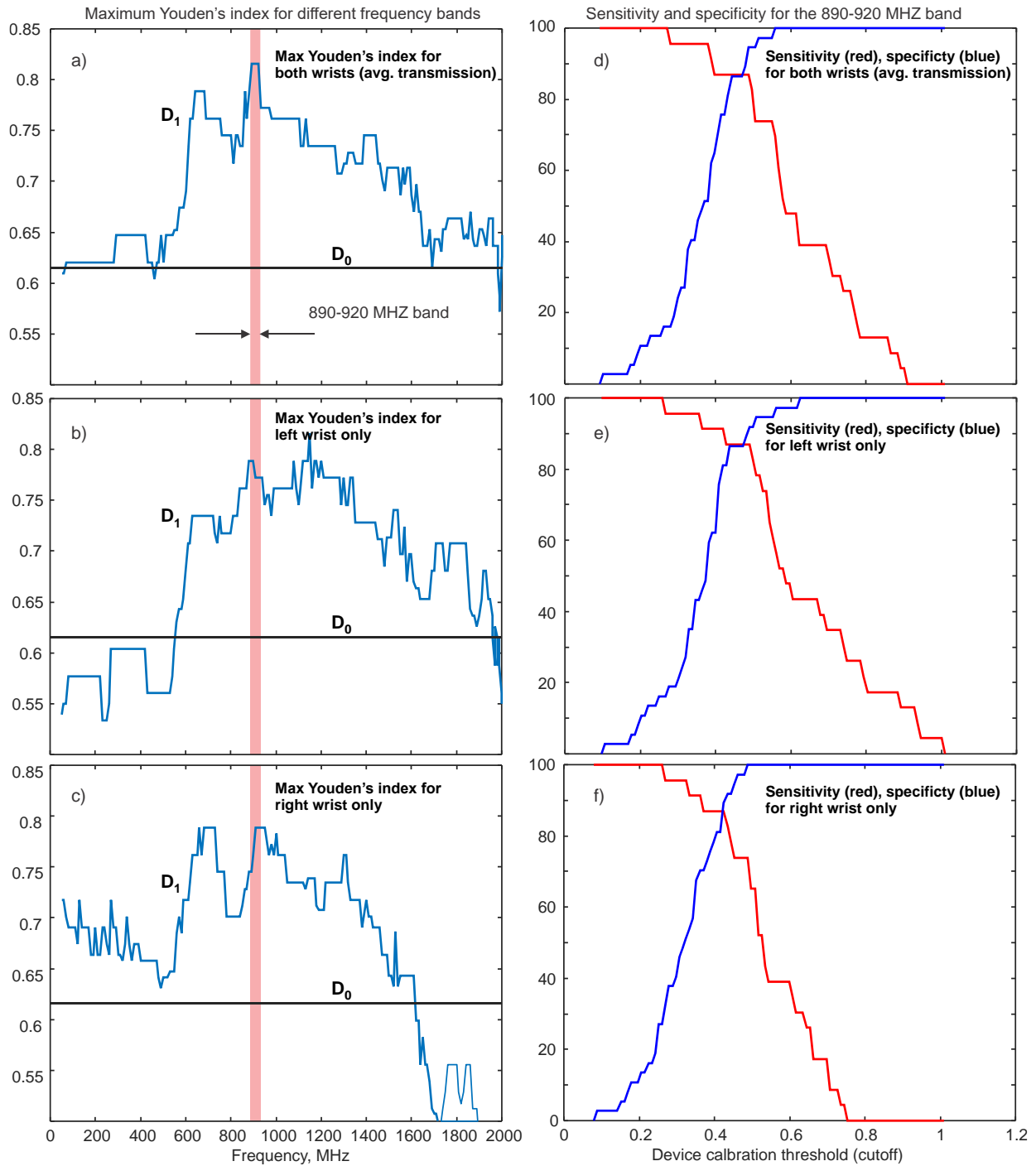


Fig. 11. (a) – Maximum Youden's J index for every center frequency of the moving 0.1 GHz band using the index given by Eq. (3). Average transmission coefficient for both wrists is used. (b) – The same as in (a) but only the transmission coefficient for the left wrist is used. (c) – The same as in (a) but only the transmission coefficient for right wrist is used. The most favorable band position indicated by a vertical bar is from 890 to 920 MHz. The straight horizontal line in (a – c) shows Youden's J index for the simple indicator D_0 given by Eq. (1). (d) – Sensitivity (red) and specificity (blue) corresponding to the band 890-920 MHz in (a). Both are given as functions of the device threshold value T in Eqs. (6). (e), (f) – the same as in (d) but only the transmission coefficient for the left or right wrist, respectively, is used. [6]

Fig. 11b shows the same result as in Fig. 11a but when only the transmission coefficient for the left wrist of every subject is used. Similarly, Fig. 11c uses the data for the right wrist only. The inclusion of information from both wrists leads to a more useful result than the information obtained from a single wrist, by measure of Youden's J.

2.12. Sensitivity and Specificity for the Optimum Frequency Band

Both sensitivity (red) and specificity (blue) are shown in Fig. 11d at the band center frequency of 900 MHz corresponding to the global maximum of Youden's J index in Fig. 11a. The x-axis is the device calibration threshold value T in Eqs. (6). One observes that we simultaneously reach the sensitivity of 87% and the specificity of 87% or better when the device is calibrated with the threshold value $0.44 \leq T \leq 0.49$ in Eqs. (6). This corresponds to the calibration threshold tolerance of $\pm 3\%$. Fig. 11e shows the same result as in Fig. 11d but when only the transmission coefficient for the left wrist of every subject is used; Fig. 11f uses the data for the right wrist only. The information from both wrists is evidently more beneficial than the information obtained from one single wrist.

For the present binary classifier, sensitivity for five severely osteoporotic subjects (T-score of -2.5 or below, indicated with magenta color in Fig. 10c) is 100%. Similarly, specificity for five young healthy adults (indicated with magenta color in Fig. 10b) is also 100%.

2.13. Improvement of antenna matching

The simplified numerical model of the human wrist used in antenna optimization does not consider realistic wrist composition, variations in tissue properties at different frequencies or tissue anisotropy. Therefore, we were unable to properly match antennas over the entire targeted frequency band from approximately 200 MHz to 2 GHz. Instead, an "average" matching to $10 - j5$ ohm was used. This is not entirely adequate (as shown by Fig. 12) and is a subject of possible improvement.

Matching an on-body antenna coupled with a power splitter (beamformer) over the wide frequency band (~ 200 MHz – 2 GHz or 10:1 in the present case) is a difficult task. Instead of performing further numerical simulations, the authors explored unmatched antennas to determine if useful data could be produced without explicitly matching the antenna at any given frequency, in the process accepting a decrease in transmitted power.

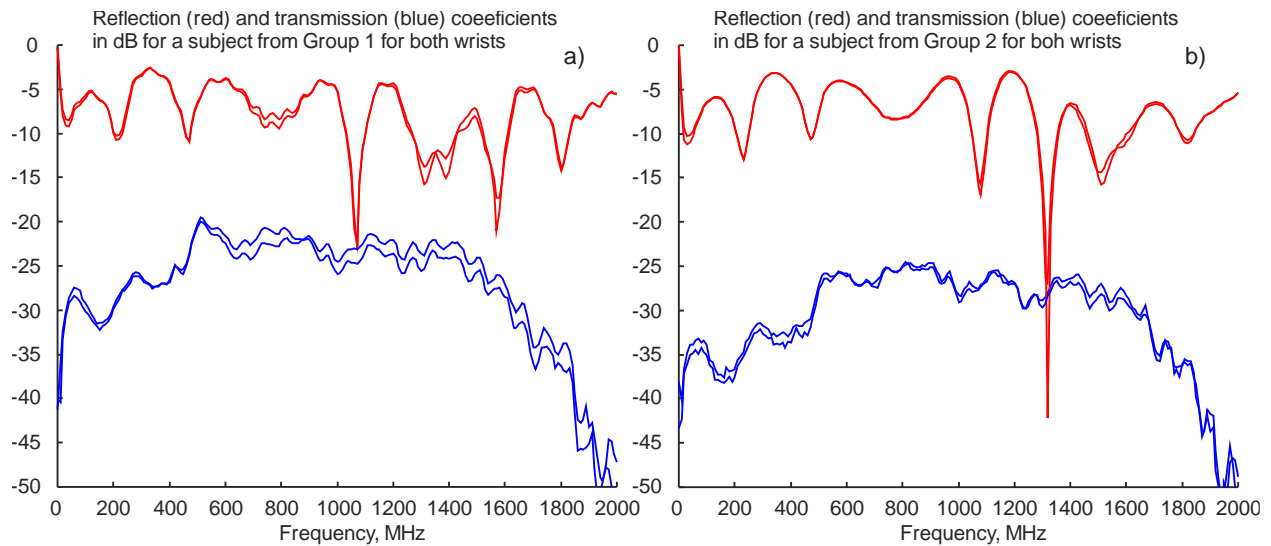


Fig. 12. (a) – Reflection (red) and transmission (blue) coefficients before normalization in dB for a typical osteoporotic subject (Group 1) for every wrist separately. (b) – The same coefficients for a typical healthy subject (Group 2). The right wrist typically indicates a lower transmission coefficient. [6]

2.14. Effect of surrounding tissue

As indicated already in Fig. 3a, the device measures an integral estimate of radio frequency propagation through the wrist. This integral estimate involves not only bone but also cartilage and soft tissues surrounding bone. Nevertheless, this estimate correlates quite well with both the clinical risk factors and the subsequent DXA data as shown in the present chapter. This is likely because a significant portion of the radio frequency signal path in Fig. 3a still passes through trabecular bone (as demonstrated in Fig. 7).

Another point is the small thickness of the fat layer around the wrist, perhaps the smallest when compared with other body regions. This small fat layer thickness does not support multipath (signal propagation along the fat layer [84] instead of through the bone). Furthermore, the wrist composition is less significantly affected by age. In [85], skin thickness and subcutaneous fat thickness were measured on the back of the hand near the wrist between the second and third metacarpal and above the third metacarpal bone. The average values for young adults were 0.5 and 0.6 mm, respectively. With aging, the average skin thickness did not change significantly while the average subcutaneous fat thickness decreased by approximately 30% (from 0.6 to 0.4 mm) [85]. This is in contrast to other parts of the body where fat accumulation with age may be very significant [86]. Finally, an additional

factor might involve accompanying changes in cartilage properties and muscular tissue properties which may be specific for the osteopenic/osteoporotic subjects.

2.15. Effect of wave diffraction around the wrist, surface waves

The effects of both wave diffraction and the associated surface waves around the wrist have been found to be small for the present antenna setup at 900 MHz as well as at 600 and 1200 MHz. The corresponding simulation results shown in Fig. 7 reveal that, for the dual antiphase patch antenna setup, the bulk of the radiated power propagates through the center of the wrist and the bone marrow toward the receiver antenna while a vanishingly small power flow is observed close to the perimeter of the wrist.

The ripples in Fig. 10 are due to non-adequate antenna matching over the entire frequency band for a variety of different subjects. The proof of this is given in Fig. 12 where the ripples of S21 correlate with the ripples of S11 (a local minimum of S11 corresponds to a local maximum of S21) all the way up to at least 1 GHz.

An antenna backlobe observed in Fig. 7c has been found to provide a minimum multipath effect that is below noise floor. The proof uses experiments with the RX antenna somewhat lifted up above the wrist. In every tested case, the corresponding transmission coefficient was below -50 dB over the entire band. This value was selected as the noise floor. Only when the TX antenna was pressed against the wrist were the reported transmission coefficients on the order of 20 to 40 dB observed.

2.16. Results for male and female subjects

The selected study groups were composed primarily of women (representative of the patient population that gets osteoporosis). However, results for one osteoporotic male subject and eleven control male subjects were also compiled. The separate results for the two genders are as follows:

- For female subjects: sensitivity of 86% and the specificity of 85% when the device is calibrated with the threshold value $0.44 \leq T \leq 0.49$ in Eqs. (6).
- For male subjects: sensitivity 100% and specificity of 90% when the device is calibrated with the threshold value $0.44 \leq T \leq 0.49$ in Eqs. (6).

2.17. Results for healthy young subjects

We have intentionally included the young healthy adults into control to demonstrate a 100% specificity for this subgroup. If we were to exclude them, nearly the same results for sensitivity and specificity (approximately 87%) would be obtained. However, the control group will now have a higher mean age of 65.3 with STD of 10.9.

2.18. Radio frequency data adds supplementary information to clinical risk factors

The index function used in this chapter is not the radiofrequency transmission coefficient alone, but the transmission coefficient multiplied by age and divided by BMI. The inclusion of these two clinical risk factors increases both sensitivity and specificity. At the same time, the inclusion of radiofrequency transmission data adds useful supplementary information to the clinical risk factors. This is best seen in Fig. 11 where such an inclusion increases the Youden's index by 20% (from 61.5% to 81.5%) when the frequency band from 890 to 920 MHz is considered. Non-normalized data for the sole transmission coefficient are discussed in more detail in Section Chapter 3. Using Neural Networks to Improve Diagnosis from Wrist Tester on page 43.

2.19. How much supplementary information is contained in "effective" wrist thickness?

The index function used in this chapter does not involve the wrist thickness or its circumference. On the other hand, the transmission coefficient clearly increases for a thinner (more likely osteopenic/osteoporotic) wrist and decreases for a thicker (more likely healthy) wrist. One may therefore suggest that the bulk of added radiofrequency information is simply the "effective" (from the viewpoint of radiofrequency propagation) overall wrist thickness, which may be considered as another added clinical risk factor.

While this is partially true, the radiofrequency measurements still provide more useful information than the simple mechanical measurement of the wrist thickness or its circumference. The first proof is given in Fig. 13. This is a replica of Fig. 11a where we additionally plot the Youden's index for the natural indicator D_0 from Eq. (1) modified by the mechanical measurements of the wrist circumference (mean of both wrists was taken), which were performed for every subject, that is

$$D_{0\text{mod}} = \frac{Age}{BMI \cdot \text{wrist circumference}} \quad (7)$$

One observes that the performance of D_0 improves but the radiofrequency data remain more informative in the frequency band from 600 to 1600 MHz where the antenna matching is the best.

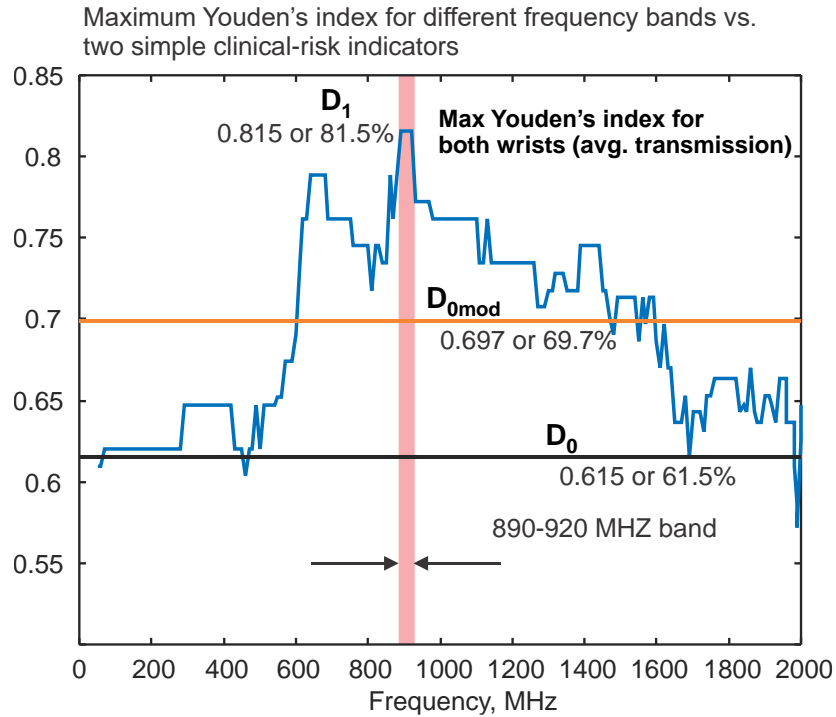


Fig. 13. Blue - maximum Youden's J index for every center frequency of the moving 0.1 GHz band using the index given by Eq. (3) with radiofrequency measurements. Average transmission coefficient for both wrists is used. Straight horizontal lines show Youden's J index for the simple indicator D_0 given by Eq. (1) and its modification $D_{0\text{mod}}$ from Eq. (7). [6]

The second proof is given in Fig. 14, the non-normalized data for the sole linear transmission coefficient but multiplied by the wrist thickness (more precisely – by the wrist circumference). This is done to undo the effect of the mechanical thickness, assuming approximately linear with distance radiofrequency damping. The differentiation between healthy and osteopenic/osteoporotic groups becomes poorer, but it is still in place.

Three fourths of the measured information have not been used for data processing in the present chapter. The non-processed data include phase information for both transmission

and reflection coefficients and the amplitude information for the reflection coefficient. Our study indicates that some classifiable phase variations may be observed for the phase of the transmission coefficient. More advanced machine learning algorithms might perhaps help to solve this problem.

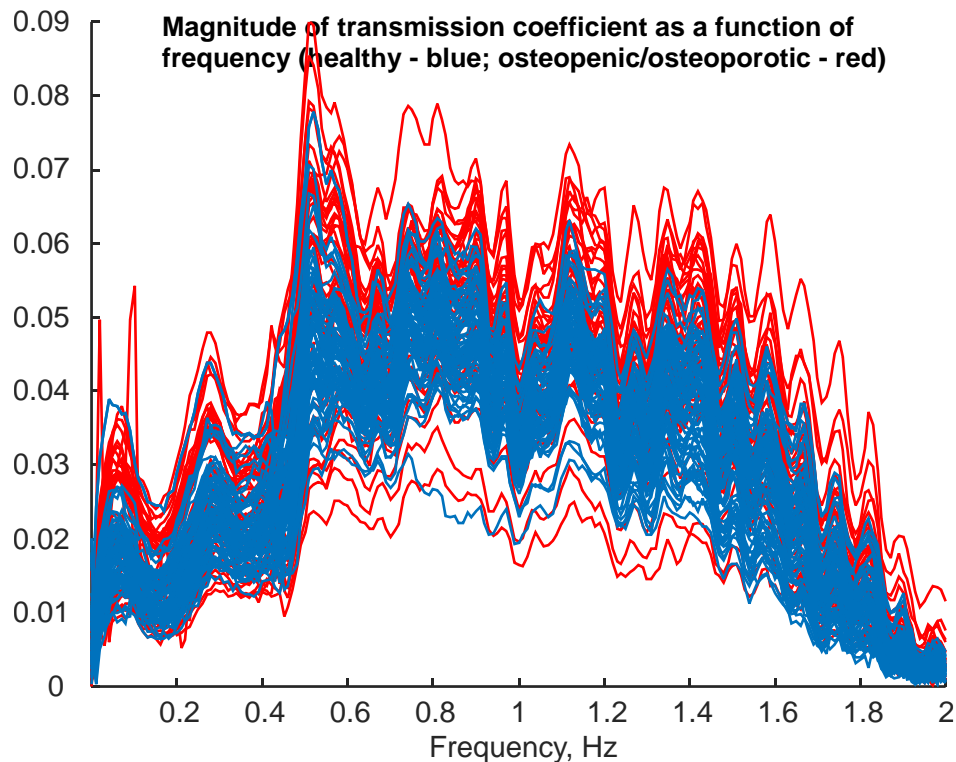


Fig. 14. Magnitude of non-normalized transmission coefficient $S_{21}(f)$ multiplied by wrist circumference (and normalized by maximum circumference). Subjects from Group 1 (osteopenic/osteoporotic) are marked red and subjects from Group 2 (healthy control) are marked blue. Total 120 curves are shown in the plot. [6]

2.20. Osteoporosis Detection in Other Body Compartments

The authors have undertaken preliminary efforts in applying this technology to other body compartments. Osteoporosis is most often problematic in the hip and the spine, and the authors have chosen to recreate the setup used here on the wrist, but on a subject's hip. Preliminary investigation reveals that such a device is possible, though the hip has challenges that are not significant at the wrist. Additional details are covered in Appendix B on page 88.

At the time of writing, the authors have not investigated applying this technology to the spine. The spine's location inside the body does not lend itself to application of the 1-pixel imaging

technique described in this chapter due to surface-propagating waves and the directivity of the antennas.

Dual antiphase antennas produce waves that propagate along the surface of the skin. These waves are large compared to those that propagate through the body and arrive at the receiver faster due to traveling through air instead of the lossy human body. To minimize the effect of these waves, this study has placed the antennas on opposite sides of a comparatively thin but wide body compartment, so the surface waves must travel a longer distance compared to the penetrating waves.

Unless these surface waves can be addressed, dual antiphase antennas and most other on-body antennas cannot be reliably placed adjacent to one another without phased-array processing to separate the surface wave from the penetrating wave. Addressing these surface waves will be the subject of another work.

2.21. Summary

In this chapter, a potentially low-cost, through-transmission radiofrequency device to detect low bone density conditions was designed, constructed, and tested. The device uses novel on-body antennas (dual antiphase patch antennas) connected to both sides of the human wrist under controlled applied pressure. It was observed that osteopenic and osteoporotic subjects more consistently indicate higher normalized transmission coefficients, while reduced risk subjects more consistently indicate lower normalized transmission coefficients, either normalized or not.

A pilot study with 72 subjects has been performed. For the dichotomous diagnostic test, we have selected 60 study participants (23-94 years old, 48 female, 12 male) who could be positively differentiated between the osteopenic/osteoporotic and healthy complementary states, respectively. The osteopenic state was determined based on a DXA T-score between -1 and -2.5 ; and the osteoporotic state was determined based on a DXA T-score below -2.5 . No DXA measurements have been performed for healthy subjects but all subjects from this category passed all of the following clinical risk-factor tests: no history of bone fractures, no medication, and no family history of bone fracture/osteoporosis. The band-limited integral of the transmission coefficient averaged for both wrists multiplied by age and divided by BMI has been used as an index.

Youden's J statistic was applied for center band frequencies in the range from 890 to 920 MHz. For a 100 MHz wide frequency band, the maximum Youden's J index is 81.5%. Both the sensitivity and specificity simultaneously reach 87% given the calibration device threshold tolerance of $\pm 3\%$. At the same time, sensitivity for severely osteoporotic subjects (DXA T-score of -2.5 or below) is 100% while specificity for young healthy adults is also 100%.

The authors' approach correlates well with the available DXA measurements and has the potential for screening patients at risk for fragility fractures. The inclusion of radiofrequency transmission data adds significant supplementary information to the available clinical risk factors.

Chapter 3. Using Neural Networks to Improve Diagnosis from Wrist Tester

This chapter covers the first primary contribution: the use of a neural network to classify subjects as healthy or osteoporotic based on data collected by the device described in the previous chapter. The perceptron-style neural network was first published in 1957 by Frank Rosenblatt [87]. Since then, neural networks have proven beneficial in the analysis of complex datasets involving frequency spectra [88], [89], [90]. Additionally, the diagnosis of osteoporosis using neural networks is not unprecedented [91], [92], [93], [94]. Prior works using neural networks to predict osteoporosis diagnosis focus on the aggregation of data from multiple diagnostics such as DXA and X-ray imaging [91], [93], [94], and the aggregation of risk factors [91], [92], [93].

In the present pilot study, we have included additionally collected subject data (7 new subjects) as compared to the previous chapter and have employed a neural network approach to process the previously obtained and new data. We hypothesize that the incorporation of a neural network classifier will significantly improve the predictive power of the presented system compared to the initial method based on a simple threshold binary classifier approach. The data collected from the device is an entire frequency spectrum of a complex scalar propagation coefficient through the wrist ($S_{21}(f)$). A neural network classifier sorts the spectra from different subjects as osteopenic or healthy. The network is trained using one subset of the collected data and validated with a separate subset. The neural network provides a binary predictor based on the spectrum it is given, as to whether the subject is healthy or osteopenic/osteoporotic.

3.1. Differences Between Breast Cancer and Osteoporosis Application

Several studies applying neural networks to the problem of breast cancer detection exist, but their methods are not directly applicable to osteoporosis detection using the present data. In most breast cancer detection applications, the problem is both detection and location of the tumor, whereas in the present study we focus only on the detection of osteoporosis [95], [96], [97], [98]. This limitation of scope is due to the imaging device itself, from the previous chapter, produces a single spatial “pixel” rather than a full 2-D or 3-D tomographic reconstruction of the wrist in the manner of many breast cancer detection studies. This, in turn, changes the

type of neural networks that are appropriate for the application. Breast cancer detection neural networks work similarly to image classification neural networks in that they are typically made of at least two stages: one stage to reduce the data from its original form into a set of features, and another stage to perform classification and/or location based on these features [95], [97], [98]. Each of these stages can have multiple layers. By contrast, the osteoporosis data needs no dimensionality reduction. Appendix C shows that some of the techniques that work well for breast cancer detection do not work well for the osteoporosis data.

3.2. Radiofrequency Measurement Device

Fig. 15a shows the arrangement of the two antennas transmitting through the wrist. These two antennas, Fig. 15b, are placed on the superior and inferior flat sides of the wrist adjacent to the position of the ulnar head. They are held in place with 1 kg of force during the recording of the measurements. The radiofrequency signal travels from the transmit antenna, through skin, bone, cartilage, and soft tissue to arrive at the receive antenna. Each of these layers provides some degree of attenuation and scattering; in the wrist, bone is significant compared to other body compartments. A network analyzer, Fig. 15c, measures the transmission coefficient $S_{21}(f)$ over the 300 kHz to 2 GHz range. This transmission coefficient is correlated to osteopenic and osteoporotic conditions. Details of the design of the system have been presented in the previous chapter [6].

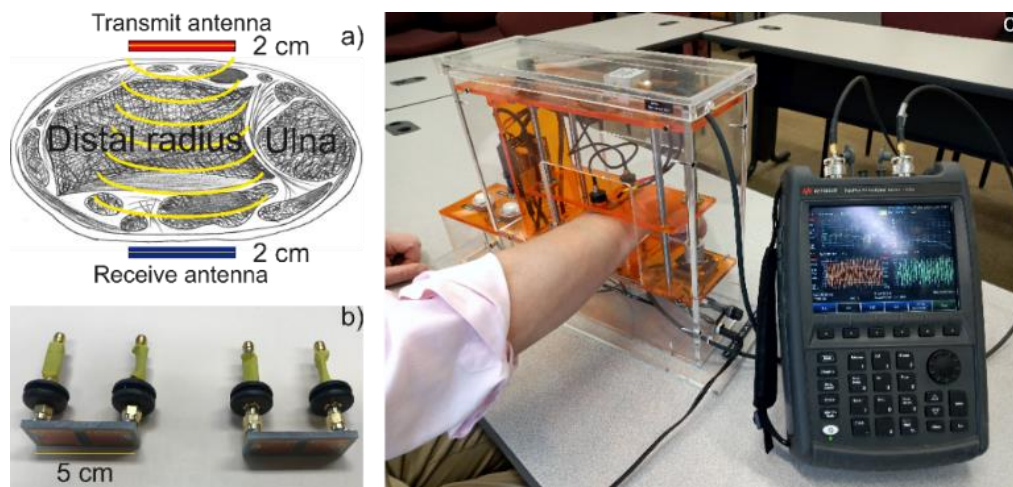


Fig. 15. (a) – Idealized diagram illustrating antenna placement on both sides of a human wrist. (b) – Transmit and receive dual antiphase patch antennas with individual lumped-component matching networks. (c) – Wrist tester device demonstration. Antenna length (along the wrist) is 5 cm; antenna width (across the wrist) is 1.8 cm. The antennas are fed in antiphase by a portable network analyzer and positioned by a lead screw for consistent 5 psi of pressure during measurement.

3.3. Data Collection

After receiving Institutional Review Board (IRB) approval (IRB-19-0123) through Worcester Polytechnic Institute on Oct. 1, 2018, written informed consent was obtained from 80 subjects to participate in this pilot study (age range 23-94 years old, 60 female, 20 male). All measurements were further performed following the relevant IRB guidelines and regulations. 72 subjects were measured in the previous section [6], and 8 new subjects were added for this chapter. From 80 subjects, we selected 67 subjects suitable for a dichotomous diagnostic set:

Group 1 (Osteopenic/Osteoporotic): 27 subjects (24 female, 3 male). Subjects were characterized by a T-score less than -1 taken within one year. Subjects with a T-score less than -2.4 were considered osteoporotic while other subjects were considered osteopenic. Subjects aged from 55 to 90 years with a mean of 77.5 and a standard age deviation of 10.1 years.

Group 2 (Healthy): 40 subjects (26 female, 14 male). Subjects in this group did not necessarily have a known T-score, but instead were characterized by having none of the following risk factors: a history of bone fractures, medication for bone-related diseases, a family history of bone fractures, and/or osteoporosis. Subjects aged from 23 to 94 years with a mean of 60.2 and a standard age deviation of 16.6 years. It is noteworthy that these clinical risk factors can have a larger impact on fracture risk than one standard deviation decline in bone density [82], [83]. Therefore, we are comfortable considering them at low risk without explicit BMD information.

Location on the body of DXA tests and ongoing medications were not considered when assigning subjects to the groups.

Each subject's data consists of their wrists' circumferences in cm and four 201-point spectra: the transmission coefficient (S_{21}) and the reflection coefficient (S_{11}) for both left and right wrists. Fig. 16A shows the magnitude of the transmission coefficient, $|S_{21}(f)|$ for 201 frequency sampling points between 300 kHz and 2.0 GHz. Group 1 is plotted in red, and Group 2 is plotted in blue. Fig. 16B has seven young subjects (age 44 and below) highlighted in magenta. Fig. 16C has five osteoporotic subjects with a DXA T-score below -2.4 highlighted in magenta.

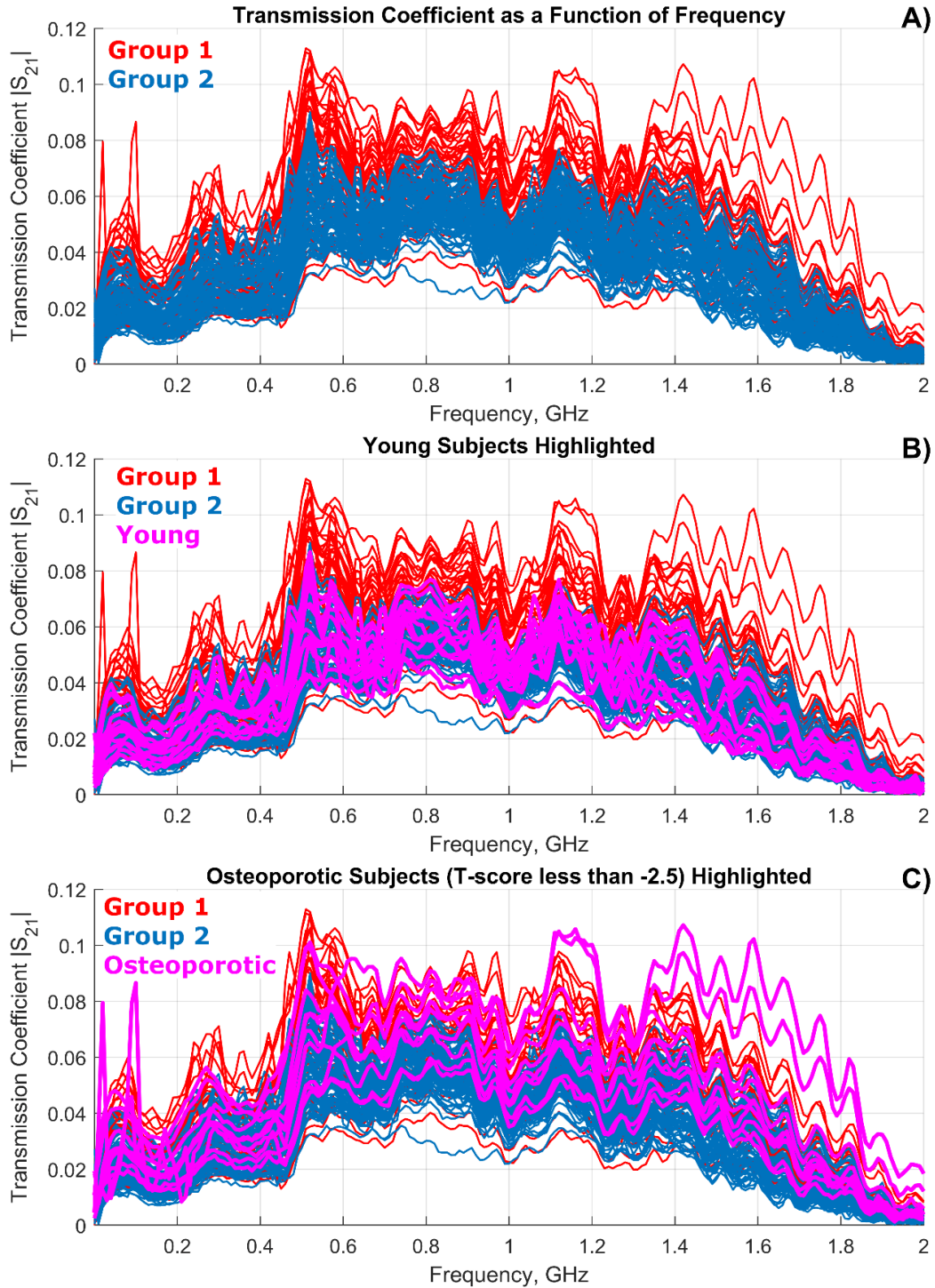


Fig. 16. (a) – Transmission coefficient $|S_{21}(f)|$ between the two antennas and through left and right wrists the frequency range 0-2 GHz for all subjects from Group 1 (osteopenic/osteoporotic) and Group 2 (healthy). The red color corresponds to Group 1 while the blue color corresponds to Group 2. 160 frequency curves (both arms for all 80 subjects) in total are shown in the figure. (b) – The same as in a) but with the data for seven young adults highlighted in magenta. (c) – The same as in a) but with the data for five osteoporotic subjects (T score below -2.5) highlighted in magenta.

The network analyzer recorded each spectrum as two components: magnitude and phase. For use with the neural network, the magnitude and phase were combined to give the complex number representation (real and imaginary component for each point) of each spectrum.

An additional set of data was created by normalizing the raw data described in the paragraphs above by risk factors of osteoporosis. The normalization factor was the subject's age divided by their body mass index, as used in Eq. 8 below to calculate the normalized S_{21} spectrum.

$$S_{21N} = D_0 S_{21} = \frac{Age}{BMI} S_{21} \quad (8)$$

3.4. The Perceptron

The original perceptron is a statical model to approximate the behavior of an animal or human neuron or set of neurons [87] which was implemented as a standalone electrical circuit [99], which was derived from the work of McCulloch and Pitts during the second world war [100]. In the context of modern machine learning for classification, the definition narrows to the combination of a weight and bias with some sort of activation function. The weight and bias are trainable, meaning that the back propagation training algorithm increases or decreases their values based on whether the classification result was correct for a given member of the training data set. While linear perceptrons have been investigated, modern networks use the activation function encourages their result to saturate, thereby giving an output that is closer to binary than would be achievable with just weights and biases. On its own, the perceptron can only solve linearly separable problems. Cascaded chains of perceptrons, however, can solve more complex problems, such as classifying data reliably despite class overlap.

3.5. Neural Network Topology

The neural network used to generate the binary classifier was a multilayered network based on a Multi-Layer Perceptron (MLP) classifier implemented using the MATLAB Deep Learning Toolbox™ (MathWorks, Inc, Natick, MA, USA). Fig. 17 shows a flow diagram of this neural network. A `featureinput` layer read in the spectrum. The first 50% dropout layer, `dropout_2`, prevented overfitting of the first fully-connected layer (`fc_2`) by setting each feature to 0 with a 50% probability. `fc_2` had unit learn rate factors for all weights and biases, its weights were L2 normalized, and its biases were not. Its weights were initialized using Glorot's algorithm [101]

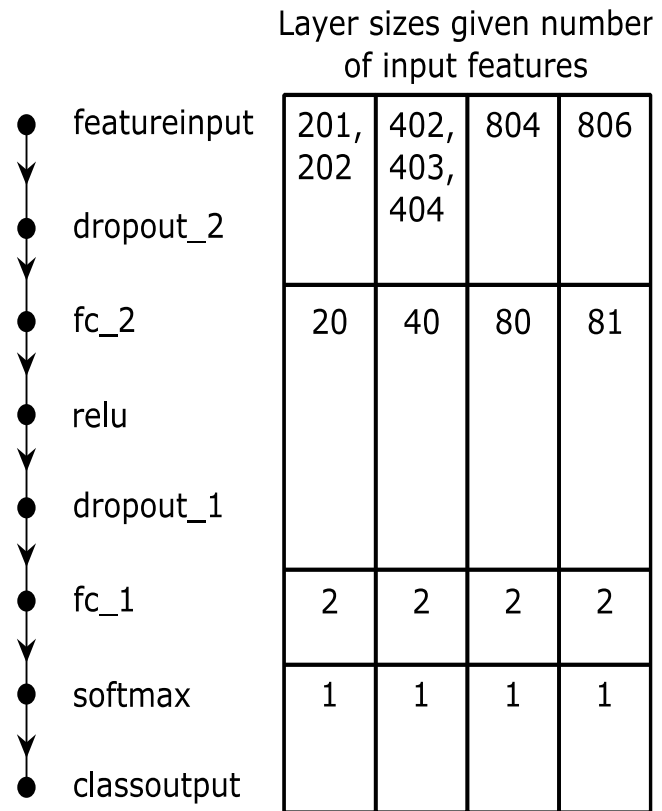


Fig. 17. MLP classification neural network flow diagram featuring two fully connected layers.

and its biases were initialized to 0. reduced the number of features according to Eq. 9, where N_{in} is the number of input features (equal to the number of points in the spectrum for this layer) and N_{out} is the number of neurons and output features from the layer.

$$N_{out} = \text{nint}(N_{in}/10), \quad 201 \leq N_{in} \leq 806 \quad (9)$$

A `relu` activation function separated the first and second layers and the second 50% dropout layer, `dropout_1`, prevented the second fully-connected layer from overfitting. This layer, `fc_1`, reduces the number of features from N_{out} to 2. `fc_1`'s learn rate factors and L2 normalization settings were identical to `fc_2`'s. Those two features are compared using a `softmax` function to determine the predicted classification (Group 1 or Group 2) for the subject. All non-mentioned parameters were left at their default values.

The final size of the vector presented to the neural networks depended on how the arms of the subject were being combined. The longest was 806 features when the complex arm

spectra (402 features each) and both wrist circumferences were concatenated. The shortest, at 201 points, was made from a single spectrum (magnitude or phase).

3.6. Training, Validation, and Classification

Three methods of combining the spectra from the left and the right arms to generate a single diagnosis for the subject were attempted. First, the left and right arm spectra were averaged before being processed by the neural network. Second, the left and right arm spectra were concatenated to form a double-length spectrum. Third, each arm's spectrum was presented separately to the neural network and the results were combined manually during postprocessing. Neural networks were trained for all combinations of data features using all three arm combination methods.

These neural networks were trained using the same parameters regardless of their number of input features. All networks were trained for 1000 epochs. To evaluate the overall usefulness of a specific configuration of input data, the neural networks were analyzed using a leave-one-out cross-validation scheme. Under this scheme, the subjects were randomly distributed between 7 subsets while maintaining roughly proportional numbers of Group 1 to Group 2 for either 9 or 10 subjects in each subset. The neural network would then be trained 7 times using each subset as the validation data once while all 6 other subsets were used as training data. Therefore, each input data configuration resulted in 7 trained neural networks of identical size each with a different validation data set. The mean of the resulting sensitivities, specificities, and accuracies from these 7 networks was used to characterize the performance of that input data configuration. Another series of tests using 10 subsets (6 or 7 subjects each) was attempted but did not yield results significantly different from the 7-subset tests.

The case wherein the two arms of each subject were presented separately to the neural network required an extra step after classification before the performance could be evaluated on a subject-by-subject basis. If both arms of a subject yielded the same classification, that classification was accepted. In the case of a conflict, the arms' results were combined using each of four schemes: keep left, keep right, keep osteoporotic, keep healthy. In addition to the recombined results, the statistics were also computed as if each arm belonged to a separate subject.

3.7. Results for Non-Normalized Data

Complex spectra produced the best results for raw data; magnitude spectra results are given for reference comparison. Combined magnitude and phase or phase-only number formats did not produce results worth including. Additionally, concatenating the arm spectra did not produce results worthy of inclusion. Using only the left or right arm of a subject produced results similar to those when the arms' spectra were averaged.

Table 1: Statistics for neural networks trained from raw (non-normalized) transmission data. The first 4 rows refer to networks trained using 134 subjects with 1 arm each while the last 4 rows refer to neural networks trained using the mean of the left and right arm spectra for each of the 67 subjects. Both cases were investigated with and without a feature for the subject's wrist circumference concatenated to the end of the spectrum.

Features	Subjects	Circumference	Format	Sensitivity	Specificity	Accuracy	Youden's J
L&R arms' spectra as separate 'subjects'	134	Concatenated	Complex	0.827	0.940	0.898	0.768
			Magnitude	0.780	0.917	0.867	0.696
		None	Complex	0.798	0.940	0.889	0.738
			Magnitude	0.780	0.929	0.875	0.708
Mean of arm spectra	67	Concatenated	Complex	0.690	0.905	0.824	0.595
			Magnitude	0.631	0.929	0.817	0.560
		None	Complex	0.690	0.905	0.824	0.595
			Magnitude	0.631	0.905	0.803	0.536

Table 1 shows the results of training the neural network using the output of the device directly. The only pre-processing involved in this data was done to put the complex data into the appropriate numerical representation – magnitude and/or phase versus complex number.

3.8. Results for Normalized Data

Table 2 shows the results of training the neural network using the data that was normalized according to Eq. 8. First, the complex data was converted to the appropriate numerical representation – magnitude and/or phase versus complex number – then Eq. 8 was applied to generate the values for the neural network.

Additionally, Fig. 18 shows a comparison of methods for recombining the classification results from the 134 single-armed 'subjects' from the highlighted row in Table 2 back into the 67 subjects that originated them. The same operation was also run using the data from Table 1 and similar performance was observed.

Table 2: Statistics for neural networks trained from transmission data that was normalized according to Eq. 8. The first 4 rows refer to networks trained using 134 subjects with 1 arm each while the last 4 rows refer to neural networks trained using the mean of the left and right arm spectra for each subject. Both cases were investigated with and without a feature for the subject's wrist circumference concatenated to the end of the spectrum.

Features	Subjects	Circumference	Format	Sensitivity	Specificity	Accuracy	Youden's J
L&R arms' spectra as separate 'subjects'	134	Concatenated	Complex	0.804	0.940	0.890	0.744
			Magnitude	0.804	0.917	0.875	0.720
		None	Complex	0.804	0.964	0.904	0.768
			Magnitude	0.780	0.917	0.867	0.696
Mean of arm spectra	67	Concatenated	Complex	0.810	0.929	0.884	0.738
			Magnitude	0.845	0.905	0.883	0.750
		None	Complex	0.762	0.952	0.883	0.714
			Magnitude	0.798	0.905	0.867	0.702

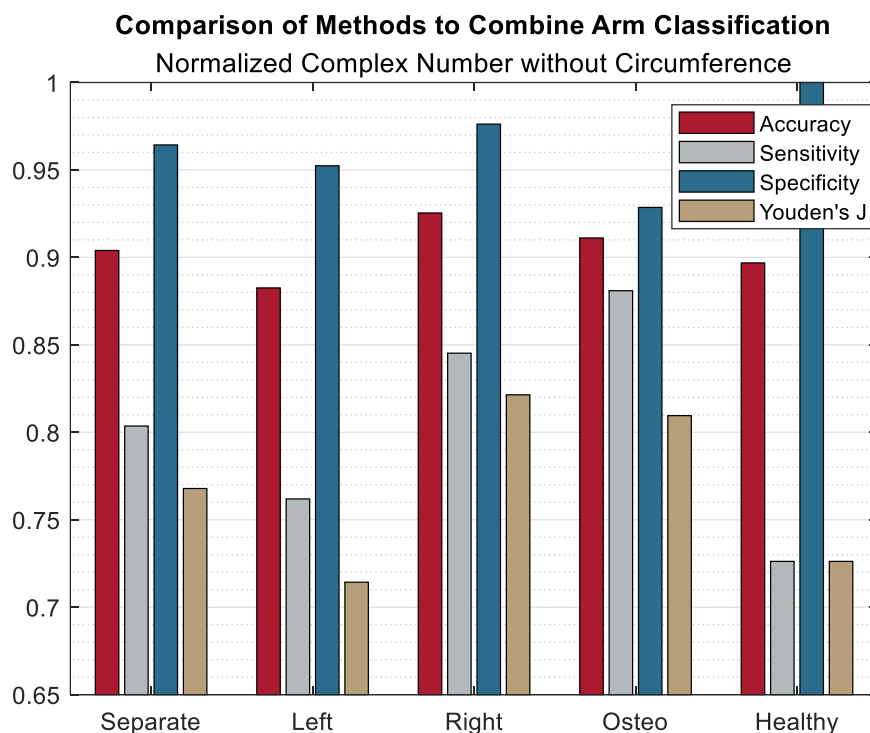


Fig. 18. Comparison of methods for recombining 134 single-arm subjects to provide one classification per subject. 'Separate' statistics are for the 167 single-arm 'subjects' while the other bar sets are sorted by what measurement was kept in case of a mismatch between the classification of the left and right arms' data. 'Left' and 'Right' resolved mismatches by taking the result from the left or right arm, respectively. 'Osteo' classified all mismatched subjects as Group 1 and 'Healthy' classified all mismatches as Group 2.

In this pilot study, we have found that a neural network trained with the complex frequency spectrum of radio wave propagation through the wrist and with the wrist circumference may serve as a promising predictor tool for detecting osteopenic/osteoporotic conditions on the wrist. Other studies have shown a strong correlation between bone density measurements in the arms, hip, and spine [102], [103]. Raw non-normalized data for the transmission coefficient through both wrists have been used as an input, without any normalization. This is in stark contrast to our initial study [6], where the processed data included the risk factors as well. In [6], a simple threshold binary classifier was used, which is essentially equivalent to checking the area under the entire frequency curve in Fig. 16 for every subject.

3.9. Limitations of the Study

All subjects in Group 1 had a DXA exam within 1 year of measurement, but the location of that exam and any following medications were not considered. Most Group 1 subjects were 70 years or older.

- Subjects in Group 2 did not necessarily undergo a DXA measurement. Additionally, fracture data since our measurements were taken is not available for the majority of Group 2. Many of the subjects in Group 2 were young adults, age 18-25.
- 13 subjects were not categorizable into Group 1 or Group 2 by all of their metrics simultaneously and were not considered for this chapter. For example, an elderly subject without a DXA exam in the past year.
- The study considers the same single configuration of the measurement apparatus applied to two single body compartments (wrists).

Due to the lack of DXA measurements for many subjects in Group 2, we state only a partial similarity between our classification and DXA measurements. Incomplete fracture histories for Group 2 between the time of measurement and time of writing prevent any conclusions based on fracture history. Similarly, the lack of a T-Score for the healthy subjects precludes the training of a regression network and therefore this study is limited to simple classification without the ability to provide a confidence estimate. A further study with new data would be required to provide the data necessary to train a regression network to provide positive and negative predictive values.

Age differences between subjects can influence fat and muscle composition as well as bone composition, which could affect the classification. Different body compartments are

composed of different amounts of fat, bone, and muscle so techniques that work well in one (for example the wrist, which is mostly bone) may not be directly applicable (as of today) to other more complex areas, such as the hip or spine. Because Group 2 had 10 more subjects than Group 1, sensitivity for a given trial is not as precise as specificity. We have used leave-one-out cross-validation to reduce the effects of this in our overall results.

This chapter only discussed results from a two-layer perceptron classifier working only with experimentally collected data. Additional experiments with other types of machine learning, including methods by which to reduce the number of features needed for classification, and data augmentation techniques are discussed in Appendix C on page 99. These results were omitted because they are only partially complete. Regardless, some limited conclusions may still be drawn from them, hence their inclusion. In brief, the data augmentation suggests that the performance of the classifier observed in this chapter can be improved by the collection and usage of additional data. Further, the PCA and feature selection proved not to be capable of producing results better than those from the perceptron network, though the corresponding visualizations offer some explanation as to why classification of this data is a nontrivial problem.

3.10. Fractures in Group 1

BMD data by DXA correlate with fracture risk but the correlation is not strong. To investigate this conclusion further, we collected data on fractures for subjects in Group 1 (osteopenic/osteoporotic). Except for one subject who deceased, two out of the 27 have experienced fractures over the last three years; one of those subjects experienced a fracture twice. All three cases were hip fractures. Four other elderly subjects in that group experienced falls without bone fractures over the last three years.

3.11. Discussion of Non-Normalized Data

The trained neural network provides sensitivity and specificity values of ~83% and 94%, respectively. The specificity compares favorably to the sensitivity and specificity provided by the inclusion of risk factors (both 87%), presented in Chapter 2. Dual Antiphase Patch Antenna Design and Application in the UHF Band [6]. The increase in the specificity obtained in the present chapter is a significant advantage due to the increased correctness when predicting the healthy condition, thereby improving utility for prescreening.

The improvement of the specificity is likely due to the use of the entire frequency information from Fig. 16. Neither the single integral over the entire frequency band nor a visual inspection of the multiple spectrum peaks can extract this additional information. On the other hand, the neural network classifier extracts additional useful features directly from the complex spectrum. These could be related to the relative positions and the relative peak values of several dominant spikes in Fig. 16.

The inclusion of the phase data by the neural network serves to increase its sensitivity compared to a network trained using only magnitude data. Further inclusion of wrist circumference increases both sensitivity and specificity by around 2% in most cases. This is likely due to wrist circumference being related to wrist fat content.

3.12. Discussion of Normalized Data

When the neural network is applied to the normalized dataset (which includes other risk factors from Section Chapter 2, a slight improvement is obtained. Normalizing the data provides a ~3% increase in overall accuracy and Youden's index. This boost is only observed in data sets that do not include the wrist circumference; datasets including the wrist circumference exhibit a loss of performance. It appears, therefore, that inclusion of additional risk factors will be complementary to the ability of the transmission data to reliably differentiate between healthy and diseases patients. Networks trained from normalized data perform better *without* the inclusion of wrist circumference data, likely because the normalization and wrist circumference data perform the same role of predicting wrist fat content and/or bone size. No normalization techniques other than the one presented in Eq. 8 were investigated.

3.13. Discussion of MLP Network Performance

Compared to more traditional machine learning techniques, specifically feature selection and principal component analysis, the MLP network proved more capable of successfully classifying the data despite its overlapping nature. Details of this comparison are provided in Appendix C on page 99. However, the MLP network did not provide any information that was useful for reducing the dimensionality of the classification problem without losing precision of the classification, beyond the lack of need for reflection data. Insignificance of reflection data is likely due to the dominant component of reflection coming from the antenna-skin boundary, rather than the tendon-bone boundary. To obtain useful information from the reflection

coefficient, some time-gating or time-aware signal processing would likely be needed. The current experimental setup does not have this capability.

3.14. Number Representations' Effect on Classification Results

For both the normalized and non-normalized datasets, data using the complex-number format for the scattering parameters provided increased sensitivity and specificity compared to data that used the magnitude-angle format. This is due to the stochastic gradient descent algorithm's preference for all of its feature data to be on the same scale. We avoided the traditional approach here of normalizing all of our data on a given interval due to a desire to keep the data set easily expandable. Because of this, magnitude-angle representation puts the magnitude and phase features (two features for a given frequency point) on dramatically different scales: magnitude on the scale of 0 to 0.12 and phase angle on the scale of -180 to 180 degrees (or, less egregiously, $-\pi/2$ to $\pi/2$). The complex number format, on the other hand, scales both the real and imaginary part (recorded as two separate real-valued features for each frequency point) roughly according to the magnitude, thereby achieving consistent scaling without the need for normalization.

3.15. Summary

The present chapter reported the application of a neural network classifier to the processing of previously collected data on very-low-power radiofrequency propagation through the wrist to detect osteoporotic/osteopenic conditions. Our approach categorizes the data obtained for two dichotomic groups. Group 1 included 27 osteoporotic/osteopenic subjects with low BMD (DXA T score below - 1) measured within one year. Group 2 included 40 healthy and mostly young subjects without major clinical risk factors such as a (family) history of bone fracture.

We process the complex radiofrequency spectrum from 30 kHz to 2 GHz. Instead of averaging data for both wrists, we are processing them independently along with the wrist circumference and then combine the results, which greatly increases the sensitivity. Measurements along with data processing require less than 1 min. Neural network classifiers can identify and use characteristics of the data not readily apparent to the human eye to increase the specificity of predictions. The neural network classifier used in this chapter is a multilayer perceptron with two fully connected layers implemented with the help of MATLAB Deep Learning Toolbox™. It was trained using the leave-one-out approach as described in

the Materials and Methods section. Additional machine learning experiments are located in Appendix C on page 99.

For the two dichotomic groups, the neural network classifier of the radiofrequency spectrum reports a sensitivity of 83% and a specificity of 94%. These results are obtained without the inclusion of any additional clinical risk factors. Given that other recent studies have shown a strong correlation between bone density measurements in the arms, hip, and spine [102], [103], the radio transmission data may be usable on their own as a predictor of bone density. Our approach has the potential for screening patients at risk for fragility fractures in the office, given the ease of implementation, small device size, and low costs associated with both the technique and the equipment.

Chapter 4. Miniaturized Dual Antiphase Patch Antennas for Microwave Imaging of Bone and Other Tissues

This chapter discusses the second primary contribution: design and construction of a miniaturized dual antiphase patch antenna for use in a dense microwave imaging array. The proposed antenna is a very low profile 2.4 GHz microwave imaging dual anti-phase patch antenna with linear polarization, coupled directly to the skin via a pressure fit. A distinct advantage of the 2.4 GHz band is its popularity in the commercial and medical spaces, and higher spatial resolution. On the other hand, there is also a disadvantage due to its higher propagation loss.

There have been a number of miniaturized RF devices and accessories developed for 2.4 GHz. In this chapter, a dual anti-phase patch antenna configuration [104], [6], tuned to 2.4 GHz, is fabricated on a PCB substrate. Both antenna feeds are combined through a 180-degree hybrid, which is also integrated into the PCB. As a result, only one signal port, at the output of the hybrid combiner, is required to establish the anti-phase property from the user interface perspective.



Fig. 19. Microwave imaging helmet with positions for multiple small antennas, fitted to a plastic head mock-up. Only two of the positions are populated with antennas in the figure.

A key benefit of a miniaturized antenna element is to establish an array of multiple elements. The smaller the element size, the more elements may be implemented, such as in Fig. 19. The design of the antenna array will be the subject of a future work, but Appendix D on page 108 discusses the design of the array controller board that accompanied these antennas. In the case of head imaging, antennas may be arrayed around the scalp of a patient [105], [106]. The increase in the number of elements may be beneficial from an image resolution point of view, at the expense of calibration and post-processing resources. Patch antennas inherently excite surface waves, which may also affect its adjacent radiating element to create signal leakage. Therefore, suppressing surface wave is critical to improve the signal to noise ratio of the detected image signals in this setup.

4.1. Antenna Design and Modelling

The antennas were first modelled numerically using Ansys Electronics Desktop 2021R2 HFSS (Ansys, Inc. Canonsburg, PA, USA). These models included the design of the resonator, the design of the 180-degree hybrid power splitter, and impedance-matching circuitry. A three-layer PCB was designed to incorporate patch antenna resonators and other discrete radio-frequency components. The goal is to create the smallest footprint as the building block of a microwave imaging antenna array. The specifications from the HFSS model were used to fabricate the antennas. Once the antennas were assembled, their performance was evaluated with on-phantom and in-vivo measurements.

The resonators in this chapter were adapted from the previous design for lower-frequency dual-antiphase patch antenna used for osteoporosis detection, discussed in the previous sections [6], [7]. A high-level dual-antiphase antenna concept was shown in Fig. 3b on page 19.

Whereas previous antennas, such as Fig. 20a, operated around 0.6-0.9 GHz [8], the antennas in this chapter were designed to operate at the 2.4 GHz ISM (Industrial, Scientific, and Medical) band [107]. To provide a proper capacitive loading to the antenna, a human body model is essential to the analysis. The human body model used throughout this chapter was the VHP-Female model, which has 249 distinct anatomical structures modelled [108]. A variety of resonator configurations were investigated then optimized by their size, electromagnetic penetration into the body, and the antenna's efficiency. The simulation setup is shown in Fig. 21.

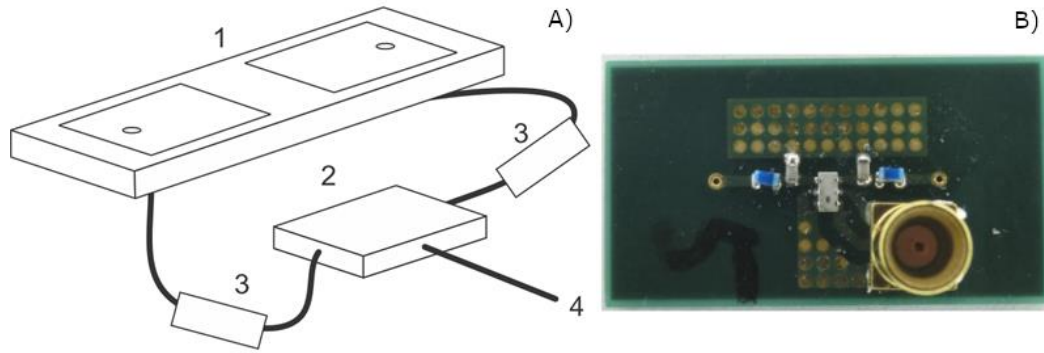


Fig. 20. (a) – Previous dual antiphase patch antenna (1) design with external matching networks (3) and balun (2) [7], (b) – present antenna with integrated matching networks and balun, and MMCX connector, both patches are on the far side.

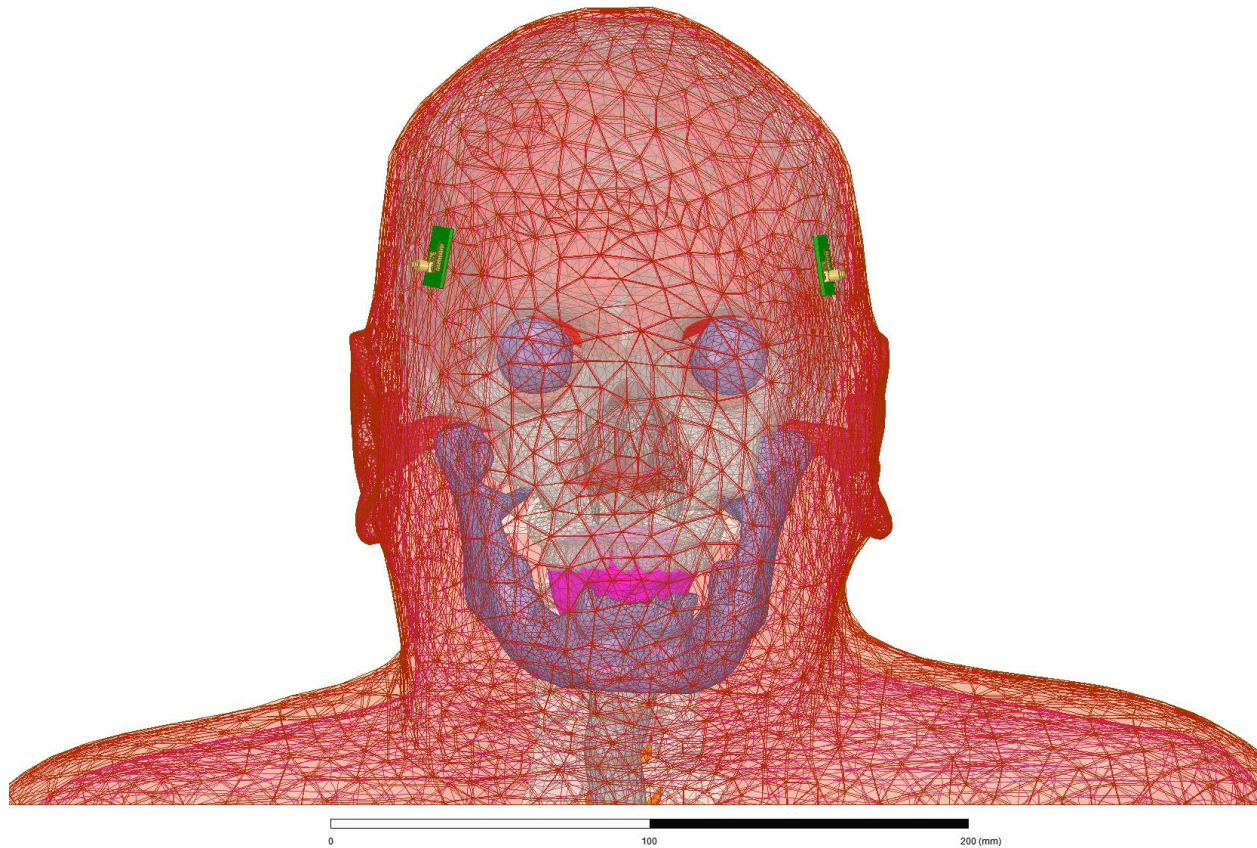


Fig. 21. Antennas placed on the temples the VHP-Female CAD model [108] for simulation in Ansys HFSS. The temples were chosen due to the natural lack of hair and relative distance across the head between the two positions.

The antennas presented in this chapter include a power splitter and matching circuitry in addition to the patch radiators, see Fig. 20b. Power splitting was accomplished by a LDM182G4505EC015 balun (Murata Manufacturing Co. Kyoto, JP). The two $50\ \Omega$ outputs

from the balun were each coupled to their respective resonator elements by an L-topology matching network.

4.2. Fabrication and Assembly

The dimensions from the HFSS simulation were transferred manually to Altium Designer (Altium Ltd. Chatswood, NSW, AU). The final 4-layer PCB layout was performed in Altium Designer with co-simulation in HFSS. The final dimensions of the antennas are shown in Fig. 22, which shows annotated renders from Ansys HFSS of the antenna as built. It features an MMCX connector for its feed. The inductors were 1.5 nH and the capacitor were 1.5 pF, all in 0402 packages.

The PCB was fabricated using three copper layers above, below and inside a low loss laminate, FR408HR, from Isola. A coaxial cable was soldered to the pads to measure the reflection coefficient of the resonator and determine the final values for the matching network components.

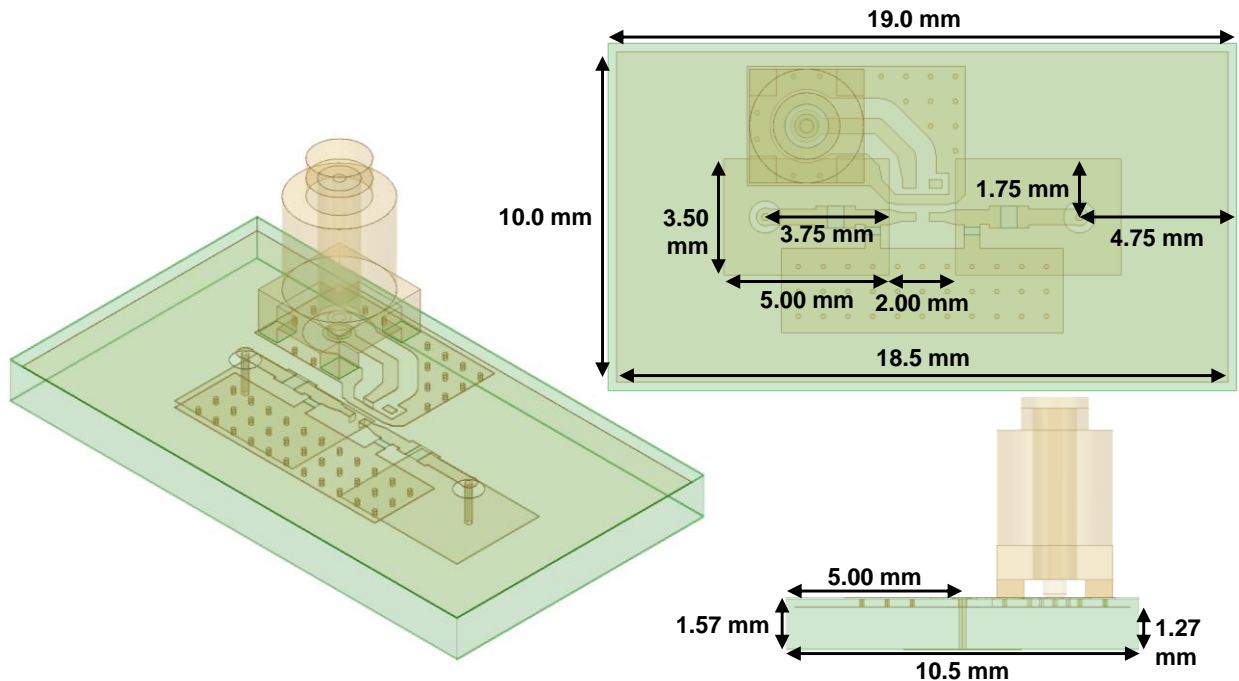


Fig. 22. Dimensions of the antenna as built. The board was finished to 62 mil (thou) thickness including all dielectric, copper, and mask layers. All other controlling dimensions were in millimeters.

4.3. Phantom Preparation

The phantom-measurements were performed on a phantom derived from subject 110411 from the Human Connectome Project [109]. The Computer Aided Design (CAD) model in Fig. 23b was generated from the data in [110]. The partial shells were printed from Polylactic Acid (PLA) and painted yellow. Holes were cut with the diameter of the hole equal to the antenna's diagonal. These holes were then covered by nitrile patches. Two phantoms were built: one with a single hole at the top of the head and one with four holes, paired left/right and front/back, shown in Fig. 23a. The phantom shell was filled with the 38% Triton X-100 to 62% water mixture with 5.2 g/L of salt adapted from [5], [111].

Reflection measurements were taken with multiple polarizations, moving the antennas randomly by 1-2 mm between measurements. Transmission measurements were only taken with the antennas co-polarized, measuring across the phantom either left to right or front to back. Again, the antennas' positions were perturbed by 1-2 mm between measurements.

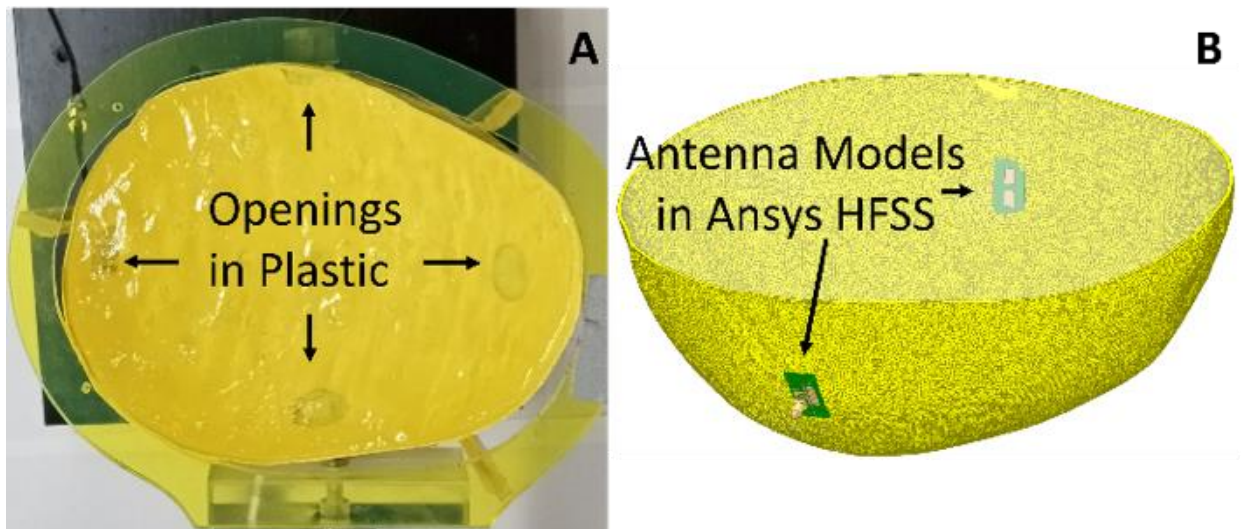


Fig. 23. (a) – Physical phantom with multiple antennas, (b) – Simulated phantom with multiple antennas

Data were collected using an HP8722ET vector network analyzer (VNA) with intermediate frequency resolution bandwidth (IFRBW) setting of 30 Hz, and output power of -5 dBm. Magnitude and phase data were collected for each measurement. The VNA was calibrated to a plane 3 inches before the antenna at an SMA connector. The 3 inches between the antenna and the plane were covered by a 50 Ω SMA-F to MMCX-F coaxial adapter cable.

4.4. Efficiency

An *in vivo* experiment with human heads from subjects was undertaken to assess the effectiveness of the proposed antiphase patch antenna assembly's radiation penetration into the human body. All human experiments were approved by the Institutional Review Board (WPI IRB 18-0310), and the Nelly model was used as the simulation subject. Phantom subject 110411 was also employed as a test vehicle in both simulation and measurement to further correlate the analysis (Fig. 23). Throughout this section, the antenna is loaded by a human body or conductive phantom because the present antennas exhibit negligible transmission in their design band when in air or free space.

Efficiency was tested using the human body CAD model in Ansys HFSS. The total radiation efficiency of the antenna was measured at 39.15% of incident power. This included power delivered to the body, to the receiver, and to the radiation boundary. Notably, 38.44% of incident power was delivered to and dissipated in the body.

4.5. Phantom Measurements vs. In Vivo Human Measurements

Both a human subject and a phantom subject were used in measurement for the comparison's sake. Due to the sensitivity of the antenna's capacitive loading against the human tissue, the measured S-parameters may vary from one capture to the next. Three sampled measurements were averaged to demonstrate its statistical reflection and transmission. The comparison between the human head and the phantom subject measurement indicates a close agreement, as shown in Fig. 24, especially in the targeted band of 2.3-2.5 GHz. The VNA configuration and calibration used on the human subject was identical to the configuration used for the phantom (see Section 4.3).

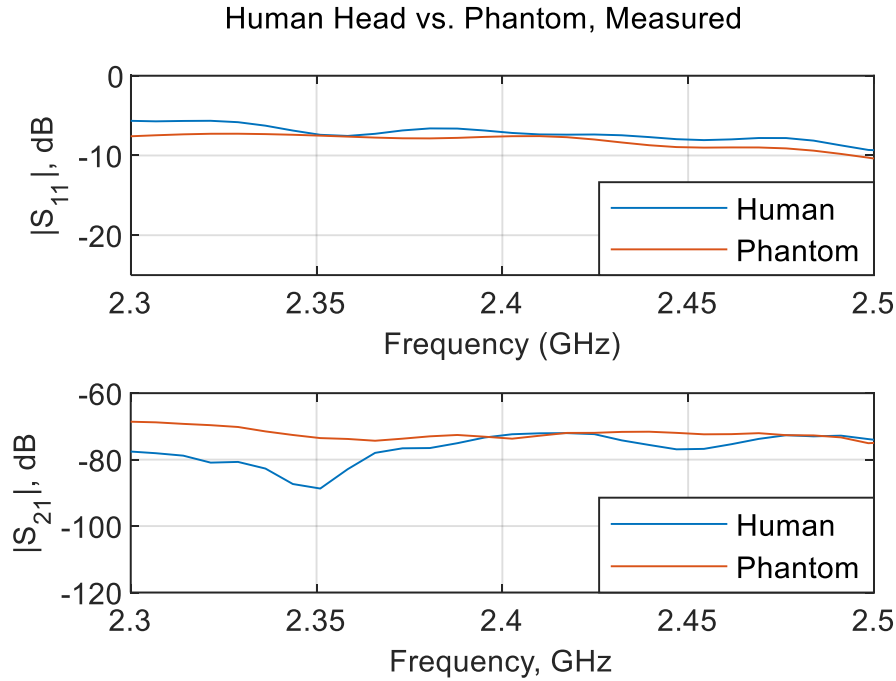


Fig. 24. Comparison between reflection and transmission measurements ($|S_{11}|$ and $|S_{21}|$) on the phantom and on a human head, averaged across 2 measurements for one subject.

4.6. Phantom Measurements vs. Simulations

Fig. 25 illustrates S_{11} and S_{21} on phantom subject 110411 in both measurements and simulations. The measured line for the phantom was generated by averaging two sets of measurements.

Reflection coefficients S_{11} from both simulation and measurement indicate low resonance characteristic. It is common for miniaturized antennas. In terms of S_{21} , there is decent agreement in that the delta between the simulation and the measurement is within 10 dB across the band of interest (between 2.3 and 2.5 GHz).

The connectors, the cable and the balun all have 50 Ω characteristic impedances. Even the microstrip line on the PCB from the connector to the balun, less than 5 mm in length and less than 1/20th of a wavelength, has a 50 Ω characteristic impedance. Therefore, it is expected that calibration at the MMCX connector (instead of 3 inches earlier at the SMA connector) would yield only a marginal improvement in agreement between the measured and simulated results.

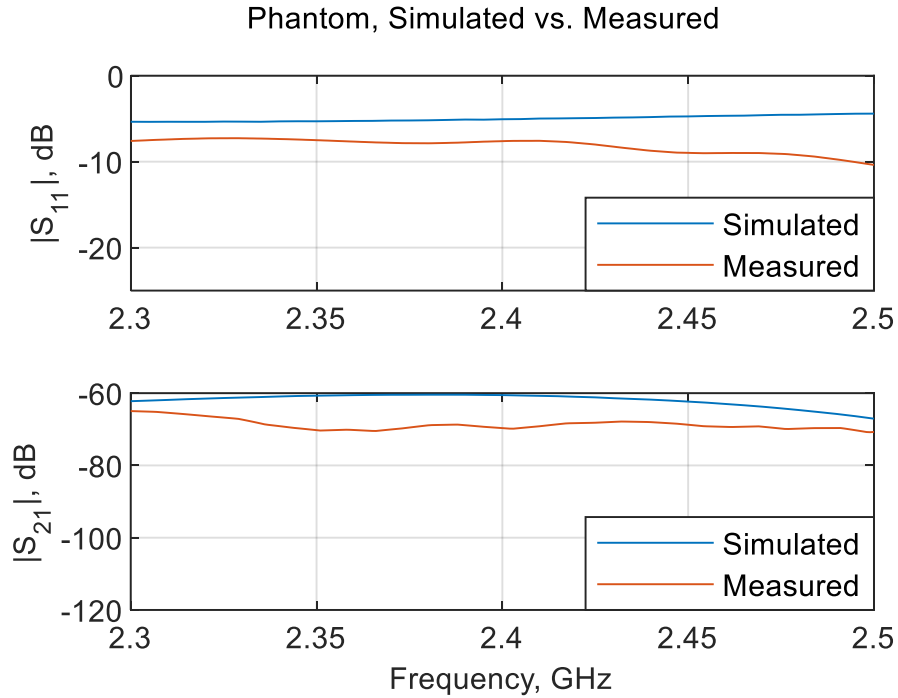


Fig. 25. Comparison between simulation and the average of two measurements of S-parameters ($|S_{11}|$ and $|S_{21}|$) for the phantom.

4.7. In Vivo Human Head Measurements vs. Simulations

Both simulations and measurements were conducted on the human head to validate the experiment. The VHP-Female model [108] was used as the simulation subject, physical validation was performed on a human subject (Fig. 26). Fig. 27 shows the experimental configuration of the antenna placed on the side of the human subject's head. That figure does not include the acrylic blocks used to hold the antenna to the subject's head at a constant pressure. The VNA configuration and calibration used on the human subject was identical to the configuration used for the phantom (see Section 4.3).

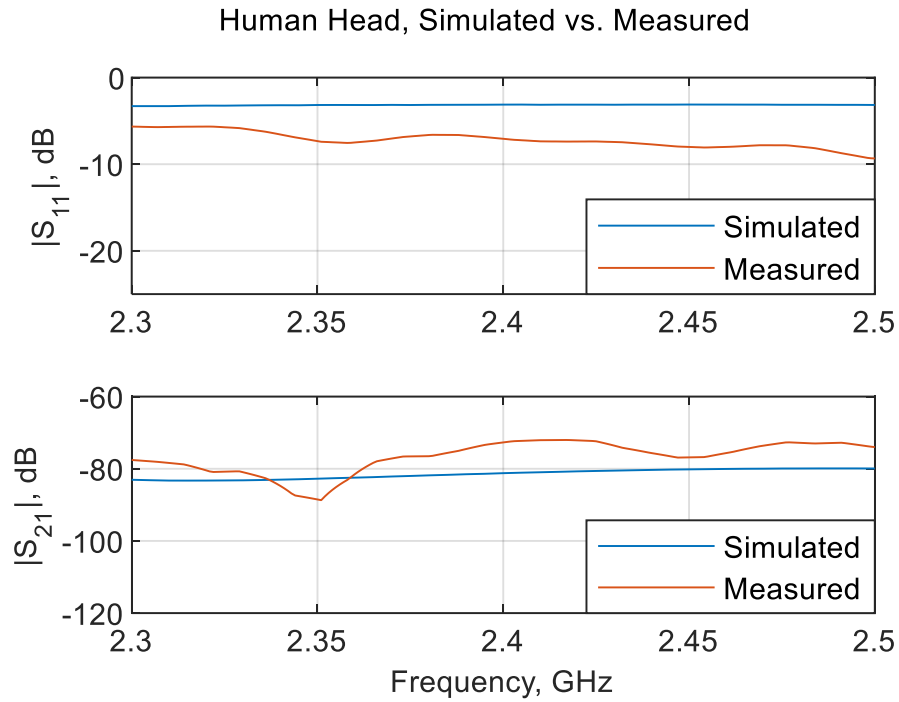


Fig. 26. Comparison between simulated and measured results for the VHP-Female model [108] and the average of two measurements on one in-vivo subject.

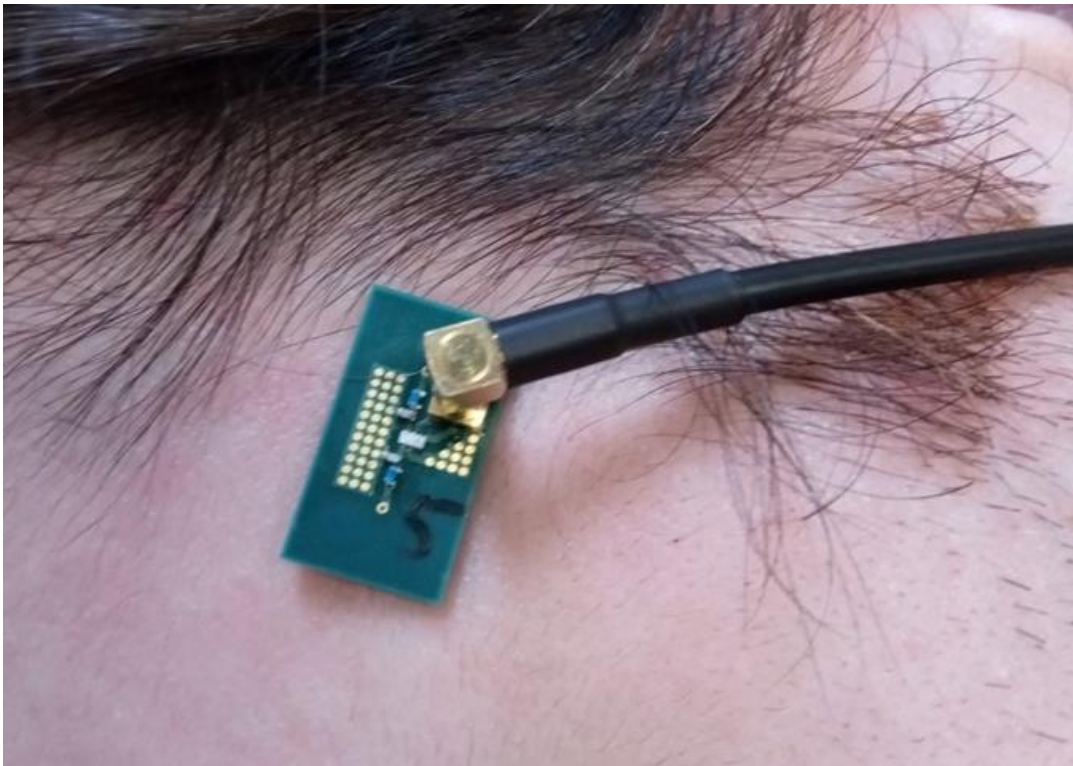


Fig. 27. Antenna positioned on the subject's temple to measure reflection. An identical antenna was placed on the opposite temple to measure transmission.

4.8. Simulated Electric Field Patterns Around Phantom and Human Head

Fig. 28 shows a representative comparison of the distribution of the E-field between the phantom (A, C) and the head (B, D) in the vicinity of the antenna. All simulations were performed in Ansys ED 2021R2. One distinct feature of the E-field distribution is the clear presence of surface waves. To take advantage of the received signals scattered from the targeted tissue, it is critically important to characterize the contribution of the surface waves and to assure that it is not the S_{21} 's dominant path.

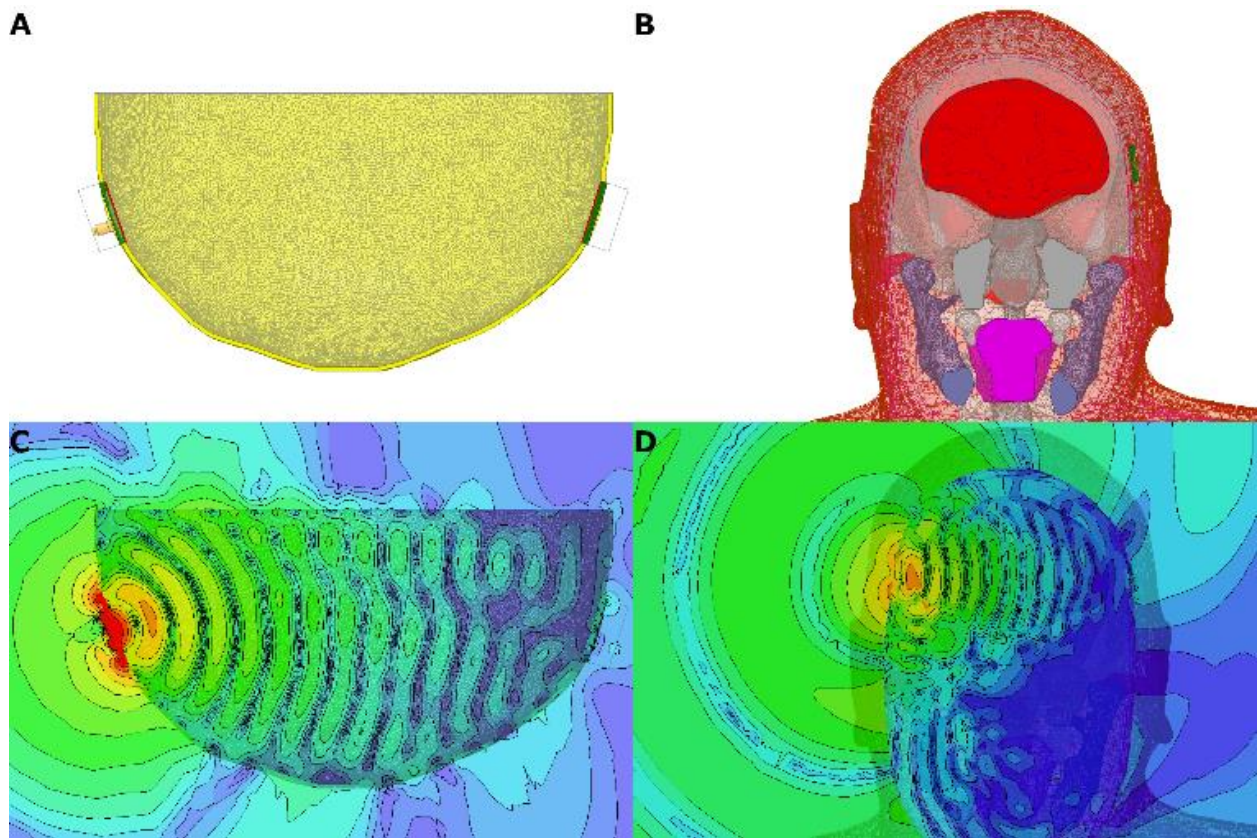


Fig. 28. (a) – Simulation setup for the phantom, coronal plane. (b) – Simulation setup for VHP-Female [108], coronal plane. (c) – Average electric field strength, $|E|$, in the coronal plane of the phantom. (d) – Average electric field strength, $|E|$, in the coronal plane of the VHP-Female model [108].

4.9. Discussion of Results

This chapter has produced a miniaturized, unitized dual antiphase patch antenna that is smaller than the existing on-body antennas known to the authors, some of which are listed in Table 3 on the next page. The present design uses an oversized ground plane, giving it the

potential for further miniaturization without significant loss of performance. Using these antennas, a theoretical microwave imaging device can achieve higher spatial resolution compared to devices using larger antennas due to the difference in density of the arrays.

Compared to contemporary on-body antennas operating at 2.4 GHz, the antenna presented in this chapter is smaller and has more potential for further size reduction without loss of performance, as shown in Fig. 29 on the next page. This may be accomplished by decreasing the annular width of the ground plane around the resonators and replacing the MMCX jack with an integral coaxial cable or other small-footprint coaxial interface. The bowtie, by comparison, uses all the available space on its PCB and the other antennas from Table 3 are significantly larger.

Table 3: Contemporary Microwave Imaging Antenna Sizes and Bands

Antenna	Length	Width	Band
Flexible Single Patch [112]	56.7 mm	49.2 mm	2.3-2.5 GHz
UWB Loaded Box [69]	105 mm	45 mm	0.75-2.5 GHz
On Body Vivaldi [113]	77 mm	60 mm	2.0-10 GHz
On Body Bowtie [114]	18 mm	18 mm	0.75-4.0 GHz
Dual Antiphase Patch	18.5 mm	10 mm	2.4-2.5 GHz

4.10. Limitations

One problem with the present antenna design is the appearance of surface waves clearly seen in Fig. 28 on the previous page, especially for the realistic human head model. For small antennas, those waves are likely unavoidable when no extra means are used to suppress them. Such means may include an enclosing antenna cavity, using perpendicular polarizations for nearby antenna radiators, using temporal waveforms (e.g., radio frequency pulses), and using different absorbing materials. Those means are presently under investigation.

Mismatch between the measured and simulated results can be attributed to multiple factors. For example, the VHP-Female model [108] used in the simulations was generated based on a middle-aged, obese female. The measurements, on the other hand, were performed on a young-adult, healthy-weight male. In the case of the measurements on the phantom, some small air bubbles could be present in the gel solution which could slightly affect its properties.

Additionally, the real phantom was painted inside and out with yellow spray paint, which was not accounted for in the simulation model. That said, it is not expected that accounting for these differences in the simulated model may not improve the results, because the difference between measured and simulated data for both the phantom and the human is of almost the same magnitude. This means that the majority of the observed error is unlikely to be derived from the fidelity of the model in either case and improvements to the model, for example a male CAD model, likely would not yield more than a marginal improvement in agreement between simulated and measured data.

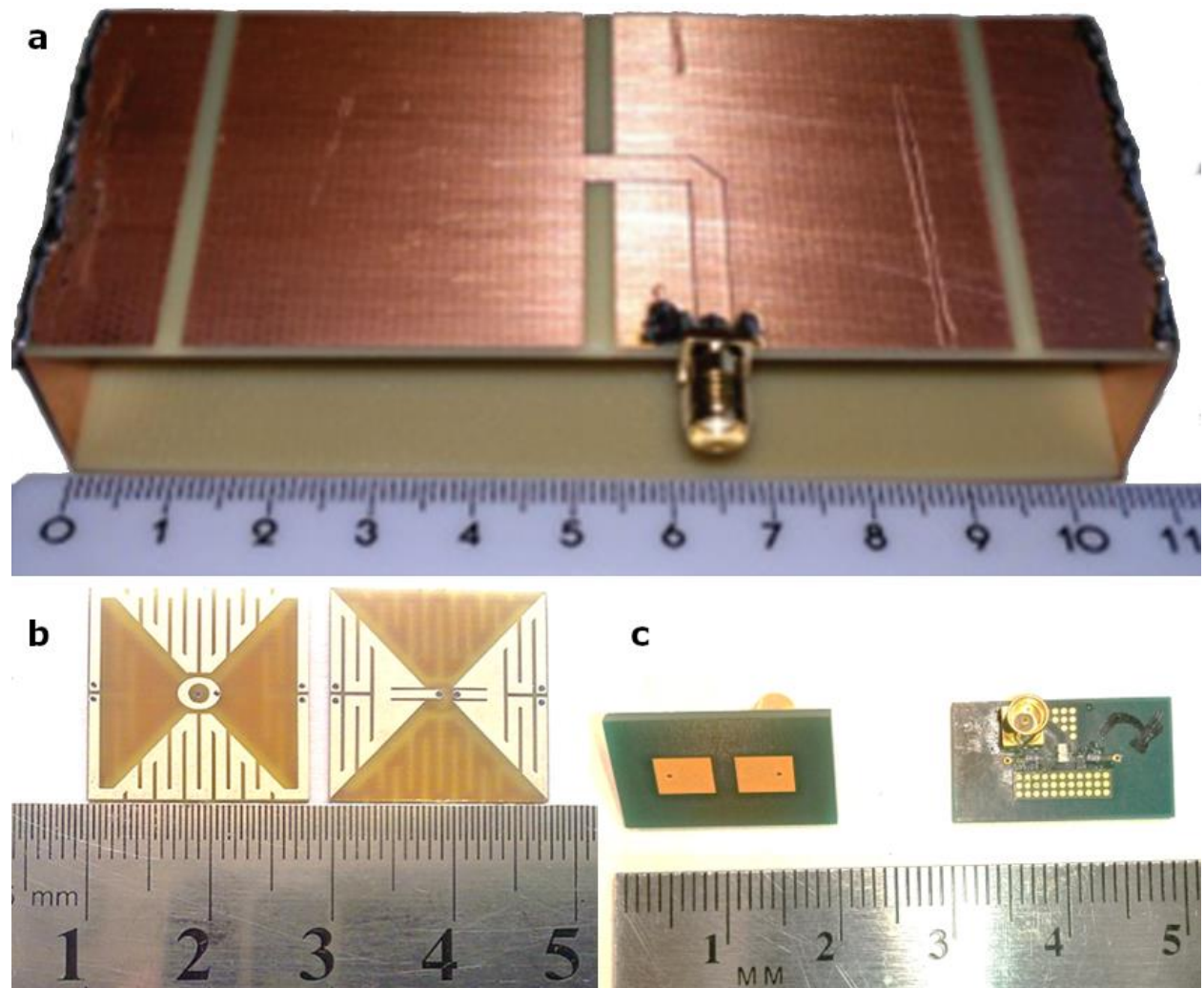


Fig. 29. Size comparison between (a) – ultra-wideband loaded box antenna [69], (b) – on body bowtie antenna [114], and (c) – the miniature dual antiphase patch antenna presented in this chapter. The miniature dual antiphase patch antenna has potential for size reduction via removal of excess ground plane and the installation of a more compact connector assembly.

The two biggest sources of loss were power reflected out the input (46.11% of incident) and power dissipated in the balun (11.57%). The high reflected power is likely due to the mismatch remaining in the matching networks. The matching accuracy is constrained by the precision of the matching capacitor and inductor, as well as their error with respect to their nominal values. The inductor in particular is on the small end of physically-realizable wire-wound inductor values, and is the cause of some amount of reflection.

4.11. Summary

A small low-profile on-body antiphase patch antenna operating from 2.3 to 2.5 GHz was designed, constructed, and evaluated numerically and experimentally using both phantom and human subjects. The electric field pattern, transmission, and reflection were measured experimentally and showed approximate agreement, though agreement between the simulations and measurements could be improved with more physically accurate models. By properly damping the surface waves, the detected signal's SNR may be improved further. The experimental results demonstrate that this antenna configuration may be a viable candidate for MI applications targeting relatively narrowband dense antenna arrays.

My Publications and Presentations

Publications

J. W. Adams, Z. Zhang, G. M. Noetscher, A. Nazarian and S. N. Makarov, "Application of a Neural Network Classifier to Radiofrequency-Based Osteopenia/Osteoporosis Screening," in *IEEE Journal of Translational Engineering in Health and Medicine*, vol. 9, pp. 1-7, 2021, Art no. 4900907, doi: 10.1109/JTEHM.2021.3108575.

J. Adams, Z. Zhang, G. M. Noetscher, A. Nazarian and S. N. Makarov, "Application of a Neural Network Classifier to Radiofrequency-Based Osteopenia/Osteoporosis Screening," *2021 43rd Annual International Conference of the IEEE Engineering in Medicine & Biology Society (EMBC)*, 2021, pp. 15-18, doi: 10.1109/EMBC46164.2021.9630944.

P. J. Serano, J. W. Adams, and A. Nazarian, "Modeling and Experimental Results for Microwave Imaging of a Hip with Emphasis on the Femoral Neck," in *Brain and Human Body Modelling 2021: Selected Papers Presented at 2021 BHBM Conference*, S. Makarov, G. Noetscher, A. Nummenmaa, Springer Nature, 2022, ch. 10, pp. 125-138. ISBN 978-3-031-15450-8.

J. W. Adams, L. Chen, P. Serano, A. Nazarian, R. Ludwig, S. Makarov, "Miniaturized Dual Antiphase Patch Antenna Radiating into the Human Body at 2.4 GHz," *IEEE J. of EM, RF, and MW in Medicine and Biology*, Under Review.

Presentations

J. Adams, Z. Zhang, G. M. Noetscher, A. Nazarian and S. N. Makarov, "Application of Neural Networks to Radiofrequency Osteoporosis Screening," *2021 43rd Annual International Conference of the IEEE Engineering in Medicine & Biology Society (EMBC)*.

J. Adams, S. N. Makarov, G. M. Noetscher, S. Arum, R. Rabiner, A. Nazarian, and Z. Zhang, "Application of Neural Networks to Radiofrequency Osteoporosis Screening," *Brain and Human Body Modelling 2021*. Available: <https://education.martinos.org/brain-and-human-body-modeling-conference/>

J. W. Adams, L. Chen, and P. Serano, "Miniaturized Dual Antiphase Antenna at 2.4 GHz for Microwave Imaging" at *Brain and Human Body Modelling Conference 2022*. Available: <https://tmslab.martinos.org/conferences/brain-and-human-body-modeling-conference-2022/>

G. Noetscher, W. Wartman, D. Pham, J. Adams, S. Makarov, "Verification of the VHP-Female V.5.0 Full Body CAD Human Model," *2018 40th Annual International Conference of the IEEE Engineering in Medicine & Biology Society (EMBC)*.

References

- [1] J. H. Jacobi, L. E. Larsen and C. T. Hast, "Water-Immersed Microwave Antennas and Their Application to Microwave Interrogation of Biological Targets," *IEEE Transactions on Microwave Theory and Techniques*, vol. 27, no. 1, pp. 70-78, 1979.
- [2] L. E. Larsen and J. H. Jacobi, "The Use of Orthogonal Polarizations in Microwave Imagery of Isolated Canine Kidney," *IEEE Transactions on Nuclear Science*, vol. 27, no. 3, pp. 1183-1191, 1980.
- [3] A. H. Barrett and P. C. Myers, "Subcutaneous Temperatures: A Method of Noninvasive Sensing," *Science*, vol. 190, no. 4215, pp. 669-671, 1975.
- [4] P. M. Meany, D. Goodwin, A. H. Golnabi, T. Zhou, M. Pallone, S. D. Geimer, G. Burke and K. D. Paulsen, "Clinical Microwave Tomographic Imaging of the Calcaneus: A First-in-Human Case Study of Two Subjects," *IEEE Transactions on Biomedical Engineering*, vol. 59, no. 12, pp. 3304-3313, 2012.
- [5] D. O. Rodriguez-Duarte, J. A. Tobon Vasquez, R. Scapatucci, L. Crovvo and F. Vipiana, "Brick-Shaped Antenna Module for Microwave Brain Imaging Systems," *IEEE Antennas and Wireless Propagation Letters*, vol. 19, no. 12, pp. 2057-2061, 2020.
- [6] S. N. Makarov, G. M. Noetscher, S. Arum, R. Rabiner and A. Nazarian, "Concept of a Radiofrequency Device for Osteopenia/Osteoporosis Screening," *Scientific Reports*, vol. 10, p. 3540, 2020.
- [7] S. N. Makarov, G. M. Noetscher, V. Makarov and A. Nazarian, "Dual antiphase antenna for better signal transmission into human body or signal reception from human body". US Patent 11101554, 3 July 2019.
- [8] S. N. Makarov, G. M. Noetscher, V. S. Makarov and A. Nazarian, "Novel Microwave Antenna Array and Testbed for Osteoporosis Detection". United States of America Patent 10657338, 16 January 2018.

- [9] CDC, "About Stroke," U.S. Department of Health & Human Services, 4 May 2022. [Online]. Available: <https://www.cdc.gov/stroke/about.htm>. [Accessed 6 June 2022].
- [10] D. O. Rodriguez-Duarte, J. A. Tobon Vasquez, S. De Luque Arias, R. Scapaticci, L. Crocco and F. Vipiana, "A Portable Microwave Scanner for Brain Stroke Monitoring: Design, Implementation and Experimental Validation," in *2022 16th European Conference on Antennas and Propagation (EuCAP)*, Madrid, 2022.
- [11] A. Ciccone, M. Celani, R. Chiaramonte, C. Rossi and E. Righetti, "Continuous versus intermittent physiological monitoring for acute stroke," *Cochrane Database of Systematic Reviews*, no. 5, 2013.
- [12] G. Tsivfoulis and A. V. Alexandrov, "Ultrasound-enhanced thrombolysis in acute ischemic stroke: Potential, failures, and safety," *Neurotherapeutics*, vol. 4, pp. 420-427, 2007.
- [13] Medfield Diagnostics AB, "Products: Strokefinder," [Online]. Available: <https://www.medfielddiagnostics.com/products/>. [Accessed 16 June 2022].
- [14] EMTensor, Inc., "Homepage," [Online]. Available: <https://www.emtensor.com/>. [Accessed 16 June 2022].
- [15] EMVision, "Products," [Online]. Available: <https://emvision.com.au/products/>. [Accessed 16 June 2022].
- [16] A. Trakic, A. Brankovic, A. Zamani, N. Nguyen-Trong, B. Mohammed, A. Stancombe, L. Guo, K. Bialkowski and A. Abbosh, "Expedited Stroke Imaging With Electromagnetic Polar Sensitivity Encoding," *IEEE Transactions on Antennas and Propagation*, vol. 68, no. 12, pp. 8072-8081, 2020.
- [17] A. S. M. Alqadami, A. Zamani, A. Trakic and A. Abbosh, "Flexible Electromagnetic Cap for Three-Dimensional Electromagnetic Head Imaging," *IEEE Transactions on Biomedical Engineering*, vol. 68, no. 9, pp. 2880-2891, 2021.

- [18] C. Hui and K. M. Luk, "An On-Body Matched Differentially-Fed Magneto-Electric Dipole Antenna for Head Imaging Systems," *IEEE Transactions on Antennas and Propagation*, 2022.
- [19] Cleveland Clinic, "Osteoporosis," 27 April 2020. [Online]. Available: <https://my.clevelandclinic.org/health/diseases/4443-osteoporosis>. [Accessed 16 June 2022].
- [20] S. Lee and D. Gallagher, "Assessment methods in human body composition," *Current Opinion in Clinical Nutrition and Metabolic Care*, vol. 11, no. 5, pp. 566-572, 2008.
- [21] E. Lochmuller, N. Krefting, D. Burklein and F. Eckstein, "Effect of Fixation, Soft-Tissues, and Scan Projection on Bone Mineral Measurements with Dual Energy X-ray Absorptiometry (DXA)," *Calcified Tissue International*, vol. 68, no. 3, pp. 140-145, 2001.
- [22] O. Svendsen, C. Hassager, V. Skodt and C. Christiansen, "Impact of soft tissue on in vivo accuracy of bone mineral measurements in the spine, hip, and forearm: A human cadaver study," *Journal of Bone and Mineral Research*, vol. 10, no. 6, pp. 868-873, 2009.
- [23] E. Lochmuller, P. Miller, D. Burklein, U. Wehr, W. Rambeck and F. Eckstein, "In Situ Femoral Dual-Energy X-ray Absorptiometry Related to Ash Weight, Bone Size and Density, and its Relationship with Mechanical Failure Loads of the Proximal Femur," *Osteoporosis International*, vol. 11, no. 4, pp. 361-367, 2000.
- [24] A. Prentice, T. Parsons and T. Cole, "Uncritical use of bone mineral density in absorptiometry may lead to size-related artifacts in the identification of bone mineral determinants," *The American Journal of Clinical Nutrition*, vol. 60, no. 6, pp. 837-842, 1994.
- [25] H. K. Genant, K. Engelke, T. Fuerst, C.-C. Glüer, S. Grampp, S. T. Harris, M. Jergas, T. Lang, Y. Lu, S. Majumdar, A. Mathur and M. Takada, "Noninvasive assessment of bone mineral and structure: State of the art," *Journal of Bone and Mineral Research*, vol. 11, no. 6, pp. 707-730, 1996.

- [26] S. C. Schuit, M. van der Klift, A. E. A. M. Weel, C. E. D. H. de Laet, H. Burger, E. Seeman, A. Hofman, A. G. Uitterlinden, J. P. T. M. van Leeuwen and H. A. P. Pols, "Fracture incidence and association with bone mineral density in elderly men and women: the Rotterdam Study," *Bone*, vol. 34, no. 1, pp. 195-202, 2004.
- [27] S. R. Cummings, D. B. Karpf, F. Harris, H. K. Genant, K. Ensrud, A. Z. LaCroix and D. M. Black, "Improvement in spine bone density and reduction in risk of vertebral fractures during treatment with antiresorptive drugs," *The American Journal of Medicine*, vol. 112, no. 4, pp. 281-289, 2002.
- [28] R. Heaney, "Is the paradigm shifting?," *Bone*, vol. 33, no. 4, pp. 457-465, 2003.
- [29] D. C. Bauer, D. M. Black, P. Garnero, M. Hochberg, S. Ott, J. Orloff, D. E. Thompson, S. K. Ewing and P. D. Delmas, "Change in Bone Turnover and Hip, Non-Spine, and Vertebral Fracture in Alendronate-Treated Women: The Fracture Intervention Trial," *Journal of Bone and Mineral Research*, vol. 19, no. 8, pp. 1250-1258, 2004.
- [30] B. Riggs and L. Melton, "Bone Turnover Matters: The Raloxifene Treatment Paradox of Dramatic Decreases in Vertebral Fractures Without Commensurate Increases in Bone Density," *Journal of Bone and Mineral Research*, vol. 17, no. 1, pp. 11-14, 2002.
- [31] J. Karjalainen, O. Riekkinen and H. Kroger, "Pulse-echo ultrasound method for detection of post-menopausal women with osteoporotic BMD," *Osteoporosis International*, vol. 29, no. 5, pp. 1193-1199, 2018.
- [32] T. Zhou, P. M. Meany, M. J. Pallone, S. Geimer and K. D. Paulsen, "Microwave tomographic imaging for osteoporosis screening: a pilot clinical study," in *2010 Annual International Conference of the IEEE Engineering in Medicine and Biology*, Buenos Aires, 2010.
- [33] P. M. Meany, D. Goodwin, A. Golnabi, M. Pallone, S. Geimer and K. D. Paulsen, "3D Microwave bone imaging," in *2012 6th European Conference on Antennas and Propagation (EUCAP)*, Prague, 2012.

- [34] A. H. Golnabi, P. M. Meany, S. Geimer, T. Zhou and K. D. Paulsen, "Microwave tomography for bone imaging," in *2011 IEEE International Symposium on Biomedical Imaging: From Nano to Macro*, Chicago, 2011.
- [35] P. Meany, T. Zhou, T. Goodwin, A. Golnabi, E. Attardo and K. D. Paulsen, "Bone Dielectric Property Variation as a Function of Mineralization at Microwave Frequencies," *International Journal of Biomedical Imaging*, vol. 2012, pp. 1-9, 2012.
- [36] R. Chandra, H. Zhou, I. Balasingham and R. M. Narayanan, "On the Opportunities and Challenges in Microwave Medical Sensing and Imaging," *IEEE Transactions on Biomedical Engineering*, vol. 62, no. 7, pp. 1667-1682, 2015.
- [37] V. Zhurbenko, T. Rubek, V. Krozer and P. Meincke, "Design and realisation of a microwave three-dimensional imaging system with application to breast-cancer detection," *IET Microwaves, Antennas & Propagation*, vol. 4, no. 12, p. 2200, 2010.
- [38] C. Gabriel, *Compilation of the Dielectric Properties of Body Tissues at RF and Microwave Frequencies*, Brooks Air Force Base: Air Force Materiel Command, 1996.
- [39] P. A. Hasgall, F. Di Gennaro, C. Baumgartner, E. Neufeld, B. LLoyd, M. C. Gosselin, D. Payne, A. Klingenbock and N. Kuster, "IT'IS Database for thermal and electromagnetic parameters of biological tissues," [Online]. Available: itis.swiss/database. [Accessed 15 5 2018].
- [40] Mayo Clinic, "Breast Cancer - Symptoms and Causes - Mayo Clinic," 27 April 2022. [Online]. Available: <https://www.mayoclinic.org/diseases-conditions/breast-cancer/symptoms-causes/syc-20352470>. [Accessed 23 June 2022].
- [41] U. Kahn, N. Al-Moayed, N. Nguyen, M. Obol, K. Korolev, M. Afsar and S. Naber, "High Frequency Dielectric Characteristics of Tumorous and Nontumorous Breast Tissues," in *2007 IEEE/MTT-S International Microwave Symposium*, 2007.
- [42] M. Stuchly and S. Stuchly, "Dielectric Properties of Biological Substances – Tabulated," *Journal of Microwave Power*, vol. 15, no. 1, pp. 19-26, 1980.

- [43] K. Foster and H. Schwan, "Dielectric Properties of Tissues and Biological Materials: A Critical Review," *CRC Critical Reviews in Biomed. Engineering*, vol. 17, no. 1, pp. 25-104, 1989.
- [44] L. Sha, E. Ward and B. Stroy, "A Review of Dielectric Properties of Normal and Malignant Breast Tissue," in *Proc. of the IEEE SoutheastCon*, 2002.
- [45] W. T. Joines, Y. Zhang, C. Li and R. L. Jirtle, "The Measured Electrical Properties of Normal and Malignant Human Tissues From 50 to 900 MHz," *Med. Physics*, vol. 21, no. 4, p. 547–550, 1994.
- [46] M. Lazebnik, L. McCartney, D. Popovic, C. B. Watkins, M. J. Lindstrom, J. Harter, S. Sewall, A. Magliocco, J. H. Bookse, M. Okoniewski and S. C. Hagness, "A Large-Scale Study of the Ultrawideband Microwave Dielectric Properties of Normal Breast Tissue Obtained From Reduction Surgeries," *Physics in Med. and Biol.*, vol. 52, no. 10, pp. 2637-2656, 2007.
- [47] M. Lazebnik, D. Popovic, L. McCartney, C. B. Watkins, M. J. Lindstrom, J. Harter, S. Sewall, T. Ogilvie, A. Magliocco, T. M. Breslin, W. Temple, D. Mew, J. H. Bookse, M. Okoniewski and S. C. Hagness, "A Large-Scale Study of The Ultrawideband Microwave Dielectric Properties of Normal, Benign and Malignant Breast Tissues Obtained From Cancer Surgeries," *Physics in Med. and Biol.*, vol. 52, no. 20, p. 6093–6115, 2007.
- [48] S. Poplack, K. Paulsen, A. Hartov, P. Meaney, B. Pogue, T. Tosteson, M. Grove, S. Soho and W. Wells, "Electromagnetic Breast Imaging: Average Tissue Property Values in Women With Negative Clinical Findings," *Radiology*, vol. 231, no. 2, pp. 571-580, 2004.
- [49] P. Meaney, M. Fanning, T. Raynolds, C. Fox, Q. Fang, C. Kogel, S. Poplack and K. Paulsen, "Initial Clinical Experience with Microwave Breast Imaging in Women with Normal Mammography," *Academic Radiology*, vol. 14, no. 2, pp. 207-218, 2007.

- [50] W. Hurt, J. Ziriak and P. Mason, "Variability in EMF Permittivity Values: Implications for SAR Calculations," *IEEE Trans. on Biomed. Engineering*, vol. 47, no. 3, pp. 396-401, 2000.
- [51] S. Kwon and S. Lee, "Recent Advances in Microwave Imaging for Breast Cancer Detection," *Int J Biomed Imaging*, vol. 2016, 2016.
- [52] A. S. Liu, "Screening for Breast Cancer: U.S. Preventive Services Task Force Recommendation Statement," *Ann Intern Med*, vol. 164, no. 4, pp. 279-296, 2016.
- [53] N. K. Nikolova, "Microwave Imaging for Breast Cancer," *IEEE Microwave Magazine*, vol. 12, no. 7, pp. 78-94, 2011.
- [54] S. C. Hagness, A. Taflove and J. E. Bridges, "Three-dimensional FDTD analysis of a pulsed microwave confocal system for breast cancer detection: design of an antenna-array element," *IEEE Transactions on Antennas and Propagation*, vol. 47, no. 5, pp. 783-791, 1999.
- [55] J. Shea, P. Kosmas, S. C. Hagness and B. D. Van Veen, "Three-dimensional microwave imaging of realistic numerical breast phantoms via a multiple-frequency inverse scattering technique," *Medical Physics*, vol. 37, no. 8, pp. 4210-4226, 2010.
- [56] M. A. Al-Jourayly, S. M. Aguilar, N. Behdad and S. C. Hagness, "Dual-Band Miniaturized Patch Antennas for Microwave Breast Imaging," *IEEE Antennas and Wireless Propagation Letters*, vol. 9, pp. 268-271, 2010.
- [57] P. M. Meaney, K. D. Paulsen and T. P. Ryan, "Two-dimensional hybrid element image reconstruction for TM illumination," *IEEE Transactions on Antennas and Propagation*, vol. 43, no. 3, pp. 239-247, 1995.
- [58] P. M. Meaney, K. D. Paulsen, A. Hartov and R. K. Crane, "An Active Microwave Imaging System for Reconstruction of 2-D Electrical Property Distributions," *IEEE Transactions on Biomedical Engineering*, vol. 42, no. 10, pp. 1017-1026, 1995.

- [59] P. M. Meaney, K. D. Paulsen, A. Hartov and R. K. Crane, "Microwave imaging for tissue assessment: initial evaluation in multitarget tissue-equivalent phantoms," *IEEE Transactions on Biomedical Engineering*, vol. 43, no. 9, pp. 878-890, 1996.
- [60] P. M. Meaney, K. D. Paulsen and J. T. Chang, "Near-field microwave imaging of biologically-based materials using a monopole transceiver system," *IEEE Transactions on Microwave Theory and Techniques*, vol. 46, no. 1, pp. 31-45, 1998.
- [61] Q. Xue, S. W. Liao and J. H. Xu, "A Differentially-Driven Dual-Polarized Magneto-Electric Dipole Antenna," *IEEE Transactions on Antennas and Propagation*, vol. 61, no. 1, pp. 425-430, 2013.
- [62] P. M. Meaney, F. Shubitidze, M. W. Fanning, N. R. Epstein and K. D. Paulsen, "Surface wave multipath signals in near-field microwave imaging," *Int. J. Antennas Propag.*, vol. 2012, 2012.
- [63] D. O. Rodriguez-Duarte, J. A. Tobon Vasquez, A. De Luque Arias, R. Scapatucci, L. Crocco and F. Vipiana, "A Portable Microwave Scanner for Brain Stroke Monitoring: Design, Implementation and Experimental Validation," in 2022, 2022 16th European Conference on Antennas and Propagation (EuCAP).
- [64] D. O. Rodriguez-Duarte, J. A. Tobon Vasquez, R. Scapatucci, L. Crocco and F. Vipiana, "Assessing a Microwave Imaging System for Brain Stroke Monitoring via High Fidelity Numerical Modelling," in *IEEE Journal of Electromagnetics, RF and Microwaves in Medicine and Biology*, 2021.
- [65] P. M. Meaney, M. W. Fanning, D. Li, S. P. Poplack and K. D. Paulsen, "A clinical prototype for active microwave imaging of the breast," *IEEE Transactions on Microwave Theory and Techniques*, vol. 48, no. 11, pp. 1841-1853, 2000.
- [66] C. Yu, M. Yuan, J. Stang, E. Bresslour, R. T. George, G. A. Ybarra, W. T. Joines and Q. H. Liu, "Active Microwave Imaging II: 3-D System Prototype and Image Reconstruction From Experimental Data," *IEEE Transactions on Microwave Theory and Techniques*, vol. 56, no. 4, pp. 991-1000, 2008.

- [67] T. Rubaek, O. S. Kim and P. Meincke, "Computational Validation of a 3-D Microwave Imaging System for Breast-Cancer Screening," *IEEE Transactions on Antennas and Propagation*, vol. 57, no. 7, pp. 2105-2115, 2009.
- [68] M. Bassi, M. Caruso, M. S. Khan, A. Bevilacqua, A. Capobianco and A. Neviani, "An Integrated Microwave Imaging Radar With Planar Antennas for Breast Cancer Detection," *IEEE Transactions on Microwave Theory and Techniques*, vol. 61, no. 5, pp. 2108-2118, 2013.
- [69] A. T. Mobashsher and A. Abbosh, "CPW-fed low-profile directional antenna operating in low microwave band for wideband medical diagnostic systems," *Electronics Letters*, vol. 50, no. 4, pp. 246-248, 2014.
- [70] R. Karli, H. Ammor and J. Aoufi, "Miniaturized UWB Microstrip Antenna for Microwave Imaging," *WSEAS Transactions on Information Science and Applications*, vol. 11, pp. 122-129, 2014.
- [71] J. D. Dyson and R. Ginyovsky, "Balanced transmission-line measurements using coaxial equipment," *IEEE Transactions on Microwave Theory Techniques*, vol. 19, no. 1, pp. 94-96, 1971.
- [72] J. D. Dyson, "Measurement of near fields of antennas and scatterers," *IEEE Transactions on Antennas and Propagation*, vol. 21, pp. 446-460, 1973.
- [73] D. F. Bowman and E. F. Kuester, "Impedance matching, broadbanding, and baluns," in *Antenna Engineering Handbook*, McGraw Hill, 2007, pp. 52-26-52-27.
- [74] P. D. Carberry, A. Nazarian and S. N. Makarov, "Cavity-backed slotted patch antennas radiating into a lossy human body," in *10th European Conference on ANtennas and Propagation (EuCAP16)*, 2016.
- [75] P. D. Carberry, A. Nazarian and S. N. Makarov, "Slotted patch antennas at 0.3-3 GHz radiating into a lossy human body for microwave imaging," in *39th Antenna Applications Symposium*, 2015.

- [76] S. N. Makarov, G. M. Noetscher, J. Yanamandala, M. W. Piazza, S. Louie, A. Prokop, A. Nazarian and A. Nummenmaa, "Virtual Human Models for Electromagnetic Studies and Their Applications," *IEEE Rev Biomed Eng*, vol. 10, pp. 95-121, 2017.
- [77] R. B. Martin, D. B. Burr and N. A. Sharkey, *Skeletal Tissue Mechanics*, Springer, 1988.
- [78] J. Sierpowska, *ELectrical and Dielectric Characterization of Trabecular Bone Quality*, University of Kuopio, 2007.
- [79] D. A. Chakkalakal, M. W. Johnson, R. A. Harper and J. L. Katz, "Dielectric properties of fluid-saturated bone," *IEEE Transactions on Biomedical Engineering*, vol. 27, pp. 95-100, 1980.
- [80] A. Peyman, C. Gabriel, E. Grant, G. Vermeeren and L. Martens, "Variation of the dielectric properties of tissues with age: the effect on the values of SAR in children when exposed to walkie-talkie devices," *Physics in Medicine and Biology*, vol. 54, pp. 227-241, 2009.
- [81] ICNRP, "Guidelines for limiting exposure to time-varying electric magnetic and electromagnetic fields (up to 300 GHz)," *Health Phys*, vol. 74, no. 4, pp. 494-522, 1998.
- [82] J. A. Kanis and et al, "The use of clinical risk factors enhances the performance of BMD in the predication of hip and osteoporotic fractures in men and women," *Osteoporosis Int*, vol. 18, pp. 1033-1046, 2007.
- [83] S. U. University of Sheffield, "Fracture Risk Assessment Tool," [Online]. Available: <https://www.sheffield.ac.uk/FRAX/>.
- [84] N. B. e. a. Asan, "Characterization of the fat channel for intra-body communications at R-band frequencies," *Sensors*, vol. 18, p. E2752, 2018.
- [85] J. S. Petrofsky, M. Prowse and E. Lohman, "The influence of ageing and diabetes on skin and subcutaneous fat thickness in different regions of the body.," *The Journal of Applied Research*, vol. 8, pp. 55-61, 2008.

- [86] S. M. Garn, "Fat patterning and fat intercorrelations in the adult male," *Human Biology*, vol. 26, pp. 59-69, 1954.
- [87] F. Rosenblatt, "The Perceptron - a perceiving and recognizing automaton," Cornell Aeronautical Laboratory, Buffalo, NY, 1957.
- [88] D. Zhao, T. Wang and F. Chu, "Deep convolutional neural network based planet bearing fault classification," *Computers in Industry*, vol. 107, pp. 59-66, 2019.
- [89] B. Liang, S. D. Iwanicki and Y. Zhao, "Applicaiton of power specrum, cepstrum, higher order spectrum and neural network analyses for induction motor fault diagnosis," *Mechanical Systems and Signal Processing*, vol. 39, no. 6, pp. 342-360, 2013.
- [90] V. Srinivasan, C. Eswaran and N. Sriaam, "Artificial neural network based epileptic detection using time-domain and frequency-domain features," *Journal of Medical Systems*, vol. 29, no. 6, pp. 647-660, 2005.
- [91] X. Yu, C. Ye and L. Xiang, "Applicaiton of artificial neural network in the diagnostic system of osteoporosis," *Neurocomputing*, vol. 29, no. 6, pp. 376-381, 2005.
- [92] A. B. Shaikh, M. Sarim, S. K. Raffat, K. Ahsan, A. Nadeem and M. Siddiq, "Artificail neural netowrk: a tool for diagnosing osteoporosis," *Research Journal of Recent Sciences*, vol. 214, pp. 376-381, 2016.
- [93] J. S. Chiu, Y. C. Li, F. C. Yu and Y. F. Wang, "Applying an artifical neural networkto predict osteoporosis in the elderly," *Studies in health technology and informatics*, vol. 124, p. 609, 2006.
- [94] T. Illou, C. N. Anagnostopoulos, I. M. Stephanakis and G. Anastassopoulos, "A novel data preprocessing method for boosting neural network performance: a case study in osteoporosis detection," *Information Sciences*, vol. 380, pp. 92-100, 2017.
- [95] D. A. Woten, J. Lusth and M. El-Shenawee, "Interpreting Artificial Neural Networks for Microwave Detection of Breast Cancer," *IEEE Microwave and Wireless Components Letters*, vol. 17, no. 12, pp. 825-827, 2007.

- [96] P. Rashidi, M. Ei-Shenawee and D. Macias, "Microwave imaging of three-dimensional malignant breast tumors employing an enhanced evolution strategy," in *2005 IEEE Antennas and Propagation Society International Symposium*, 2005.
- [97] B. Gerazov and R. C. Conceicao, "Deep learning for tumour classification in homogeneous breast tissue in medical microwave imaging," in *IEEE EUROCON 2017 -17th International Conference on Smart Technologies*, 2017.
- [98] S. Costanzo, A. Flores and G. Buonanno, "Machine Learning Approach to Quadratic Programming-Based Microwave Imaging for Breast Cancer Detection," *Sensors*, vol. 22, no. 11, p. 4122, 2022.
- [99] J. L. Muerle, "The Perceptron—a perceiving and recognizing automaton," DTIC, 1963.
- [100] W. S. McCulloch and W. Pitts, "A logical calculus of the ideas immanent in nervous activity," *The bulletin of mathematical biophysics*, vol. 5, pp. 115-133, 1943.
- [101] X. Glorot and Y. Bengio, "Understanding the difficulty of training deep feedforward neural networks," in *Proceedings of the Thirteenth International Conference on Artificial Intelligence and Statistics*, Sardinia, 2019.
- [102] A. Abdelmohsen, "Comparison of central and peripheral bone mineral density measurements in postmenopausal women," *Journal of Chiropractic Medicine*, vol. 16, no. 3, pp. 199-203, 2017.
- [103] M. Malekzadeh and e. al., "MDCT-QCT, QUS and DXA in healthy adults: an intermodality comparison," *Medical Journal of the Islamic Republic of Iran*, 2019.
- [104] J. Adams, Z. Zhang, G. Noetscher, A. Nazarian and S. Makarov, "Application of Neural Network Classifier to Radiofrequency-based Osteopenia/Osteoporosis Screening," *IEEE Journal of Translational Engineering in Health and Medicine*, vol. 9, 2021.
- [105] A. S. M. Alqadami, A. Trakic, A. Stancombe, B. Mohammend, K. Bialkowski and A. Abbosh, "Flexible Electromagnetic Cap for Head Imaging," *IEEE Transactions on Biomedical Circuits and Systems*, vol. 14, no. 5, 2020.

- [106] A. S. M. Alqadami, A. Stancombe, K. Bialkowski and A. Abbosh, "Flexible Meander-line Antenna Array for Wearable Electromagnetic Head Imaging," *IEEE Transactions on Antennas and Propagation*, vol. 69, no. 7, 2021.
- [107] ITU, "Chapter II - Frequencies," in *Radio Regulations*, ITU, 2020, p. 63.
- [108] G. Noetscher, P. Serano, W. Wartman, K. Fujimoto and S. Makarov, "Visible Human Project (R) femal surface based computational phantom (Nelly) for radio-frequency safety evaluation in MRI coils," *PLoS One*, vol. 16, no. 12, 2021.
- [109] Human Connectome Project, "Human Connectome Project 2020," [Online]. Available: <http://www.humanconnectomeproject.org>.
- [110] A. T. Htet, E. H. Burnham, G. M. Noetscher, D. N. Pham, A. Nummenmaa and S. N. Makarov, "Collection of CAD Human Head Models for Electromagnetic Simulations and their Applications," *Biomedical Physics and Engineering Express*, vol. 5, no. 6, 2019.
- [111] N. Joachimowicz, B. Duchene, C. Conessa and O. Meyer, "Anthropomorphic Breast and Head Phantoms for Microwave Imaging," *Diagnostics*, vol. 8, no. 4, p. 85, 2018.
- [112] G. K. Soni, A. Rawat, D. Yadav and A. Kumar, "2.4 GHz Antenna Design for Tumor Detection of Flexible Substrate for On-body Biomedical Application," in *2021 IEEE Indian Conference on Antennas and Propagation (InCAP)*, 2021.
- [113] M. T. Islam, S. Kibria, M. Samsuzzaman, K. Mat and M. T. Islam, "A Modified Side Feeding Directional Antenna for Microwave Imaging Applications," in *2018 IEEE International RF and Microwave Conference (RFM)*, 2018.
- [114] A. Arayeshina, S. Amiri and A. Keshtkar, "Miniaturized on-body antenna for small and wearable brain microwave imaging systems," *Int'l Journal of RF and Microwave Computer-Aided Engineering*, vol. 30, no. 4, pp. 1096-4209, 2020.
- [115] H. Peng, F. Long and C. Ding, "Feature Selection Based on Mutual Information Criteria of Max-Dependency, Max-Relevance and Min-Redundancy," *IEEE Transactions on Pattern Analysis and Machine Intelligence*, vol. 27, no. 8, p. 2, 2005.

- [116] D. P. Kingma and J. Ba, "Adam: A Method for Stochastic Optimization," in *Proceedings of the 3rd International Conference for Learning Representations*, San Deigo, 2017.
- [117] Mini-Circuits, "Mini-Circuits," [Online]. Available: <https://www.minicircuits.com/>. [Accessed 4 10 2022].
- [118] Advanced Circuits, "Standard & Custom Printed Circuit Boards," [Online]. Available: <https://www.4pcb.com/pcb-manufacturing-custom-standard.html>. [Accessed 4 10 2022].
- [119] Mini-Circuits, "HSAWA2-30DR+; Absorptive SPDT, SMT Solid State Switch, DC - 3000 MHz, 50Ω," 2017. [Online]. Available: <https://www.minicircuits.com/WebStore/dashboard.html?model=HSAWA2-30DR%2B>. [Accessed 4 10 2022].

Appendix A. Prior Art Study Subject Roster

Table 4 Study roster (from left to right): subject number, category score (1-5), age, weight, height, sex, left wrist circumference, and right wrist circumference.

Subject #	Osteo Category	Age	Weight [lbs]	Height [ft]	Sex	L. Wrist Circ. [in]	R. Wrist Circ. [in]
1	5	55	130	5 1/3	f	5 3/8	5 5/8
2	5	81	140	5 1/6	f	6 3/4	6 1/2
3	5	74	168	5 4/7	f	6 3/4	7 1/8
4	5	80	139	5	f	8	8
5	5	86	130	4 1/2	f	5	5 1/4
6	4	55	145	5 1/2	f	6	6 1/8
7	4	80	170	5 1/3	m	7	7
8	4	85	153	5	f	5 3/4	5 3/4
9	4	56	138	5 3/7	f	6 3/8	6 1/2
10	4	83	128	5	f	5 3/4	6 1/2
11	4	82	188	5	f	7	7
12	4	69	177	5 3/7	f	7 1/4	7 1/4
13	4	84	140	5 1/6	f	6 3/4	7
14	4	88	138	5	f	6	6
15	4	79	158	4 5/6	f	6 5/8	6 5/8
16	4	76	180	5 1/6	f	8 1/4	8 1/4
17	4	84	150	5	f	5 3/4	5 3/4
18	4	90	134	4 3/4	f	6 1/2	6 1/4
19	4	87	180	5 1/6	f	7 3/8	7 1/2
20	4	80	115	4 5/6	f	5 3/4	6
21	4	79	148	5 1/6	f	6 1/4	7
22	4	78	172	5	f	7 1/2	7 3/4
23	4	72	150	5 1/3	f	5 3/4	6
24	3	56	190	5 1/3	f	6 1/2	6 3/4
25	3	50	155	5 3/7	f	5 1/2	5 3/4
26	3	55	170	5 1/2	f	6 1/4	6 1/4
27	3	58	110	5 1/4	f	5 3/8	5 1/2
28	3	54	145	5 2/3	f	6 1/4	6 1/4
29	3	75	155	5 3/4	m	7	7 1/8
30	3	64	150	5 4/5	m	6 4/5	7
31	3	77	125	5 1/3	f	6	6
32	3	44	120	5 1/4	f	5 1/4	5 3/4
33	3	57	145	5 1/3	f	6 3/8	6 1/4
34	3	56	190	5 1/2	m	7 3/4	8
35	3	44	139	5 3/7	f	6 1/4	6 1/4
36	2	42	156	5	f	6	6
37	2	51	160	5 1/6	f	5 3/8	5 3/4
38	2	50	175	5 3/4	m	6 3/4	6 3/4
39	2	60	160	5	f	7	7

40	2	62	186	5 1/2	m	7 1/2	7 1/2
41	2	63	142	5 1/4	f	6 1/2	6 1/2
42	2	47	218	5 5/6	m	7 3/4	7 3/4
43	2	71	163	5 4/7	f	6 7/8	7
44	2	58	200	5 3/4	m	7	7 1/4
45	2	69	190	5 2/3	m	7 1/4	7
46	2	79	189	5 2/3	f	7 3/4	7 1/2
47	2	74	179	5 1/3	f	7 7/8	7 5/8
48	2	82	188	5	f	7	7
49	2	86	165	5 1/2	f	6 5/8	6 3/4
50	2	67	217	5 1/3	f	7 1/4	7 1/2
51	2	72	180	5 1/4	f	7 1/2	8
52	2	72	185	5 3/7	f	7 1/4	7 1/4
53	2	78	142	5	f	7 1/4	7 1/4
54	2	69	191	5	f	7 1/4	7 3/8
55	2	72	159	5	f	7	7
56	2	72	170	5 1/2	f	7 1/2	8 1/8
57	2	78	201	5 1/6	f	8 1/8	8 1/4
58	2	62	180	5 1/4	f	7 3/8	7 1/2
59	2	80	175	5	f	7	6 5/8
60	2	72	190	5 3/7	f	7 1/8	7 1/8
61	2	70	182	5	f	7 1/2	7 5/8
62	2	69	182	5 1/4	f	7 1/2	7 1/2
63	2	81	150	5	f	6 3/8	6 5/8
64	2	94	156	4 2/3	f	6 3/4	6 7/8
65	2	60	152	5 1/6	f	5 1/4	5 1/4
66	2	60	220	5 1/6	m	7 3/4	7 1/2
67	2	65	180	5 5/6	m	6 3/4	6 7/8
68	1	28	152	5 1/3	f	6 3/4	6 1/2
69	1	29	256	5 3/4	m	8	8 1/4
70	1	30	198	5 3/4	m	7 1/4	7
71	1	23	185	5 5/6	m	6 7/8	6 5/8
72	1	26	124	5 1/3	f	6	6

Appendix B. Modeling and Experimental Results for Microwave Imaging of a Hip with Emphasis on the Femoral Neck

This study consists of a set of simulations to determine field propagation inside the body validated by *in vivo* experimental measurements under the same conditions. The simulations produced models that included reflection coefficient S_{11} and transmission coefficient S_{21} in addition to the fields. These S -parameters can be measured in a physical setup using a network analyzer. The simulations and physical measurements were performed with the same antennas [8]. Additional simulations were performed with different antennas to investigate wideband measurements; these were not verified experimentally. The simulation results were analyzed primarily based on the electric field and Poynting vector.

This study was divided into two parts: first, a set of *in vivo* measurements using real antennas and second, a set of simulations using a corresponding human body model. The measurements were taken with Institutional Review Board (IRB) approval (IRB-19-0123) through Worcester Polytechnic Institute. The same human subject was used for all *in vivo* measurements.

B.1. Experimental Hardware

The antennas featured in this study are dual antiphase patch antennas [8] built using copper on FR4. Two sets of antennas, shown in Fig. 30, were investigated.

Set A (resonators: 2.0 cm x 1.4 cm, ground-plane: 5.0 cm x 1.9 cm) connected to matching networks that match them to 675 MHz. Matching networks were built with lumped components and applied at the antenna feeds, after the 180° power splitter (Mini-Circuits® ZFSCJ-2-232-S+, 5 MHz to 2.3 GHz).

Set B (resonators: 2.5 cm x 1.6 cm, ground-plane: 3.0 cm x 8.0 cm) were not matched to any particular frequency. The antenna feeds connected directly to the 180° power splitter (Mini-Circuits® ZFRSC-183-S+, DC to 1.8 GHz).

Both antennas had 0.5 cm spacing between the resonators. The antennas were connected to a Keysight FieldFox N9914A network analyzer. The network analyzer transmitted at -15 dBm over a frequency range of 30 kHz to 2 GHz at 401 points. The magnitude in dB and

phase in degrees of S_{11} and S_{21} were saved to a CSV-file. The measurements were each a single frequency sweep.

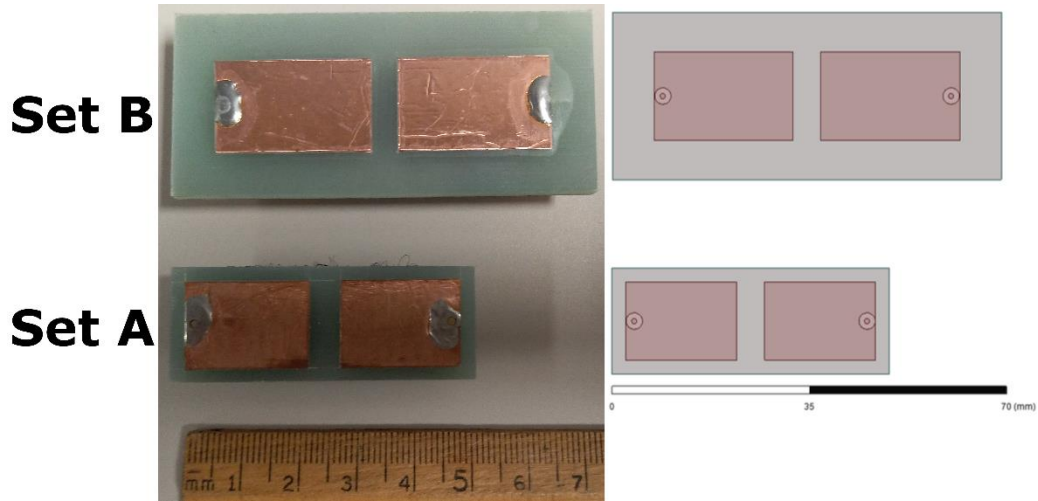


Fig. 30. Comparison of size between antennas from Set B (top) and from Set A (bottom). The left two are the physical antennas and the right two are the corresponding CAD models. The spacing between patches in both antennas is 0.5 cm. Antennas in Set A had resonators of 2 cm x 1.4 cm and a ground-plane of 5 cm x 1.9 cm. Antennas in Set B had resonators of 2.5 cm x 1.6 cm and a ground-plane of 3 cm x 8 cm. The antennas were fed from the back, the solder joints in the figure are the feeds.

B.2. Measurement Sites

To test the viability of various sites for measuring transmission through the femoral neck, we first checked using both sets of antennas to determine if meaningful transmission could occur given the positions of the antennas. The exact positions investigated are shown in Fig. 31.

The positions investigated were:

1. On the side of the body, positioned over the greater trochanter.
2. On the side of the body, positioned next the iliac crest. The antenna in this position was rotated in the plane of the drawing in Fig. 31 to investigate different polarizations. The orientation shown in the figure (vertically aligned with the body and the antenna in position 1) was considered 0° , and rotation angles were measured toward the front of the body (clockwise on the right side, counterclockwise on the left side).
3. On the front of the body, positioned over the anterior superior iliac spine.
4. On the rear of the body, positioned over the top edge of the gluteus maximus.
5. On the front of the body, positioned horizontally in the same horizontal plane as the greater trochanter.

On the rear of the body, positioned horizontally and below the gluteus maximus.

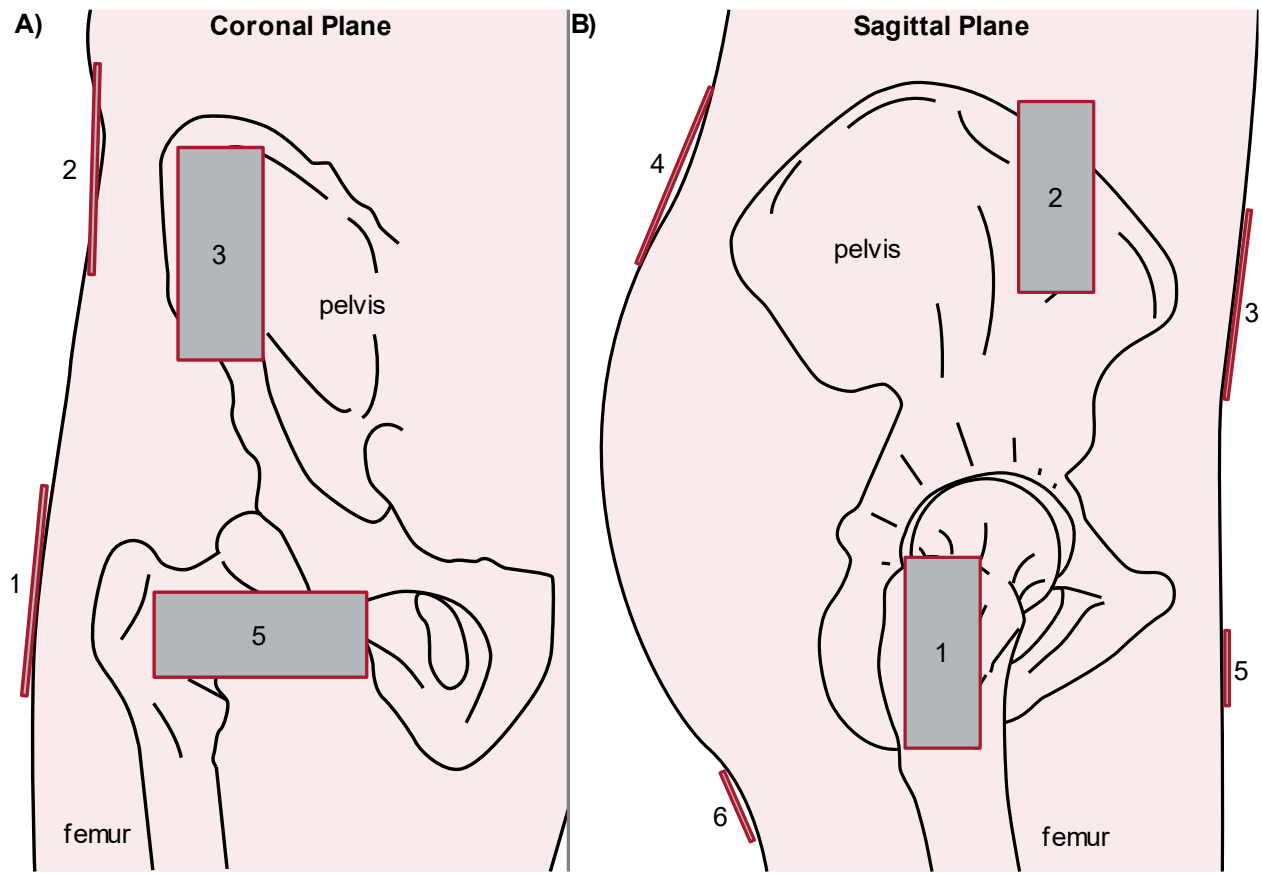


Fig. 31. A) Front (coronal plane) view of the right side of the body with antenna positions by number. B) Right side (sagittal plane) view of the body with antenna positions noted by number. In both, the skin profile, right pelvis, and right femur are shown in addition to the antennas. Antennas were pushed against the body such that gaps, such as the one near position 4, were not present during the measurement. The antenna in position 4 was located over the posterior iliac crest.

Measurements were taken between two of the positions. The antennas were held to the body by the subject being measured, by pressing on the center of the ground plane of each antenna. This ensured deformation of the body so that the total length of the antenna was contacting skin. The positions that were not in use for a given measurement did not have antennas present. All position combinations measured were measured with both Set A and Set B antennas.

B.3. Simulated Antenna Positioning and Human Body Model

Antenna positions on the simulated body model were the same as those on the *in vivo* model and are shown in Fig. 32. The base CAD model is the Ansys male human model. It was chosen to match the *in vivo* subject, who is male.

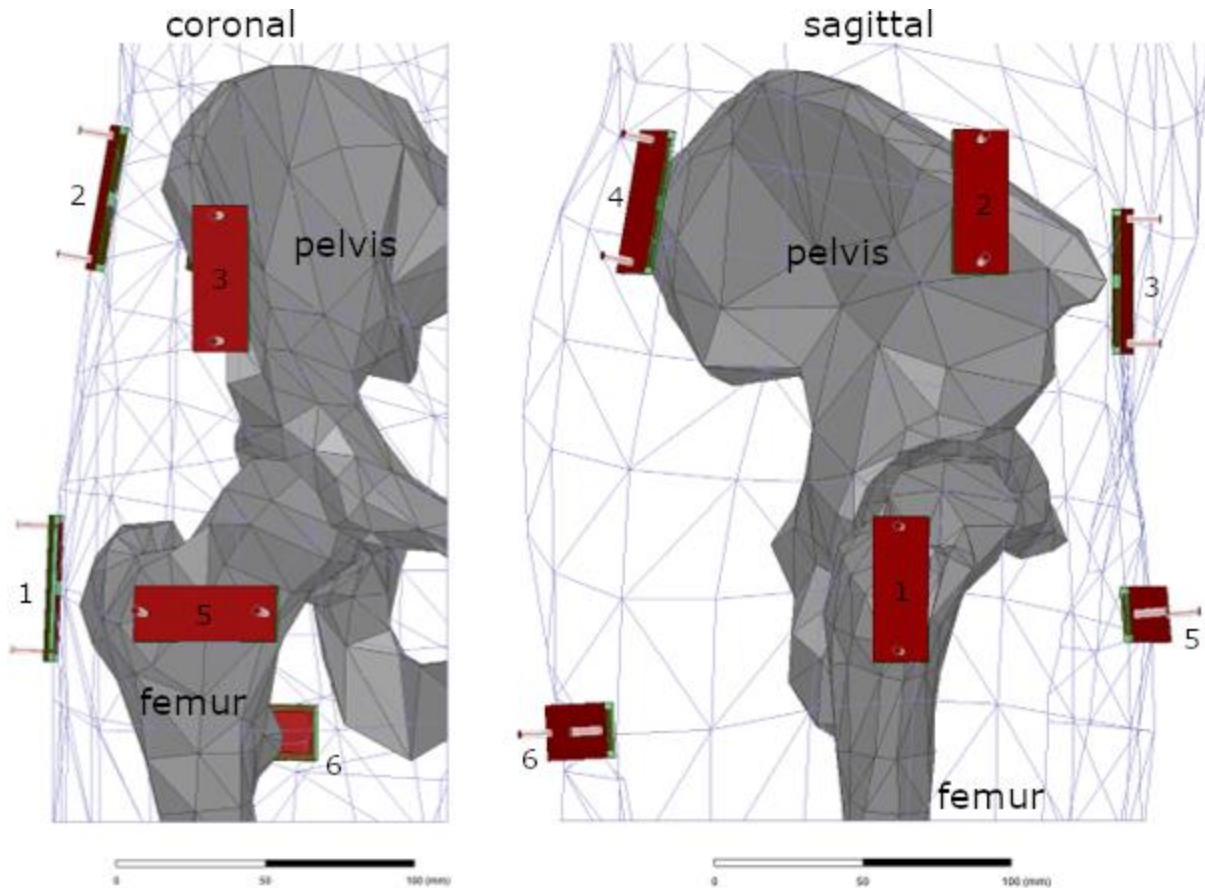


Fig. 32. a) Front (coronal plane) view of the right side of the CAD model with antenna positions by number. b) Right side (sagittal plane) view of the CAD model with antenna positions noted by number. In both, the wireframe body shell, right pelvis, and right femur are shown in addition to the antennas. The body shell was flattened or Boolean-subtracted using the antenna's shape to eliminate gaps and ensure good coupling at each position. The apparent difference in location of position 4 is due to perspective of the drawing in Fig. 31.

The CAD model includes the full body with bones, muscles, and fat modelled throughout. Some skin layers and fat deposits are represented in aggregate by a volume with the average electric properties of the human body. Cartilage in joints, such as the hip joint, is not modelled by default. We investigated the effects of cartilage by producing a new shell using the area between the femur and pelvis making up the ball joint. This new volume was between 3 to 10 mm thick due mostly to the large-triangle tessellation of the bones' shells. In addition, two outer skin shells were added with properties derived from the VHP-Female v.5.0 model [108].

B.4. Software Modelling of Matched Antennas

The matching networks were modelled in Ansys using S-Parameter measurements of the physical matching networks. The matching networks' measurements were taken over the

same frequency range (30 kHz to 2 GHz) and with the same resolution (401 points) as the *in vivo* transmission measurements. However, they were taken at 0 dBm and averaged across 8 sweeps, whereas the *in vivo* measurements were taken at a lower power (-15 dBm, see above) and with only a single frequency sweep. The input ports were all 50 Ω characteristic impedance, identical to the physical network analyzer. The 180° power splitters were modelled with an ideal splitter model. Fig. 33 shows a typical simulation configuration for a single antenna at position 1 compared to a physical measurement at the same site.

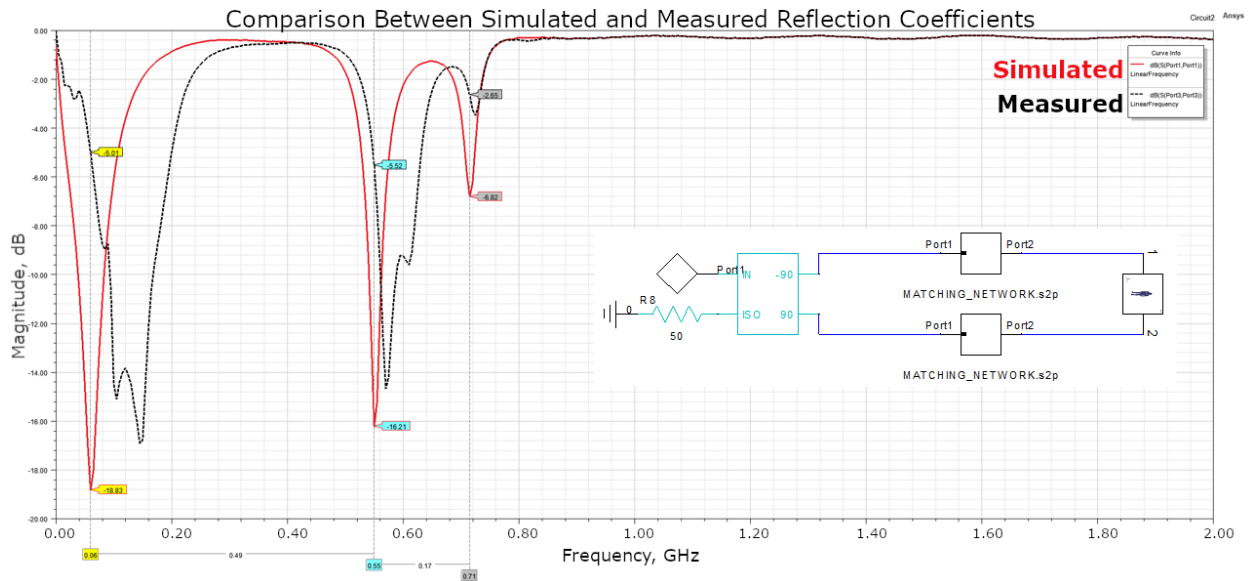


Fig. 33. Comparison of reflection coefficient magnitude $|S_{11}|$ for the simulated antenna (red) and the *in-vivo* antenna (dashed black). This figure additionally shows the configuration of the matching and power splitting circuits in HFSS for the simulated curve. Both the simulated and measured curves were produced from antennas at position 1.

B.5. In Vivo Measurement Results

The positions shown in Fig. 31 are positions between which transmission was achieved. Additional sites were measured, including one between sites 4 and 6 through the center of the gluteus maximus, but no meaningful signal was received. Fig. 34 shows the transmission coefficient for a selection of antenna position pairs using Set A, while Fig. 35 shows the transmission coefficient for the same position pairs using Set B.

Set A, S_{21} for Various Paths

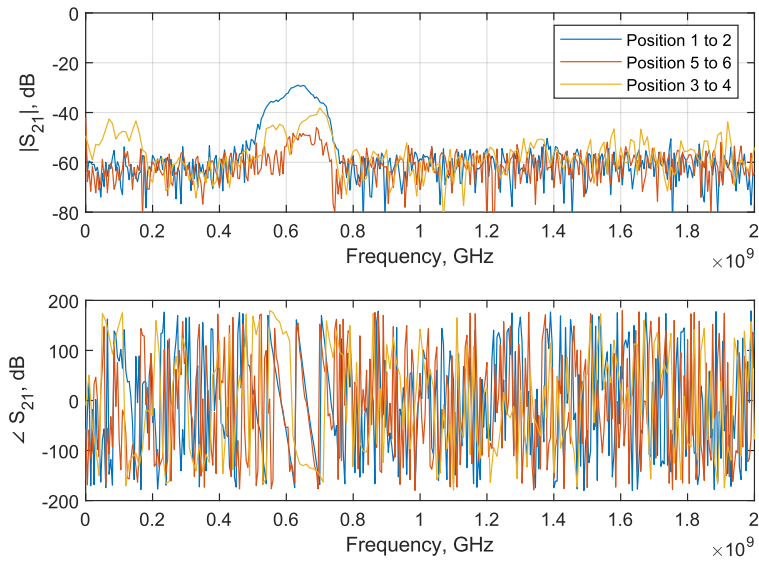


Fig. 34. Comparison of transmission coefficient S_{21} when using antennas from Set A for three propagation paths: First, position 1 to position 2, a semicircular path through the compartment. Second, position 5 to position 6, a straight path through the upper femur. Third, position 3 to position 4, a straight path through the upper pelvis.

Set B, S_{21} for Various Paths

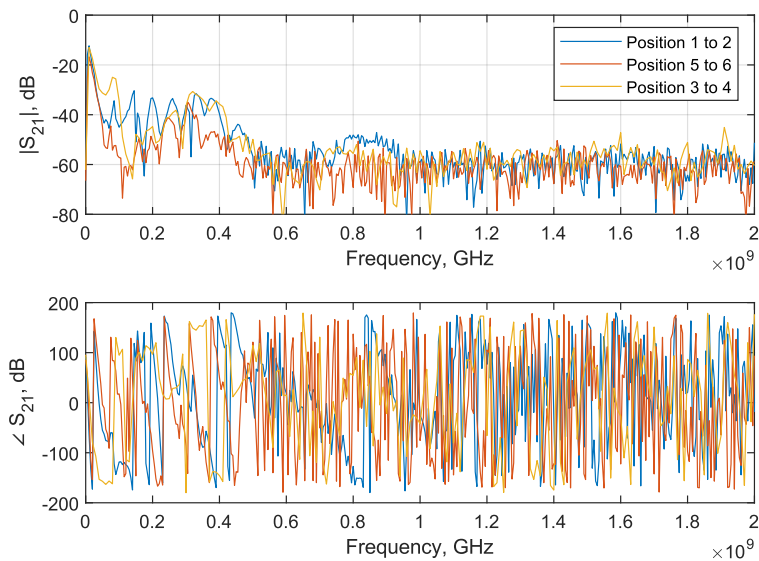


Fig. 35. Comparison of transmission coefficient S_{21} when using antennas from Set B for three propagation paths: First, position 1 to position 2, a semicircular path through the compartment. Second, position 5 to position 6, a straight path through the upper femur. Third, position 3 to position 4, a straight path through the upper pelvis.

In addition to the measurements shown in the figures, transmission from position 1 to position 2 was measured with varying polarizations achieved by rotating the position 2 antenna in 45° increments. For Set A, the highest average transmission over the bandwidth of the antenna transmission was seen at 45° of rotation while the lowest at 135°. Set B was less consistent but showed similar results: minimum transmission at 270° and maximum at either 45° (on the left side of the body) or 135° (on the right side). Overall, Set B showed less change in S_{21} over various angles of rotation than Set A, potentially due to noise. Set A showed differences of S_{21} at the same frequency within the passband of the antenna with different polarizations up to 20 dB, while Set B showed differences up to only 10 dB. Lying down during the measurement process decreased this variation by about half. Table 5 shows the maximum measured magnitude of the transmission coefficient for each orientation tested, for both sets of antennas.

Table 5: Maximum transmission coefficient magnitude $|S_{21}|$ for various relative polarizations using both sets of antennas on the right leg. Measured from position 1 to position 2.

Angle, degrees	Set A, Right Leg		Set B, Right Leg	
	f , MHz	$ S_{21} $, dB	f , MHz	$ S_{21} $, dB
0 (co-polarized)	615.0	-38.663	10.0	-12.254
45	635.0	-29.127	10.0	-12.066
90 (cross-polarized)	695.0	-42.658	10.0	-13.860
135	705.0	-39.581	10.0	-11.955
180 (co-polarized)	705.0	-37.817	10.0	-12.741
225	600.0	-36.861	10.0	-12.891
270 (cross-polarized)	710.0	-39.151	10.0	-14.000
315	705.0	-37.694	10.0	-12.057

B.6. Simulation Results

First, the relative agreement between the simulated and measured results is characterized by Fig. 36, in which there are resonances at approximately the same frequencies in the measured and simulated environments, but the simulated environment experiences significantly more attenuation on transmission than the measured environment.

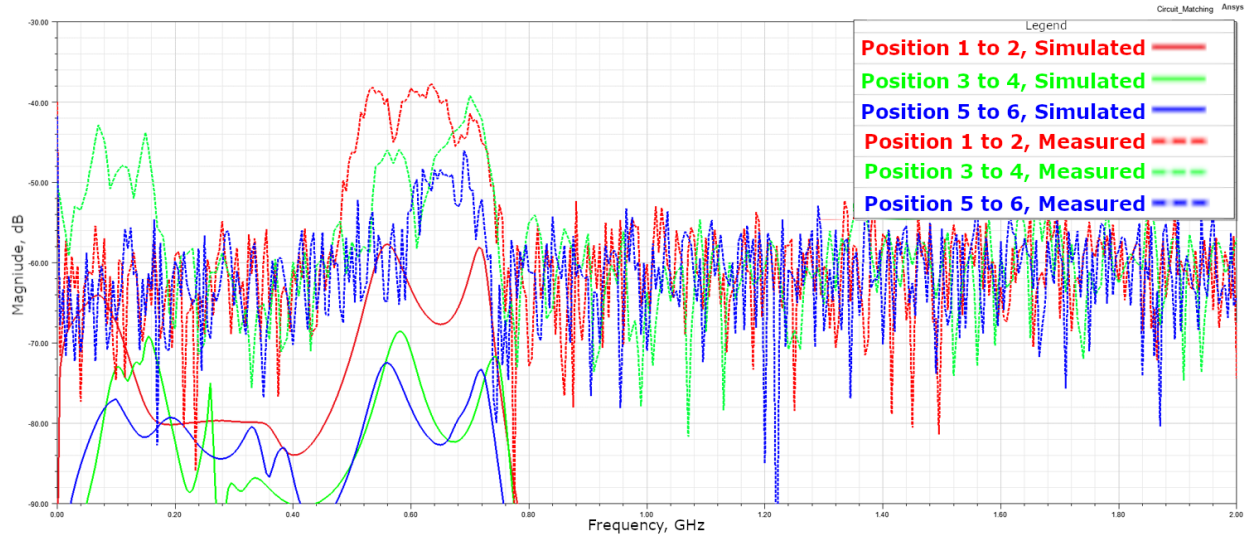


Fig. 36. Comparison of transmission coefficient S_{21} when using antennas from Set A for three propagation paths: First (red): position 1 to position 2, a semicircular path through the compartment. Second (blue): position 5 to position 6, a straight path through the upper femur. Third (green): position 3 to position 4, a straight path through the upper pelvis. The dashed lines are the measured in-vivo $|S_{21}|$ (also seen in Fig. 34) and the solid lines are simulated.

Next, the propagation paths of the waves were observed using animated electric field plots in various observation planes and 3-D Poynting vector plots in the bones and the body. At higher frequencies, a surface-propagating wave is present, as seen in Fig. 37. The Poynting vector plots in the femur and pelvis for the three transmission configurations in Figs. Fig. 34, Fig. 35, and Fig. 36 are shown in Fig. 38.

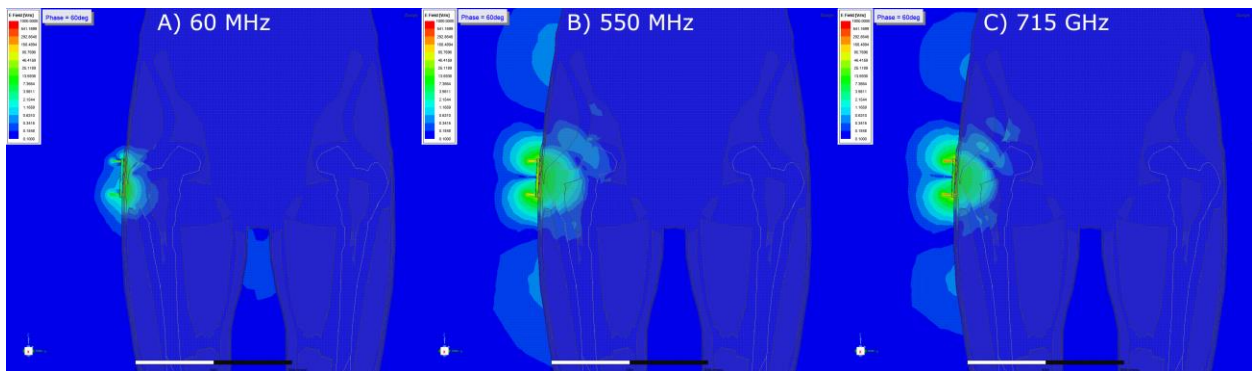


Fig. 37. Electric field magnitude in the sagittal plane at different frequency bands. a) is 60 MHz, b) is 550 MHz, and c) is 715 GHz. All three are snapshots from animations, taken at a phase of 60° . The vertical surface-propagating wave is present in b) and c) but not in a). The antennas for these measurements are the Set A antennas, located at position 1.

In addition to the results shown in the figures, simulations were performed with a dielectric “belt” between the transmitting and receiving antennas to attenuate the surface wave. The

effect was not strong enough to reduce the magnitude of the surface wave to a level comparable to that of the wave propagating through the bone.

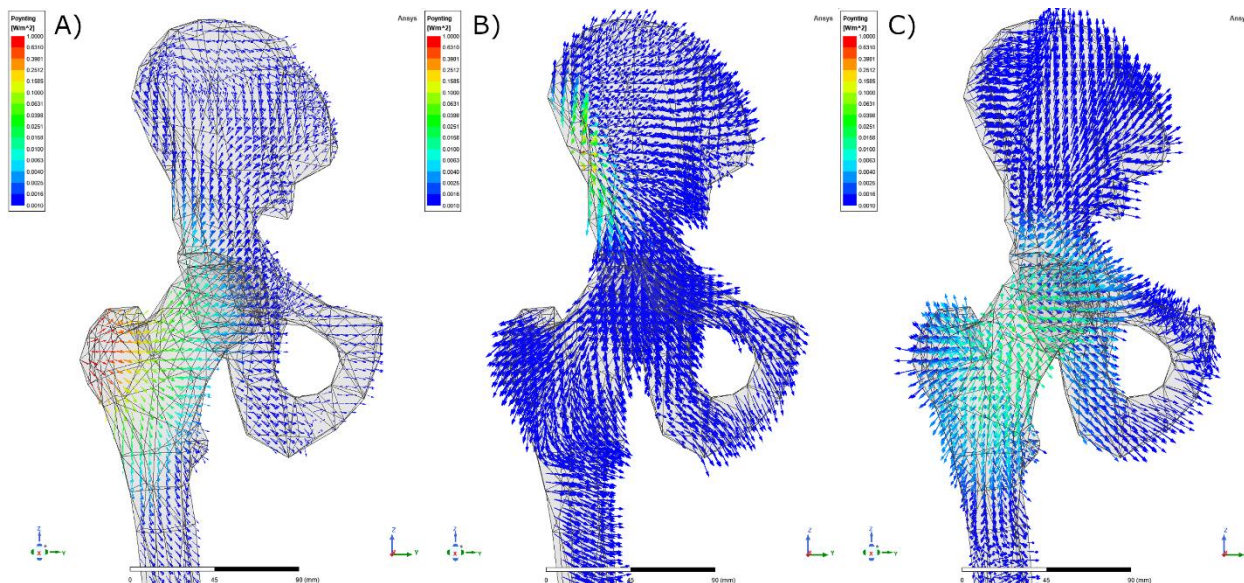


Fig. 38: Poynting vector distribution in the femur and pelvis for three antenna position pairs: a) transmission from position 1 to position 2, b) transmission from position 3 to position 4, and c) transmission from position 4 to position 5. Poynting vector magnitude is represented by color, warmer is larger.

B.7. Limitations

This study only considered the strongest component of the received wave. Simulations suggest that this component likely propagates through skin, fat, and muscle when the antennas are on the same side of the body compartment. The same simulations also suggest propagation occurs through the bone and this second component will accrue some phase shift (delay) relative to the one that propagates through the soft tissue.

This study performed *in vivo* measurements on only one subject, a 26-year-old male, who is not at significant risk of osteoporosis according to standard risk factors.

In vivo spectra were determined from a single frequency sweep; therefore, noise contents in the spectra are more significant than had the measurements been performed using averaging of multiple sweeps.

Matched (Set A) and unmatched (Set B) antennas are not identical and have different resonant frequencies. Set A had a bandwidth of about 230 MHz, centered on about 675 MHz (when matched) and Set B had a bandwidth of about 420 MHz, centered on about 215 MHz.

B.8. Validation of Simulation Using In Vivo Measurement Results

While the measured and simulated results are not a perfect match, the resonant frequencies are collocated in the two spectra for the same antenna set and positions. Some of the difference in transmission coefficient magnitude between the measured and simulated spectra is due to differences between the model and the physical subject. These differences include the level of detail of the CAD model, and differences in physical shape between the CAD model and the subject.

B.9. Propagation Paths and Antenna Position

To achieve transmission through the bone, antennas should be placed on the opposite sides of the body compartment. If placed on the same side of the body compartment, the surface wave has the shortest path between the two antennas and thereby dominates the received signal. Direct transmission across a body compartment, contrarily, puts the shortest path between the antennas through the bone at the center of the compartment, and the Poynting vector for such a setup is the largest at the center of the compartment [6]. This is illustrated in Fig. 38, where the distribution in part C shows more even transmission through the femoral neck than part A. Part C's antennas are transmitting across the compartment while part A's transmit in a u-shape, starting and ending on the same side of the compartment.

B.10. Frequency Choice and Propagation Through Bone

It is common knowledge that lower frequencies provide better human body penetration but lower spatial resolution in microwave imaging. Our simulations have confirmed this, but we also note that in this application we can consider frequencies that are lower than traditionally considered for microwave imaging of the human body, due to the independence of this approach from spatial features. Therefore, a frequency of operation closer to 60 MHz with a reduced surface wave is preferable in this application to a higher frequency. Any waveguide-like effects from higher-frequency waves propagating through bones are overshadowed by the lack of penetration to reach the bones in the first place, and by the large surface-propagating waves produced by these high frequencies.

Further investigation revealed that waveguide-like effects can be observed for electric field propagation in fatty tissue, though these are best observed at higher frequencies. This increases the difficulty of properly placing antennas such that the primary received component is the component that passed through the bone and is therefore useful for the

diagnosis. These effects can be limited by decreasing the thickness of the outer fat layer in the subject's body. Because this isn't generally viable, the authors also note that a phased antenna array and phase-aware signal processing may be used to eliminate these effects, as the fat-layer path propagates the electric field noticeably faster compared to the central (bone) path. It may also be possible to build a system with a time delay on the receiver that blocks the faster signal from the fat layer but accepts the slower signal from the central path, thereby avoiding the need for a phased array and the associated hardware and processing.

Appendix C. Additional Exploration of Machine Learning Techniques for Osteoporosis Detection

This project had two aims: first, to use data augmentation techniques on the existing data to investigate its effect on the trained classifier(s) and, second, to use dimension-reduction techniques to better understand which features are most important to classification.

The motivation for the first aim was simply to increase the sensitivity and specificity of the classifier compared to one trained with only real data. The motivation for the dimension reduction was primarily to aid in design efficiency: by targeting certain frequencies and ignoring others the measurement hardware can be made much cheaper. Secondly, reducing the number of features could help with visualization and could theoretically speed the training of a classifier without losing much sensitivity or specificity.

C.1. Base Data

All the data used in this study was collected for previous studies with IRB approval (IRB-19-0123) through Worcester Polytechnic Institute on Oct. 1, 2018. The data consisted of 80 subjects total (age range 23-94 years old, 60 females, 20 males) shown in Fig. 16 on page 46, of which 66 were suitable for a dichotomous diagnostic test [104]. Suitability was determined by clinical risk factors of osteoporosis: if a subject was easily classifiable as osteoporotic or healthy from their clinical risk factors alone or had an available DXA T-score from the past year, that subject was suitable for the test. Subjects whose clinical risk factors were split some indicating healthy and some indicating osteoporosis who did not have an available T-score were considered unknown and discarded from the test. These subjects were split into the same two groups from [104]:

Group 1 (Osteopenic/Osteoporotic): 25 subjects (24 female, 1 male). Subjects were characterized by a T-score less than -1 taken within one year. Subjects with a T-score less than -2.4 were considered osteoporotic while other subjects were considered osteopenic.

Group 2 (Healthy): 41 subjects (25 female, 16 male). Subjects in this group did not necessarily have a known T-score, but instead were characterized by having none of the following risk factors: a history of bone fractures, medication for bone-related diseases, a family history of bone fractures, and/or osteoporosis.

Each arm from each base subject was considered as a separate subject for this study, so the base dataset contained 132 subjects, each with a single arm's worth of data. Each arm consisted of 403 features, 402 of which were frequency points (real and imaginary) and one was wrist circumference.

C.2. Data Augmentation

The goal of the data augmentation was to provide some noise to the spectra without losing their class-defining characteristics. Because of simulations done for [6], we believe the difference between classes will likely manifest in the form of resonant frequency shift, as shown in Fig. 6 on page 23.

Adding a large amount of noise, especially uniform noise, to the spectra would risk losing these resonance shifts. On the other hand, not adding enough noise encourages overfitting by not differentiating the new spectra significantly from the old spectra. To address this, I added two separate Gaussian random variables as noise sources when generating the augmented data.

The first was added to each data value and had a small standard deviation, relative to the standard deviation of each feature. To apply this to any subject ξ , I took the transmission coefficient spectrum for that subject $S_{21}(\xi, f)$ and added it to the random variable Φ .

$$S'_{21}(\xi, f) = S_{21}(\xi, f) + \frac{\sigma(f)}{50} \Phi(\xi, f) \quad (1B)$$

Where Φ is a normally distributed (Gaussian, zero-mean, unit-variance) random value, then multiplied by the variance of the feature $\sigma(f)$ it was being added to. Unique values of Φ are generated for every combination ξ and f . To reduce the chances of losing critical information, this value was divided by 50.

To add more variability without losing critical information, we can also add a per-subject bias. Because this is applied uniformly across all features for a given subject, its variance can be larger without effecting the critical part of the data. To do this, we modify the result from Eqn. 1B as follows:

$$S''_{21}(\xi, f) = S'_{21}(\xi, f) + \frac{\sigma(\xi)}{5} \theta(\xi) \quad (2B)$$

Where $\theta(\xi)$ is another normally distributed random value that is the same for all features for a given subject and $\sigma(\xi)$ is the standard deviation of feature values for the subject. Eqn. 2B describes the full process to create an augmented subject.

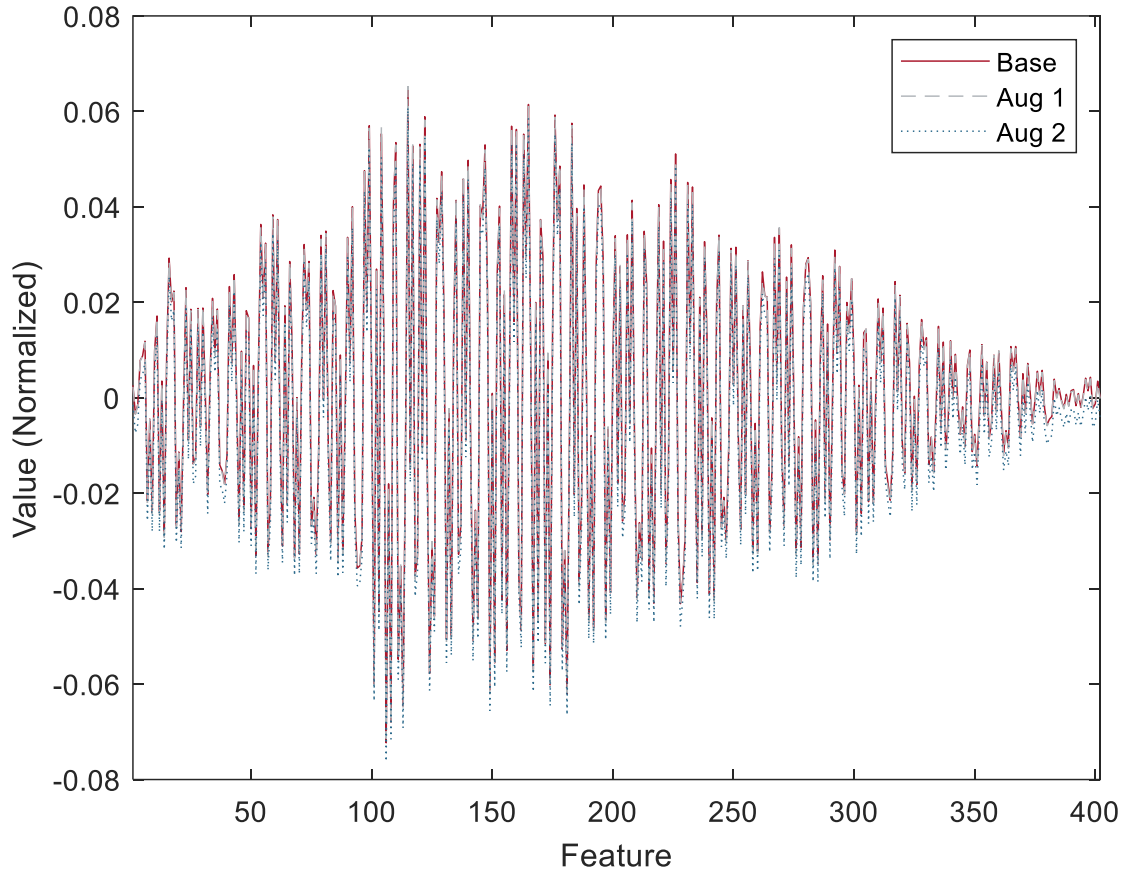


Fig. 39. Base data subject (solid red) compared to the two augmented data subjects that were based on it (dashed grey and dotted blue).

The augmented data, shown in Fig. 39, should therefore have some variability for all features compared to the base data, but should also carry a more significant per-subject bias. Wrist circumferences were not modified when generating augmented subjects, as they were rounded to the nearest quarter inch and had a small range of possible values.

Two augmented subjects were generated from each base subject, therefore the augmented data set contained 396 subjects. The base data was a subset of the augmented data.

C.3. Principal Component Analysis

Principal Component Analysis (PCA) transforms the feature space to one that has rank consistency, with each subsequent component contributing less to the overall diagnosis than

the last. This allows us to easily drop features that do not contribute much to the classification, as they are consistent across all the data. The downside of this approach is that the resulting principal components lose their physical meaning: they are no-longer related to frequency values.

The MATLAB® Statistics and Machine Learning Toolbox™, MathWorks Inc., Natick MA, includes a function to perform unsupervised PCA with various options for solvers and initial conditions. I performed two sets of PCA using the Singular Value Decomposition (SVD) algorithm: one with each feature weighted according to its variance, and one with each feature weighted uniformly. In both cases, I scaled the data so that each feature covered the interval [0,1] and the PCA function biased the input features to be zero-mean before performing PCA.

For the variance based PCA, I orthonormalized the resulting coefficient matrix using Eqn. 3B.

$$C_{\perp} = [I \sigma(f)]^{-1}C \quad (3B)$$

Where C is the non-orthogonal coefficient matrix, I is the identity matrix, $\sigma(f)$ is the standard deviation for each feature and C_{\perp} is the orthonormalized coefficients matrix. This was not necessary for the uniform-weighting, as its coefficient matrix was already orthonormal.

The PCA function directly produced the coefficient matrix, the scores (or feature values in the PCA space) matrix, and the explained variance fraction of each principal component. I performed both kinds of PCA (variance-weighted and uniform-weighted) on both the base dataset and the augmented dataset.

C.4. Feature Selection

My goal with feature selection was to achieve similar results to PCA without losing the physical meaning of the features. The end goal of this would be to streamline the design of the measurement hardware so as to not measure components that don't contribute to classification and make the apparatus more cost-efficient in the process.

I performed feature selection using two functions from the MATLAB® Statistics and Machine Learning Toolbox™. One performed feature selection based on the covariance, χ^2 , and the other used the Minimum Redundancy Maximum Relevance (MRMR) algorithm [115].

When using the χ^2 method, the algorithm binned continuous predictors into 10 bins, the weights for each feature were all initialized to 1, and the prior probabilities for each class were

determined from the class frequencies across the dataset in question. When using MRMR, the weights for each feature were all initialized to 1, and the prior probabilities for each class were determined from the class frequencies across the dataset in question.

Both feature selection functions had two outputs: an index vector that would sort the features by order of importance, and the predictor scores which provide a measure of how important the algorithm thought each predictor was. Notably, the χ^2 algorithm can produce scores of infinity while the MRMR algorithm cannot. Features with non-finite scores were grouped in arbitrary order at the start of the index vector and were considered most important.

Because neither feature selection algorithm produced an explained-variance statistic, I generated an approximation using the ratio of the score to the sum of all scores as shown in Eqn. 4.

$$E(f) = \frac{s_f}{\sum_{i=1}^N s_i} \quad (3B)$$

Where $E(f)$ is the explained variance fraction for feature f where $1 \leq f \leq N$ and N is the number of features. I performed feature selection on both the base dataset and the augmented dataset using both methods.

C.5. Training and Validation

In addition to the PCA and feature selection, I also applied the 2-layer perceptron network from [104] to the augmented data. What I intended to do and what I did for training the network ended up being different. I intended to perform 10-fold cross-validation and retain an 11th fold as the test data, to be evaluated on each of the 10 trained classifiers. What I ended up doing was performing 10-fold cross-validation with 11 folds, such that one fold never took its turn as validation data. This fold was the one intended to be the test data. Different from my previous approach [104] to k-fold cross-validation, wherein I wrote my own code to divide the data into folds, I used the library function `cvpartition`.

Otherwise, the training process was identical to the training process from [104]. All networks were trained using an ADAM [116] solver and a mini-batch size of 27 for 1000 epochs and were evaluated by sensitivity, specificity, and accuracy. This study concentrates on accuracy instead of Youden's J because accuracy is more commonly used in machine learning, which is the context of this paper. Youden's J is more commonly used in medical contexts.

When training the neural network based on the PCA and feature selection results, the networks were trained on the minimum number of components to achieve 95% explained variance.

C.6. PCA Results

The two PCA methods produced results that are visually indistinguishable from each other. As shown in Fig. 40, the PCA succeeded in capturing most of the variance of the spectra in the first few components, but unfortunately this did not lead to clear separation of classes in Fig. 41.

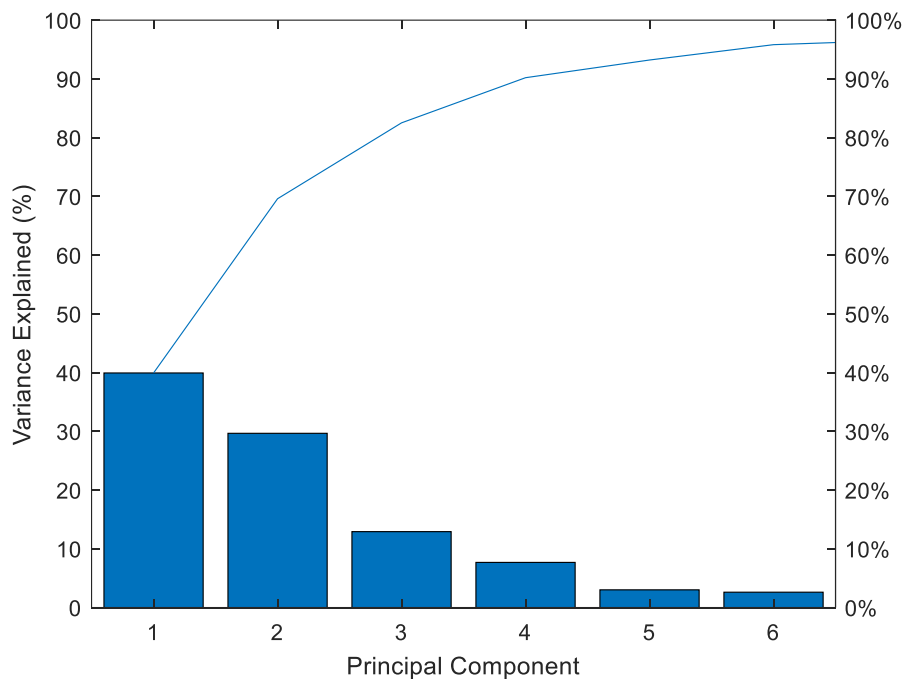


Fig. 40. Principal component explained variance by component (bars) and total explained variance (line) for the 6 most-significant components. Base data, Uniform weights method.

Applying PCA to the augmented data yielded much the same results as the base data. It is notable, however, that the variance-weighted PCA for the augmented data picked up extra spread along the third principal component compared to the uniform weights method and either method for the base data. The first two components remained essentially identical.

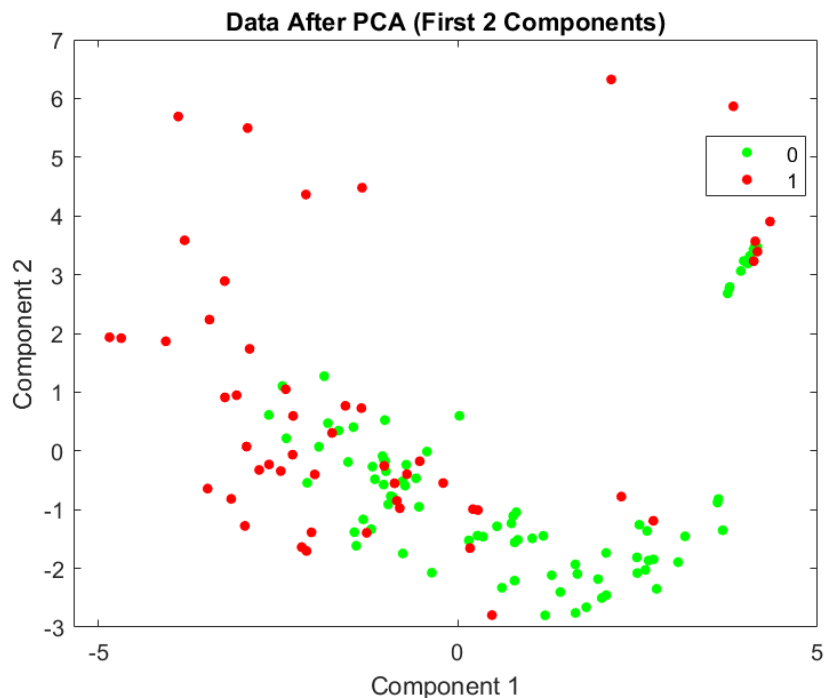


Fig. 41. Plot of the subjects' scores using the first two principal components. Green is Group 2 (Healthy), and red is Group 1 (Osteoporotic). Base data, uniform weights method.

Applying PCA to the augmented data yielded much the same results as the base data. It is notable, however, that the variance-weighted PCA for the augmented data picked up extra spread along the third principal component compared to the uniform weights method and either method for the base data. The first two components remained essentially identical.

For the base data, the first 5 components were sufficient to represent 95% of the variance of the original spectra by both methods.

For the augmented data, the first 6 components were sufficient to represent 95% of the variance of the original spectra by both methods.

C.7. Feature Selection Results

Feature selection using the χ^2 method produced predictor importance scores that were mostly linear with the predictor rank. MRMR, however, produced importance scores that underwent exponential decay as predictor rank increased. I didn't have any non-finite predictor importance scores. There was no clear trend among the features that were selected. In three of the four cases, wrist circumference was in the top 15 features, but χ^2 on the augmented data didn't value it as highly as the other methods did. For the base data, using the χ^2 method, 93 features were needed to explain 95% of the total score. Using the MRMR

method, 210 features were needed for the same percentage of the total score. For the augmented data, using the χ^2 method, 99 features were needed to explain 95% of the total score. Using the MRMR method, 162 features were needed for the same percentage of the total score.

C.8. MLP Classifier Results

The cross-validation results for the neural networks trained from the base data and the PCA/feature selection derived from the base data are shown in Table 6.

Table 6: Base data derived (132 subjects) classifier performance for various feature arrangements.

	Accuracy	Sensitivity	Specificity
Base	0.810606	0.68	0.892857
PCA Uniform	0.754837	0.40	0.975000
PCA Variance	0.720513	0.29	0.985714
F.S. χ^2	0.654138	0.11	0.987500
F.S. MRMR	0.802273	0.55	0.958929

The cross-validation results for the neural networks trained from the augmented data and the PCA/feature selection derived from the augmented data are shown in Table 7.

Table 7: Augmented data derived (132 subjects) classifier performance for various feature arrangements.

	Accuracy	Sensitivity	Specificity
Augmented	0.872696	0.73022	0.960079
PCA Uni.	0.75642	0.364835	0.995455
PCA Var.	0.758985	0.387363	0.986364
F.S. χ^2	0.689344	0.181319	1
F.S. MRMR	0.794792	0.473077	0.991107

Performing each round of cross-validation on the base data took about 5 minutes, while it took about 15 minutes for the augmented data.

C.9. Limitations

Because I decided to do 10-fold cross-validation instead of 7-fold and ended up doing sort-of-11-fold cross-validation, the results for the neural network classifier are not directly comparable to those presented in [104]. The origin of this awkward sort-of-10-fold cross-validation is my misreading of the MATLAB documentation and a lack of time in which to fix it. Additionally, this is not an exhaustive comparison between the number of features and the explained variance. The PCA-based data might yield significantly better results given enough components to explain 99% or 99.9% of the variance.

Unlike [104], subjects have not been recombined into their original individuals. This is a limitation from the medical perspective, but not from the machine learning perspective.

C.10. Dimension Reduction

PCA proved extremely effective at reducing dimensionality of the data, going from 403 features per subject to 5 or 6 features per subject. Unfortunately, the unsupervised PCA that I had chosen did not prove comparatively effective at identifying components relevant to the actual classification of the data, and the results from the neural network classifier trained with this data reflects this. Additionally, performing PCA on the augmented data lost all benefit the augmentation had on the accuracy of the classifier.

By contrast, feature selection was not particularly effective at reducing dimensionality. The χ^2 method proved ineffective overall, likely due to the large number of features in these datasets. The MRMR method, however, proved highly effective, retaining most of the accuracy of the base dataset (within 1-2%) while halving or quartering the number of features. Again, performing feature selection on the augmented data only hurt the results.

Possible future work would include the investigation of the effects of applying data augmentation *after* the PCA or feature selection has occurred to get the best of both worlds.

C.11. MLP Classifier

Despite the classifier used in this experiment not being directly comparable to the one used in [104], the results here still show that a network of that topology with the given data will benefit greatly from data augmentation, increasing accuracy by 6%.

Appendix D. Design of Antenna Array Switchboard for Microwave Imaging

The miniaturized 2.4 GHz dual antiphase patch antennas described in Chapter 4 on page 57 were designed as part of a novel 3D conformal array-based microwave imaging system, specifically designed for imaging of the brain. To use this antenna array, either a switchboard or a phased array controller was needed. Due to the complexity of a phased array controller and the relative simplicity of a switchboard, the switchboard was selected as the most expedient option to control the array. When comparing discrete RF switches, splitters, and combiners to the same functional units in PCB mountable form, the PCB mountable components proved cost effective. Further, building a custom PCB allowed minimization of size of the controller and minimization of length of the connections between devices that make up the controller. For these reasons, we elected to design and build a fully custom 8-antenna array switchboard PCB instead of building it out of discrete RF blocks and coaxial cables.

Table 8: Price comparison of the two individual parts with the greatest price difference between their PCB and Discrete versions. Mini-Circuits, (Brooklyn, NY, USA) parts with roughly equivalent specifications are shown [117].

Part Type	Discrete Cost (Part #)	Board Mount Cost (Part #)
DC – 3 GHz Absorptive SPDT Switch	\$68.94 (ZX80-DR230-S+)	\$3.39 (HSPA2-30DR+)
700 MHz – 2.7 GHz 8-way splitter/combiner	\$402.44 (ZN8PD-272SMP+)	\$114.94 (SEPS-8-272+)

Additional overhead costs are expected for both methods, though in general board manufacturing is expected to cost much more than parts for the discrete unit's assembly. Altogether, both methods are expected to yield similar final price tags. Due to this expectation, the advantages of the PCB method in size and customizability led us to choose that method to build the controller.

D.1. Constraints

To make the controller useful for controlling two arrays (transmitting and receiving) simultaneously, it was determined to need a minimum of eight controllable antennas. The controller needed to be able to work on its own, or when connected to a personal computer. It needed batteries on board to limit the number of cables, easing setup and allowing the array controller to be physically mounted on the subject's head with the array, but it would also be convenient if it may be powered by an offboard source for testing and debugging. Each of the

antennas needed to be able to connect to transmit, receive, or neither, in case an imaging pattern did not use all connected antennas simultaneously.

D.2. System Design

The switches were chosen as HSWA2-30DR+ from Mini-Circuits and the power splitter and combiner were chosen as SEPS-8-272+ again from Mini-Circuits.

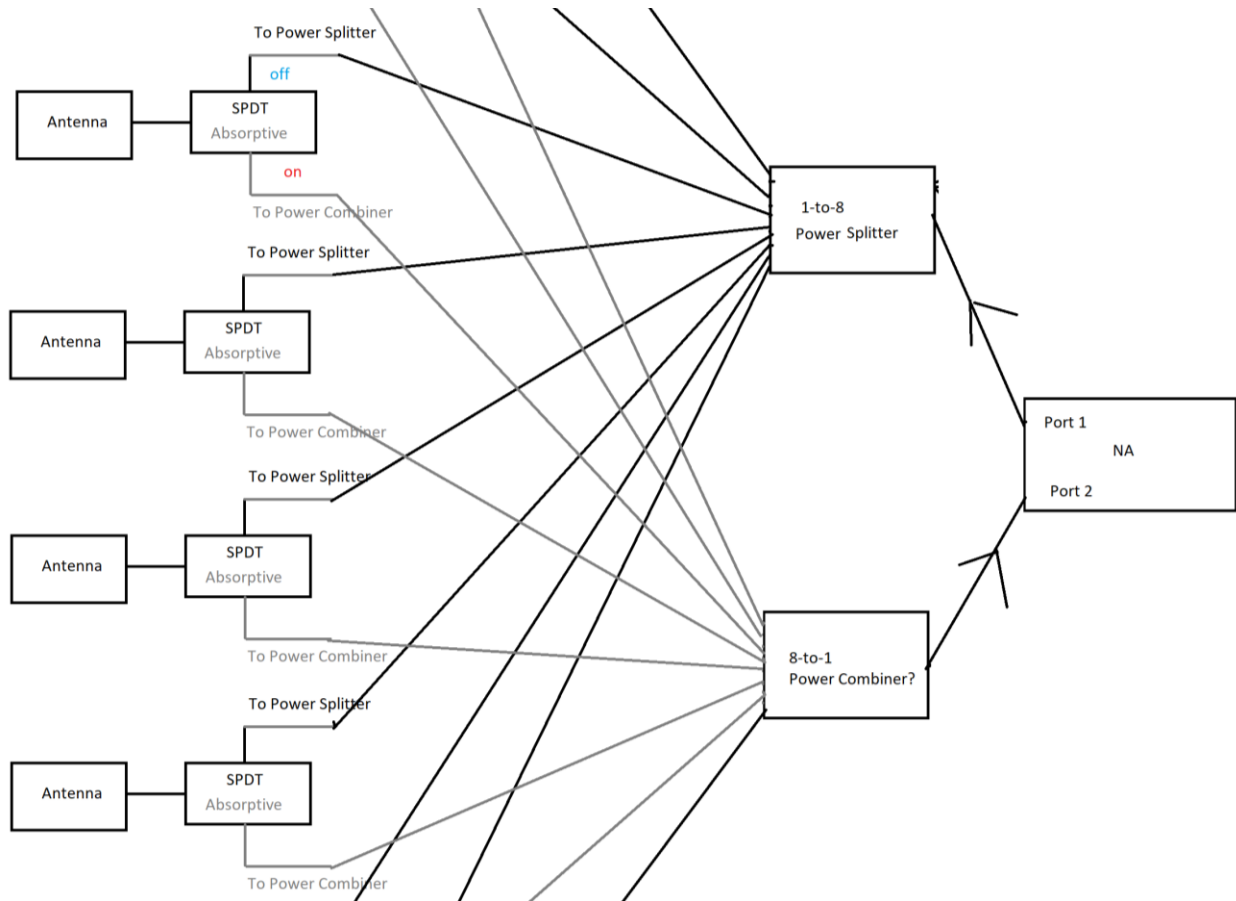


Fig. 42. Abbreviated block diagram of the core of the antenna switchboard. Each antenna is connected to its own switch, which can connect that antenna to either the splitter, the combiner, or simply ground the antenna through a 50 Ω load. The splitter and combiner connect off-board to a network analyzer. Only four of the eight antennas are shown in the diagram.

The board would have an onboard linear regulator, MCP1703T-3002 (Microchip Technology, Chandler, AZ, USA) to ensure the most consistent 3.0V supply possible to the switches. Autonomous control and interface with a PC would happen via an Arduino Nano Every (Arduino S.r.l., Partita, IVA). The Arduino Nano Every has a sufficient clock speed to handle the switching requirements and boasts castellated pins, allowing it to be soldered directly to the controller board to minimize its profile. The controller would have an onboard battery, an

offboard power connector, and the ability to run from the 5 V USB supply from the Arduino. Switching between these operating modes would be configured with pin jumpers.

D.3. Board Design

The circuits and boards were designed using Altium Designer to meet Advanced Circuits' (Aurora, CO, USA) standard board specification for 4-layer boards. This included the substrate material (FR-4), the copper thickness (1 oz/ in²), via depth (through all layers), and the pad finish (solder), as well as some cosmetic constraints [118]. The board shape was decided to be octagonal to minimize the profile of the board and better conform to the shape of the top of the head, where it was expected to be mounted. The octagon shape also allowed each antenna to be connected via an edge launch connector from its own edge of the PCB. The network analyzer would connect via vertical connectors from the center of the board. The two inner layers of the board would be ground planes while the two outer layers would be signal layers. All microstrip lines and vias on RF traces would be matched to 50 Ohms using a combination of Altium's built in impedance calculator and Saturn PCB Toolkit (Saturn PCB Design, Inc, DeBary, FL, USA). The top layer of the board mounted all of the RF switches, the splitter and combiner, and the vertical SMA connectors. The bottom layer mounted the Arduino, battery, and regulator circuitry. All RF traces were length-matched, which is to say the traces connecting the splitter to the switches were one length and the traces connecting the combiner to the switches were another length. Where possible, all RF traces also had the same number of vias inline, up to a maximum of two. A minimum of 30 mil spacing was maintained between RF traces and any adjacent metal on the same layer, to ensure the dominant coupling would be to the ground plane (spaced about 10 mil away on an interior layer). Copper pours were used around the switches and connectors to improve isolation between pins, as recommended by the datasheet [119]. Tapers were added to all RF pads using Altium designer's automatic taper generator. Low-speed traces, such as the switch control traces and the power traces were separated from RF traces by a minimum of 30 mil but were allowed to be within 10 mil of each other. Power traces were sized to allow 2 A of current with a temperature increase of 10 °C, while non-RF signal traces were sized to the same width as the RF traces. Fig. 43 shows the full layout of the switchboard, except for the ground planes on the two interior layers.

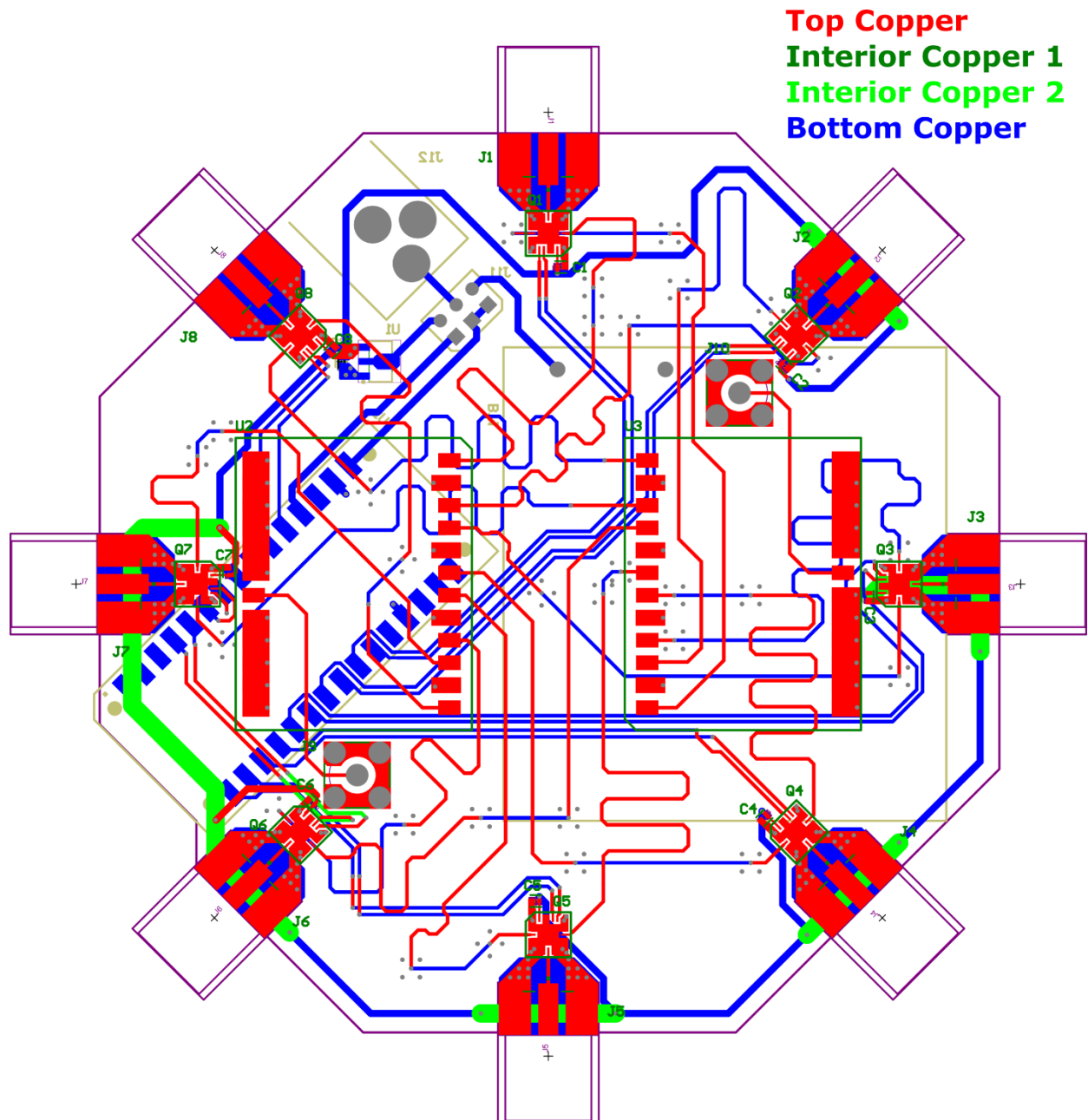


Fig. 43. Array switchboard board layout diagram. Top (red), bottom (blue) and traces on interior copper layer 2 (neon green) are shown. Interior copper layer 1 (dark green) is a ground plane and is not shown. Interior layer 2 is a ground plane except where traces are shown, this ground plane is not included in the figure. Top and bottom silkscreen markings are shown in dark green and dark yellow, respectively. Vias and through-hole pads are shown in grey.